Dissertation

Improving Flood Monitoring Capabilities using Synthetic Aperture Radar Data Cubes

Ausgeführt zum Zwecke der Erlangung des akademischen Grades eines Doktors der technischen Wissenschaften (Dr.techn.)

Unter der Leitung von
Univ.Prof. Dipl.-Ing. Dr.techn. Wolfgang Wagner

E120.1
Department für Geodäsie und Geoinformation
Forschungsgruppe Fernerkundung

Eingereicht an der Technischen Universität Wien
Fakultät für Mathematik und Geoinformation

von

Mark Edwin Tupas
[redacted]

Wien, im November 25, 2024

Dissertation

Improving Flood Monitoring Capabilities using Synthetic Aperture Radar Data Cubes

A thesis submitted in fulfillment of the academic degree of

Doktors der technischen Wissenschaften (Dr.techn.)

Under the supervision of
Univ.Prof. Dipl.-Ing. Dr.techn. Wolfgang Wagner

E120.1
Department of Geodesy and Geoinformation
Research Group Remote Sensing

Research conducted at TU Wien
Faculty of Mathematics and Geoinformation

by

Mark Edwin Tupas
[redacted]

Wien, im November 25, 2024 _____

Supervisor: Univ.Prof. Dipl.-Ing. Dr.techn. **Wolfgang Wagner**
Technische Universität Wien
Department of Geodesy and Geoinformation
Research Group Remote Sensing
Wiedner Hauptstraße 8/E120.1, A-1040 Vienna, Austria
E-Mail: wolfgang.wagner@geo.tuwien.ac.at

Referee: Prof. Dipl.-Ing. Dr.techn. **Gottfried Mandlburger**
Technische Universität Wien
Department of Geodesy and Geoinformation
Research Group Photogrammetry
Wiedner Hauptstraße 8/E120.1, A-1040 Vienna, Austria
E-Mail:Gottfried.Mandlburger@geo.tuwien.ac.at

Referee: Dr. **Masahiko Nagai** D. Eng
Yamaguchi University
Center for Research and Application of Satellite Remote Sensing
2-16-1 Tokiwadai,Ube,Yamaguchi 755-8611 Japan
E-Mail: nagaim@yamaguchi-u.ac.jp

Mark Edwin Tupas
Improving Flood Monitoring Capabilities
using Synthetic Aperture Radar Data Cubes
Dissertation, November 25, 2024

Technische Universität Wien
Department of Geodesy and Geoinformation
Research Group Remote Sensing
Wiedner Hauptstraße 8/E120.1, A-1040 Vienna, Austria

Author's Statement

Hiermit erkläre ich, dass ich diese Arbeit selbstständig verfasst habe, dass ich die verwendeten Quellen und Hilfsmittel vollständig angegeben habe und dass ich die Stellen der Arbeit - einschliesslich Tabellen, Karten und Abbildungen -, die anderen Werken oder dem Internet im Wortlaut oder dem Sinn nach entnommen sind, auf jeden Fall unter Angabe der Quelle als Entlehnung kenntlich gemacht habe.

I hereby declare that I independently drafted this manuscript, that all sources and references are correctly cited, and that the respective parts of this manuscript – including tables, maps, and figures – which were included from other manuscripts or the internet either semantically or syntactically are made clearly evident in the text and all respective sources are correctly cited.

Wien, im November 25, 2024

Mark Edwin Tupas

Acknowledgments

First, I am deeply thankful to my daughters, Kaia and Tala, for bearing with me throughout my doctoral studies. They have been my sources of strength and my compasses throughout this journey.

I want to express my profound gratitude to my supervisor, Wolfgang, for his patience and exceptional scientific sixth sense that helped me straighten this meandering scientific work. Thanks to the entire Remote Sensing Group for enriching my scientific journey and TU Wien GEO, where Jour Fixes were a scientific delight. A special thanks go to the SAR team, Florian and Bernhard B-M., who have always been there for me when I needed scientific second opinions. Many thanks to Felix O. for his top-notch administrative support. Thanks to my other colleagues at TU Wien and EODC for assisting with the technical tasks necessary for maintaining the SAR datacube featured in this work.

I also thank the following institutions that have provided me with the resources, monetary or otherwise, that have sustained me to accomplish this work. First, the Engineering Research and Development for Technology Program of the Philippine Department of Science and Technology, as well as the University of the Philippines System's Faculty, REPS, and Administrative Staff Development Program (FRASDP) without both, I would not have made it and continued my stay at TU Wien. I am also grateful for the European Commission's Joint Research Centre (EC-JRC) project titled "Provision of an Automated, Global, Satellite-based Flood Monitoring Product for the Copernicus Emergency Management Service" (GFM) and the colleagues I have worked with there for providing me with new challenges and giving context to my work. I also acknowledge the Vienna Scientific Cluster (VSC), where the computational results presented in this work were achieved. Additionally, I appreciate the financial support from TU Wien Bibliothek through its Open Access Funding program, which facilitated my publications. Acknowledgments to Grammarly for helping with my writing process.

I would also like to give thanks to Edy, April, the Castillo clan, Mike, Fr. Ron, and the rest of the gang for welcoming my family and I as part of their own in a now not-so-familiar land. I deeply appreciate my family's emotional support, even from a distance. My heartfelt appreciation goes to my parents, Edwin and Melit, for believing in me every step of the way.

Lastly, I want to express my wholehearted gratitude to my wife, Shom, who has worked the hardest and made the greatest sacrifices to help me accomplish this goal. Words cannot adequately convey my appreciation.

Abstract

Flooding poses a significant challenge across much of the world. It ranks as a leading natural disaster in terms of damage and the number of people affected. Effective management of floods requires rapid or Near Real-Time (NRT) mapping, primarily using satellite-based earth observation data. Synthetic Aperture Radar (SAR) data is considered the most suitable for flood mapping operations due to its ability to operate in all weather conditions, both day and night, and its skill at distinguishing between open water and land.

The Sentinel-1 SAR system has unrivaled temporal and spatial coverage and thus has been tapped for various flood mapping operations. To better harness the vast Sentinel-1 data holdings, most researchers use data cube solutions. Notable in this regard is the TU Wien flood mapping algorithm. This algorithm is based on Bayes Inference that leverages a Sentinel-1 data cube to define the no-flood probability distribution of pixels via harmonic modeling and flood probability from historical water samples reckoned per incidence angle. It contributes to the Copernicus Emergency Management System's (CEMS) Global Flood Mapping (GFM) ensemble workflow being operated in NRT.

While working well in most cases, it has issues such as underestimation in flood transition areas and overestimation in agricultural areas. Further, limitations due to SAR-based flood retrievals necessitate the application of exclusion masks. However, over reliance on exclusion masks also presents an issue. As the TU Wien algorithm's novel Bayesian Inference formulation presents opportunities for improvement, this thesis aims further to improve it in the context of global NRT operations. To do this, we systematically analyzed the algorithm performance and Bayesian Inference components for improvement.

First, we compared the performance of change detection algorithms in the northern Philippines as a study area. We tested four well-known change detection algorithms that rely on time-series SAR inputs against reference data from Sentinel Asia and optical imagery. We tested parameterizations such as no-flood estimates or references and threshold determination methods. The TU Wien algorithm was also varied by checking the effect of its low sensitivity masking. Our results suggest that the Bayesian Inference used for the TU Wien algorithm is superior to the other tested algorithms due to its stable performance regardless of parameterization.

We then proposed an alternative to non-informative priors using Height Above Nearest Drainage to derive spatially varying priors. The HAND data is used as an input to a two-parameter sigmoid function to generate the priors. We optimized and tested this new formulation of priors on five test events, comparing the HAND-based prior versus the original non-informed priors using CEMS rapid mapping results. Overall, the proposed HAND prior improved the flood mapping results by reducing false negatives, with the added benefit of removing dependence on an external HAND exclusion mask.

Further, we explored the use of the exponential filter to estimate a no-flood reference probability and replace the harmonic model. This filter is a promising alternative because

it accounts for the most recent backscatter observations, coupled with its recursive formulation, which makes it viable for NRT computation. We compared this filter and its parameterizations for flood mapping performance on four flood events in Europe covered by CEMS rapid activation and three sites in Asia covered by Sentinel Asia flood mapping activations. We then proposed a novel time series assessment of false positive rates to avert the pitfall of overfitting for flooded scenarios.

From the time-series assessments, we were able to analyze the causes of overestimation at no-flood scenarios by referencing ERA-5 data. We found that well-known causes of low backscatter, such as frost, dry soil conditions, and lesser-studied agriculture effects, trigger higher FPR at scale. In all cases, the exponential filter showed reduced FP. However, improvement to the exponential filter method is needed as prolonged floods in an area result in poorly estimated no-food references and, thus, poor flood mapping performance. We concluded that the exponential filter is an excellent alternative to the harmonic model.

In conclusion, we have established the TU Wien algorithm using the Sentinel-1 data cube as a robust method compared with other change detection algorithms. Further, we have shown improvements in the TU Wien algorithm from incremental changes to its Bayesian Inference framework. These improvements are being (and will be applied) to the TU Wien workflow under the CEMS GFM, thus impacting a true fully automated near-real-time global flood mapping operations.

Relevant Publications

The journal articles, contributions to conference proceedings and presentations relevant to this thesis that I developed during my doctoral studies are presented here.

The following **articles** have been published in **peer review journals included** in this thesis:

- Tupas, M. E., Roth, F., Bauer-Marschallinger, B., & Wagner, W. (2023). An Intercomparison of Sentinel-1 Based Change Detection Algorithms for Flood Mapping. Remote Sensing, 15(5), Article 5. https://doi.org/10.3390/rs15051200
- Tupas, M. E., Roth, F., Bauer-Marschallinger, B., & Wagner, W. (2023). Improving Sentinel-1 Flood Maps Using a Topographic Index as Prior in Bayesian Inference. Water, 15(23), Article 23. https://doi.org/10.3390/w15234034
- Tupas, M. E., Roth, F., Bauer-Marschallinger, B., & Wagner, W. (2024). Assessment of Time-Series-Derived No-Flood References for SAR-based Bayesian Flood Mapping. GIScience & Remote Sensing, 61(1), 2427304. https://doi.org/10.1080/15481603.2024.2427304

The following are my **contributions to conferences with full proceedings not included** in this thesis:

- Tupas, M. E., Navacchi, C., Roth, F., Bauer-Marschallinger, B., Reuß, F., & Wagner, W. (2022). Computing Global Harmonic Parameters for Flood Mapping using TU WIEN's SAR Datacube Software Stack. The International Archives of the Photogrammetry, Remote Sensing and Spatial Information Sciences, XLVIII-4-W1-2022, 495–502. https://doi.org/10.5194/isprs-archives-XLVIII-4-W1-2022-495-2022
- Tupas, M. E., Roth, F., Bauer-Marschallinger, B., & Wagner, W. (2024). Assessing Global Hand Datasets as Priors for SAR-Based Bayesian Flood Mapping. IGARSS 2024 - 2024 IEEE International Geoscience and Remote Sensing Symposium, 1209–1213. https://doi.org/10.1109/IGARSS53475.2024.10641043

The following are my **conference presentations without full paper proceedings not included** in this thesis:

- Tupas, M. E., Roth, F., Bauer-Marschallinger, B., Reuß, F., Raml, B., & Wagner, W. (2024, June 12). Enabling Global Flood Monitoring with SAR Datacubes and theVienna Scientific Cluster [Paper presentation]. ASHPC24 – Austrian-Slovenian HPC Meeting 2024, Grundlsee, Austria. https://doi.org/10.25365/phaidra.463

I have also **contributed** to the following **peer-reviewed journal articles but not included** in this thesis:

- Bauer-Marschallinger, B., Cao, S., Tupas, M. E., Roth, F., Navacchi, C., Melzer, T., Freeman, V., & Wagner, W. (2022). Satellite-Based Flood Mapping through Bayesian Inference from a Sentinel-1 SAR Datacube. Remote Sensing, 14(15), Article 15. https://doi.org/10.3390/rs14153673
- Roth, F., Bauer-Marschallinger, B., Tupas, M. E., Reimer, C., Salamon, P., & Wagner, W. (2023). Sentinel-1-based analysis of the severe flood over Pakistan 2022. Natural Hazards and Earth System Sciences, 23(10), 3305–3317. https://doi.org/10.5194/nhess-23-3305-2023

I have also contributed in the preparation and publication of the following **datasets**:

- Roth, F., Tupas, M. E., Reuß, F., Navacchi, C., Bauer-Marschallinger, B., & Wagner, W. (2023). Sentinel-1 Global Harmonic Parameters: A Seasonal Model for Flood Mapping and More [Data set]. TU Wien Research Data. https://doi.org/10.48436/x8p2j-1tj74

Acronyms

The following abbreviations are used in this manuscript:

BI	Bayes(ian) Inference
CEMS	Copernics Emergency Management Service
CSI	Critical Success Index
DEM	Digital Elevation Model
DOY	Day Of Year
EODC	Earth Observation Data Centre for Water Resources Monitoring
EXPF	Exponential Filter
FN	False Negative
FP	False Positive
FPR	False Positive Rates
GFM	Global Flood Monitoring
GRDH	Ground Range Detected High-resolution SAR product
HAND	Height Above Nearest Drainage
HPAR	Harmonic Parameters
IW	Interferometric Wide Swath mode of Sentinel-1
MNDWI	Modified Normalized Difference Water Index
NDWI	Normalised Difference Water Index
NDSI	Normalised Difference Scattering Index
NRT	Near-Real-Time
NSM	No-sensitivity Mask
OA	Overall Accuracy
PA	Producer Accuracy
PDF	Probability Distribution Function
PLIA	Projected Local Incidence Angle θ
RMSD	Root Mean Square Deviation
UA	User Accuracy
NRT	Near-Real-Time
SA	Sentinel Asia
SAR	Synthetic Aperture Radar
SSE	Sum of Squared Errors
SIG0	Sigma Nought backscatter coefficient σ_0
SNDSI	Shanon's entropy of Normalised Difference Scattering Index
SR	Standardized Residuals
STD	Standard Deviation
TN	True Negative
TP	True Positive
WM	Water Mask

Contents

1 Introduction **21**
- 1.1 Motivation . . . 21
  - 1.1.1 Need for SAR-based Flood Mapping at Near Real Time . . . 21
  - 1.1.2 Flood Mapping Theory and the TU Wien Flood Mapping Algorithm 21
- 1.2 Research Objective and Questions . . . 22
- 1.3 Structure of the Thesis . . . 23
  - 1.3.1 Publication Summaries . . . 24
  - 1.3.2 Author Contributions . . . 25

2 An Intercomparison of Sentinel-1 Based Change Detection Algorithms for Flood Mapping **26**
- 2.1 Abstract . . . 27
- 2.2 Introduction . . . 27
- 2.3 Change Detection Algorithms . . . 29
  - 2.3.1 Normalized Difference Scattering Index . . . 29
  - 2.3.2 Shannon's entropy of NDSI . . . 29
  - 2.3.3 Standardized Residuals . . . 30
  - 2.3.4 Bayesian Inference . . . 30
  - 2.3.5 Thresholding Techniques . . . 31
  - 2.3.6 Selection of No-Flood Reference . . . 31
- 2.4 Data and Study Site . . . 31
  - 2.4.1 Sentinel-1 Data Cube . . . 31
  - 2.4.2 Study Area . . . 31
  - 2.4.3 Reference Flood Maps . . . 32
  - 2.4.4 Auxiliary Data . . . 33
- 2.5 Methods . . . 34
  - 2.5.1 Paramterizations . . . 35
  - 2.5.2 Accuracy Assessment . . . 37
- 2.6 Model Parameter Assessment . . . 37
  - 2.6.1 Parameterization of NDSI Model . . . 39
  - 2.6.2 SNDSI Parameterization . . . 40
  - 2.6.3 Standardized Residuals Parameterization . . . 41
  - 2.6.4 Bayes Inference Parameterization . . . 41
  - 2.6.5 Parameterization Summary . . . 42
- 2.7 Model Intercomparison . . . 43
- 2.8 Conclusions . . . 46
- 2.9 Acknowledgments . . . 47
  - 2.9.1 Funding . . . 47
  - 2.9.2 Data Avialability . . . 48

3 Improving Sentinel-1 Flood Maps Using a Topographic Index as Prior in Bayesian Inference 49
3.1 Abstract . . . 50
3.2 Introduction . . . 50
3.3 Height Above the Nearest Drainage As A Prior . . . 51
3.3.1 SAR flood mapping using Bayes Inference . . . 51
3.3.2 HAND Based Prior Probability Function . . . 52
3.4 Materials and Methods . . . 53
3.4.1 Study Sites . . . 53
3.4.2 Materials . . . 54
3.4.3 HAND Prior Probability Function Parameter Estimation . . . 55
3.4.4 Comparative Performance . . . 56
3.5 Results and Discussions . . . 57
3.5.1 Prior Probability Parameterization . . . 57
3.5.2 Comparative Results HAND prior . . . 58
3.5.3 No-flood Conditions . . . 63
3.6 Summary and Conclusions . . . 64
3.7 Acknowledgements . . . 66
3.7.1 Funding . . . 66
3.7.2 Data Availability . . . 66

4 Assessment of Time-Series-Derived No-Flood References for SAR-based Bayesian Flood Mapping 67
4.1 Abstract . . . 68
4.2 Introduction . . . 68
4.3 TU Wien Flood Mapping Algorithm . . . 70
4.3.1 Harmonic Model . . . 70
4.3.2 Exponential Filter Model . . . 71
4.3.3 Standard Deviation . . . 72
4.3.4 No-Sensitivity Masking and Post-processing . . . 72
4.4 Materials and Study Sites . . . 72
4.4.1 Sentinel-1 Data cube . . . 73
4.4.2 Ancillary Data . . . 73
4.4.3 Reference Flood and Water Maps . . . 74
4.4.4 Study sites . . . 74
4.5 Assessment Methodology . . . 76
4.5.1 Reference Image and No-Flood Time-Series Assessment . . . 76
4.5.2 Flood Map Assessment . . . 76
4.6 Results . . . 77
4.6.1 No-flood Time Series . . . 77
4.6.2 False Positive Frequency Mappings . . . 82
4.6.3 Flood Scenarios Quantitative Analysis . . . 82
4.6.4 Flood Scenarios Confusion Maps . . . 85
4.7 Discussion . . . 88
4.7.1 No-flood conditions . . . 88
4.7.2 Flood conditions . . . 88

4.7.3 T-value selection . . . 89
4.7.4 Long Floods and Exponential Filter Prospects . . . 89
4.8 Conclusions and Outlook . . . 90
4.9 Acknowledgements . . . 91
4.9.1 Funding . . . 91
4.9.2 Data Availability . . . 91
4.10 Supplementary material . . . 93
4.10.1 No-Flood Temporal Plots . . . 93
4.10.2 Pairwise Statistical Significance . . . 96
4.10.3 False Positive Frequency Maps . . . 96
4.10.4 Comparison of Mean and Exponential Filter . . . 99

5 Conclusions and Outlook **103**
5.1 Conclusions and Potential Impact . . . 103
5.2 Outlook . . . 104

Bibliography **107**

Chapter 1

Introduction

1.1 Motivation

1.1.1 Need for SAR-based Flood Mapping at Near Real Time

Flooding is a concern that affects most of the globe and its population [13, 96, 110]. It consistently ranks among the top natural disasters in terms of infrastructure damage and lives affected. Unfortunately, floods are expected to worsen because of climate change [45].

To manage flooding events, rapid or Near Real-Time (NRT) mapping is of the utmost importance. While traditional field-based mapping and drone surveys provide accurate information, their usability is limited due to scale and costs. Hence, for large-scale floods, most rely on space-borne earth observation data.

In this regard, Synthetic Aperture Radar (SAR) data is proving to be the best option for operational flood mapping [98, 102, 109]. This is because of SAR's day-night and all-weather capability. Along with its sensitivity to distinguishing open water from other land cover types. Thus, attempts at developing operational SAR-based flood mapping workflows have garnered significant attention in literature[12, 73, 120].

SAR-based flood mapping techniques include single-image thresholding algorithms [39, 71], parametric or tile-based thresholding schemes [15, 72, 120, 141], change detection algorithms [18, 24, 80] and machine learning methods [53, 105, 132]. However, not all SAR-based algorithms are viable as NRT workflows. For NRT operations, an algorithm should not require subjective manual inputs– automated, objective, and repeatable [35, 71]. These points emphasize the need to investigate SAR-based flood mapping methods further for global NRT implementation.

1.1.2 Flood Mapping Theory and the TU Wien Flood Mapping Algorithm

In most flood detection algorithms' core is the identification of water. SAR data is a strong choice for flood mapping because of its ability to differentiate calm standing water due to its low backscatter from specular reflection of microwave signals. However, without context, floods on Earth observation images are no different from existing water bodies. Thus, the temporal dimension is often used to differentiate floods from non-crisis inundations such as permanent or seasonal water bodies.

In terms of temporal and spatial coverage, the Sentinel-1 SAR system is unrivaled and thus has been tapped for various flood mapping operations. Sentinel-1 uses a C-band

sensor (CSAR) onboard a designed constellation of two satellites, with its main operation measuring backscatter in VV and VH polarizations over land [113]. Sentinel-1 offers systematic repeat observations within 12 days for a single satellite and an image every six days when tandem satellites are available.

To harness the huge Sentinel-1 data holdings better, most researchers turn to data cube solutions. These solutions offer access and processing mechanisms for large temporal earth observation data collections abstracted as multi-dimensional arrays. SAR datacubes solutions have proliferated [37, 77, 111, 125], and to varying degrees relied upon for flood mapping [24, 121].

A notable implementation is the TU Wien flood mapping algorithm based on Bayes Inference [8]. This algorithm leverages a Sentinel-1 datacube to define the no-flood probability distribution of pixels via harmonic modeling and flooded probability from historical water samples reckoned per incidence angle. This algorithm contributes to the Copernicus Emergency Management System's (CEMS) Global Flood Mapping (GFM) [98] ensemble workflow being operated in NRT.

While working well in most cases– showing good use cases for temporal analysis [97], it has shown issues such as underestimation in flood transition areas and overestimation in agricultural areas [8]. Understandably, a globally applied method would not work well everywhere. Further, limitations due to SAR-based flood retrievals (e.g., urban and arid areas) necessitate the application of exclusion masks [137]. From our experience with GFM, overreliance on exclusion masks also presents an issue. It is an advantage that the TU Wien algorithm's novel Bayesian Inference formulation presents several opportunities for improvement.

1.2 Research Objective and Questions

The main objective of the study is to further improve the TU Wien flood mapping algorithm in the context of global NRT operations. Hence, instead of looking at more complex solutions that might incur greater processing requirements– we aim to systematically analyze the algorithm performance and its Bayesian inference components. Thus, to guide this doctoral research, we have posed the main research question:

How can the SAR-datacube-based TU Wien algorithm be further improved to better address the challenges of global near-real-time application?

We further break down the problem into three main parts to answer this. First, we aim to establish the viability of the TU Wien flood mapping algorithm compared to other algorithms that follow similar concepts, specifically those that utilize time-series information and apply change detection concepts. Hence, we pose the following questions:

How does the TU Wien flood mapping algorithm perform compared to other change detection SAR-based flood mapping algorithms?

Specifically:

- *Are time-series-based change detection algorithms suitable for operational flood mapping? Which algorithms perform well in this context?*
- *Do parameterizations have a significant effect on each algorithm's performance? Do these algorithms require localization or tuning to work well?*

After establishing the TU Wien algorithm's robust performance compared to its peers, we set out to improve our method incrementally. We first look at the aspect of Bayesian algorithms that has received fewer contributions in literature. Specifically the priors. In this regard, we ask the following:

Does topography-based a priori information improve SAR-based flood mapping?

Specifically:

- *How to utilize topographic information as priors for SAR-based flood mapping without localized tuning?*

Another aspect that could be improved in the Bayes Formulation is the no-flood reference case. Hence, we looked at this issue and tried to answer these posed questions:

Is the exponential filter a viable option as a no-flood reference to improve SAR-based flood mapping?

Specifically:

- *Does the exponential filter perform better than the harmonic model for flood mapping in scenes with floods and no floods?*
- *How prevalent is the overestimation of floods using the TU Wien algorithm in no-flood scenarios? What are its causes? Could using an exponential filter address this issue?*
- *How can we assess the performance of flood mapping algorithm improvements considering the need for automated execution for near-real-time operations?*

1.3 Structure of the Thesis

To systematically answer these thesis questions and objectives, we subdivide this work into five Chapters, including the first Introductory chapter, the last concluding chapter, and the three main middle chapters based on published peer-reviewed journal articles. Chapter 1 introduces the motivations, objectives, and outline of this study. Chapter 2 describes our initial study, where we examined the performance of the TU Wien flood mapping algorithm compared with other data cube or time-series-based methods. Chapter 3 discusses our attempt to improve the TU Wien algorithm using priors derived from topographic information. Chapter 4 assesses the viability of using an exponential filter instead of the harmonic model for no-flood reference probability to further improve the TU Wien Algorithm for global application. Lastly, Chapter 5 includes the conclusions, implications, and recommendations of this study.

1.3.1 Publication Summaries

In this section, we briefly summarize the work done in the middle Chapters– the aforementioned published journal articles.

In Chapter 2: **An Intercomparison of Sentinel-1 Based Change Detection Algorithms for Flood Mapping** [117], We compared the performance of change detection algorithms. We selected the northern Philippines as a study area to test four well-known change detection algorithms that rely on time-series SAR inputs against reference data from Sentinel Asia and optical imagery.

We took a look at the theoretical basis for these algorithms and possible parametrizations. As change detection methods, they commonly require no-flood estimates or references. Thus, we tested prior images, temporal mean, and the harmonic model as inputs. We also tested threshold determination methods such as the fixed values from literature, Otsu, and KI methods. In contrast, the TU Wien algorithm was also varied by checking the effect of its low sensitivity (a.k.a. internal pdf) masking method. Our results suggest that the Bayesian Inference used for the TU Wien algorithm is superior to the other tested algorithms due to its stable performance regardless of parameterization.

In Chapter 3: **Improving Sentinel-1 Flood Maps Using a Topographic Index as Prior in Bayesian Inference** [119], I proposed an alternative to the usual non-informative priors using Height Above Nearest Drainage to derive spatially varying priors. The HAND data is used as an input to a two-parameter sigmoid function to generate the priors. We optimized and tested this new formulation of priors on five test events, where we compared the HAND-based prior versus the original non-informed priors using CEMS rapid mapping results. Overall, the proposed HAND prior improved the flood mapping results by reducing false negatives while also removing the dependence on an external HAND exclusion mask.

In Chapter 4: **Assessment of Time-Series-Derived No-Flood References for SAR-based Bayesian Flood Mapping** [116], we explored the possibility of using the exponential filter, inspired by soil moisture studies [126], to estimate a no-flood reference probability replacing the harmonic model. This filter is a promising alternative since it uses the most recent backscatter observations, thus more accurately coping with the dynamic changes. Unlike other temporal filters, the exponential filter has a recursive formulation, making it viable for NRT computation. In this work, we compared this filter and its' parameterizations effect on the flood mapping performance on four flood events in Europe covered by CEMS rapid activation and three sites in Asia covered by Sentinel Asia flood mapping activations. We proposed a novel time series assessment of false positive rates to avert the pitfall of overfitting for flooded scenarios.

In this time-series assessment, we also looked at the RMSD of the no-flood reference models to check their capacity to estimate the no-flood SAR scene. In time-series assessments of the RMSD and FPR, we analyzed the causes of overestimation at no-flood scenarios by referencing ERA-5 data. We found that well-known causes of low backscatter– such as frost, dry soil conditions, and the lesser studied agriculture effects –trigger higher FPs at scale. We showed the effect of changing its descriptive parameter and settling on an optimal estimate. In all cases, the exponential filter at this parameterization showed reduced FP. However, improvement to the exponential filter method is required to realize

its potential for global flood mapping. It was observed that prolonged floods result in poorly estimated no-flood references and, thus, poor flood mapping performance.

1.3.2 Author Contributions

The publications contained in this thesis would not have been possible without the contributions of my three co-authors: Wolfgang Wagner (W.W.), Bernhard Bauer-Marschallinger (B.B.-M), and Florian Roth (F.R.). As the primary author (M.E.T.) of these publications, my contributions are as follows:

- **An Intercomparison of Sentinel-1 Based Change Detection Algorithms for Flood Mapping:** Conceptualization M.E.T. and W.W.; methodology M.E.T. and W.W.; software M.E.T. and F.R.; validation M.E.T. and F.R.; formal analysis M.E.T.; investigation F.R., M.E.T. and B.B.-M.; data curation M.E.T.; writing—original draft preparation M.E.T.; writing—review and editing ALL; visualization M.E.T. and B.B.-M.; supervision B.B.-M. and W.W.
- **Improving Sentinel-1 Flood Maps Using a Topographic Index as Prior in Bayesian Inference:** Conceptualization, M.E.T., and W.W.; methodology, M.E.T., and W.W.; software, M.E.T., and F.R.; validation, M.E.T.; formal analysis, M.E.T.; investigation, M.E.T.; data curation, M.E.T.; writing—original draft preparation, M.E.T.; writing—review and editing, all authors; visualization, M.E.T.; supervision, B.B.-M. and W.W.
- **Assessment of Time-Series-Derived No-Flood References for SAR-based Bayesian Flood Mapping:** Conceptualization, M.E.T. and W.W.; methodology, M.E.T. and W.W.; software, M.E.T., and F.R.; validation, M.E.T.; formal analysis, M.E.T.; investigation, M.E.T.; data curation, M.E.T.; writing—original draft preparation, M.E.T.; writing—review and editing, all authors; visualization, M.E.T.; supervision, W.W.

Chapter 2

An Intercomparison of Sentinel-1 Based Change Detection Algorithms for Flood Mapping

This chapter is a reformatted accepted version of:
Tupas, M. E., Roth, F., Bauer-Marschallinger, B., & Wagner, W. (2023). An Intercomparison of Sentinel-1 Based Change Detection Algorithms for Flood Mapping. Remote Sensing, 15(5), Article 5. `https://doi.org/10.3390/rs15051200`
The original document is openly accessible at: `https://www.mdpi.com/2072-4292/15/5/1200` under the Creative Commons Attribution (CC-BY) license.

2.1 Abstract

With its unrivaled and global land monitoring capability, the Sentinel-1 mission has been established as a prime provider in SAR-based flood mapping. Compared to suitable single-image flood algorithms, change-detection methods offer better robustness, retrieving flood extent from a classification of observed changes. This requires data-based parametrization. Moreover, in the scope of global and automatic flood services, the employed algorithms should not rely on locally optimized parameters, which cannot be automatically estimated and have spatially varying quality, impacting much on the mapping accuracy. Within the recently launched Global Flood Monitoring (GFM) service, we implemented a Bayes-Inference (BI) based algorithm designed to meet these ends. However, whether other change detection algorithms perform similarly or better is unknown. This study examines four Sentinel-1 change detection models: Normalized Difference Scattering Index (NDSI), Shannon's entropy of NDSI (SNDSI), Standardized Residuals (SR), and Bayes Inference over Luzon in the Philippines, which was flood-hit by a typhoon in November 2020. After parametrization assessment against an expert-created Sentinel-1 flood map, the four models are inter-compared against an independent Sentinel-2 classification. The obtained findings indicate that the Bayes change detection profits from its scalable classification rules and shows the least sensitivity to parametrization choices while also performing best in terms of mapping accuracy. For all change detection models, a backscatter seasonality model for the no-flood reference delivered best results.

Keywords: Flood Mapping; Change Detection; SAR; Sentinel-1; Datacube; Philippines

2.2 Introduction

Flooding is a significant concern all over the world. In global disaster assessment reports, it consistently ranks among the most destructive of natural disasters. Unfortunately, flood frequency and severity are expected to increase for most of the world due to climate change [45], with further increased human exposure due to population growth. Therefore rapid assessments of flood extent and impacts using Earth observation satellites are of great importance. Due to their capacity to capture high-resolution images of the Earth's surface even in stormy weather, Synthetic Aperture Radar (SAR) sensors are unrivaled in their capability to map large-scale flooding. Hence most disaster mapping services, such as the Copernicus Emergency Management Service (CEMS) [128], and the Sentinel Asia initiative [51] utilize SAR satellites for their operations. In the past, these services have delivered SAR-based flood maps only upon requests from affected areas, manually operated by human experts. This implies that flood events may be missed in case of late or non-activation. To avoid this and improve timeliness, CEMS has recently launched a Global Flood Monitoring (GFM) service that analyses Sentinel-1 SAR data in a fully automatic fashion [98].

In principle, mapping flood extent from SAR images is relatively straightforward given that backscatter from open water bodies is normally relatively low compared to backscatter from the surrounding land surface areas. Thus, when mapping flooded areas from individual

SAR images on demand, SAR image analysts usually work with simple thresholding techniques. However, selecting a threshold value that works everywhere under all weather conditions is clearly impossible [35, 71]. Therefore, in the fully automatic GFM service, a relatively simple problem turns into the significant scientific challenge of finding a robust flood detection model that works globally without the need for manual fine-tuning of its parameters.

A large variety of methods to map flood extent from SAR imagery has already been published, including change detection-based approaches [18, 101], split-window or tiled thresholding techniques [12, 64, 71, 120], Bayesian [21, 34, 94, 100, 129] and machine learning methods [20, 75, 138]. Most studies yielded excellent results for specific test areas, but the performance on a large scale is often not known [139]. Moreover, while reviews and assessments of these SAR flood and inundation mapping methods are available, [73, 103, 104], it has been pointed out that direct performance comparisons are limited [56]. However, such comparisons are crucial in designing and improving operational systems that perform at large scales, e.g., regional or global extents. Last but not least, distinct parameterizations might be required for these methods to perform at the same level in different areas. Thus the robustness of parameterization is a crucial indicator when selecting flood mapping workflows for implementation at scale [8, 15, 72]. Unfortunately, this aspect usually is not treated explicitly in the scientific literature so far.

For the design of robust flood detection models and their parameterization, it is highly advantageous to work with SAR backscatter data cubes that allow efficient access to the data not just in the spatial but also temporal dimension [77, 111]. Using the Sentinel-1 backscatter data cube built up at the Earth Observation Data Centre (EODC) [125], it has, e.g., been possible to parameterize a Bayesian flood detection model at the level of individual pixels by analyzing backscatter time series for each pixel [8]. Another example is the Sentinel-1 data cube implementation at the Google Earth Engine [37], which already hosts several waterbody and flood mapping workflows [24, 69].

In this contribution, we compare the performance of four change detection models for mapping floods using Sentinel-1 SAR data (Section 2.3). Compared to approaches that map floods only based on single SAR images, the parameterization of change detection models is normally less problematic, allowing to apply them over large and diverse domains. Nonetheless, even the parameterization of change detection models may involve a lot of choices that can have a strong impact on the accuracy of the derived flood maps, in particular the choices of the no-flood reference image and the threshold for labeling a SAR pixel as flooded. Hence, in our study, we investigated how sensitive the different model are to changes in their parameterization.

As a study case, we chose a flood event that occurred in the Cagayan river basin in the Northern Philippines in November 2020. This choice was motivated by the fact that the area, which is situated in the Pacific typhoon belt, is projected to be significantly impacted by climate change, including a general rise in precipitation with an indication of higher frequency of heavy rainfall events [7] and, consequently, a greater threat of flooding [112]. The study region and data are described in Section 2.4. The methods for intercomparing the four change detection models and assessing the robustness of their parameterizations are introduced in Section 2.5, followed by the presentation of the results

on parametrization and model-intercomparison in Sections 2.6 and 2.7. Finally, Section 2.8 contains the discussion and conclusions.

2.3 Change Detection Algorithms

Change detection approaches for flood mapping compare in one way or another a SAR backscatter image potentially containing flood pixels with a reference SAR scene describing a non-flooded situation. By comparing two images, spatial signal variations are reduced, simplifying the task of finding suitable thresholds and model parameterizations that work for different land cover classes. Furthermore, the use of a no-flood reference image allows for excluding other low backscatter areas that tend to be mislabeled as a flood. Nonetheless, factors such as speckle and overall high variability of the backscatter measurements prompt the need for some additional means of normalization. This problem is solved differently in the four change detection models that we selected for this study, namely the Normalized Scattering Difference Index, the Shannon's entropy of NDSI, the Standardized Residuals, and a Bayesian Inference method. Given that the choice of the no-flood reference and different thresholding techniques has an important impact on the performance of these four models, these parameterizations are discussed separately in subsections 2.3.5 and 2.3.6.

2.3.1 Normalized Difference Scattering Index

Indices such as the Normalized Difference Scattering Index (NDSI) [123] and the Normalized Difference Ratio [4], while differently named, are similarly computed from backscatter data from a flood image and a no-flood reference. For our purposes, we adopt the NDSI for the rest of the document and compute it with:

$$\mathrm{NDSI} = \frac{\sigma^0 - \sigma^0_r}{\sigma^0 + \sigma^0_r} \tag{2.1}$$

where σ^0 represents the SAR image pixels that are potentially flooded and σ^0_r the no-flood reference. Both σ^0 and σ^0_r are expressed in $\mathrm{m^2 m^{-2}}$. In this formulation, flooded areas are associated with large negative numbers due to the decrease in backscatter when the land surface is inundated, i.e., a pixel is labeled as flooded when NDSI is smaller than a chosen threshold value. The normalization term $\sigma^0 + \sigma^0_r$ helps to reduce the impact of signal variations in the reference image.

2.3.2 Shannon's entropy of NDSI

Ulloa et al. [123] extends the NDSI concept further by computing the Shannon's entropy of NDSI using a 9 x 9 moving window. The premise of this approach is that flooded pixels are often adjacent to other flooded pixels (save for boundaries) and, thus, should primarily have a smooth texture. Furthermore, since entropy measures the level of uncertainty of possible grayscale values in a given area, it also serves as a textural measure. Shannon's entropy of NDSI, referred here to as SNDSI, is computed by:

$$\mathrm{SNDSI} = -\sum_{n} p * \log_2 p \tag{2.2}$$

where p is the probability of NDSI estimated from a normalized histogram count for all n pixels in the moving window. As for the NDSI, pixels are classified as flooded when SNDSI becomes smaller than a chosen threshold.

2.3.3 Standardized Residuals

An alternative approach to normalize the difference term $\sigma^0 - \sigma_r^0$ is to use a measure of variance of the backscatter measurements [18, 24, 80, 101]. Here we adopt the terminology of Schlaffer et al. [101] who computed Standardized Residuals (SR)

$$\mathrm{SR} = \frac{\sigma^0 - \sigma_r^0}{StDev(\sigma^0)} \tag{2.3}$$

where $StDev(\sigma^0)$ is the temporal standard deviation of σ^0 for non-flooded conditions. $StDev(\sigma^0)$ is computed from historic σ^0 time series for each pixel describing the variability of the backscatter measurements due to changes in soil moisture, vegetation, or other environmental factors for each location. Thereby, a pixel is considered to be flooded if SR has a large negative value which indicates that σ^0 is outside the expected signal range. Note that because of the need to compute $StDev(\sigma^0)$ from historic time series, the SR model is substantially more input-data-demanding than the NDSI and SNDSI models that can in principle be run with just two input images. Nonetheless, similar to NDSI and SNDSI, one needs to chose a threshold.

2.3.4 Bayesian Inference

Instead of normalizing differences, another way of comparing flood and no-flood situations is to use probabilistic approaches. The method adopted here is based on a pixel-based Bayesian Inference (BI) method [8, 100] that considers the temporal SAR backscatter information of a non-flooded pixel to estimate its non-flooded conditional probability distribution, $p(\sigma^0|N)$. The conditional flooded probability distribution, $p(\sigma^0|F)$, can be estimated from geographically distributed calm open water samples. The probability that a σ^0 measurement over one pixel indicates flood conditions is calculated with [34, 94, 100]:

$$\mathrm{BI} \equiv p(F|\sigma^0) = \frac{p(\sigma^0|F)p(F)}{p(\sigma^0|F)p(F) + p(\sigma^0|N)p(N)} \tag{2.4}$$

where $p(F)$ and $p(N)$ are the prior probabilities of a pixel being flooded and non-flooded (in short simply "priors"). Here we adopt non-informed priors, with both $p(F)$ and $p(N)$ assumed to have equal i.e. 0.5, prior probability. A pixel is labeled as a flood if the flood probability $p(F|\sigma^0)$ is greater than 0.5. For easy of discussion, we refer to the numerical value of $p(F|\sigma^0)$ as BI in the following sections. Note that in contrast to the other three models, the final decision criterion is well defined, i.e. BI > 0.5. Like SR, the BI model is input-data demanding, requiring a backscatter data cube to pre-compute $p(\sigma^0|N)$ per pixel.

2.3.5 Thresholding Techniques

Except for the BI method, the change detection models introduced above require the choice of a threshold to label a SAR pixel as flooded or non-flooded. The choices one can make range from choosing one fixed threshold value for all SAR images and the entire study domain to threshold values computed for each SAR image individually or even subsets of a SAR image. Similar to the work of Landyut et. al [56] we test fixed threshold values taken from the literature and thresholds dynamically selected using histogram-based methods. In particular, we investigate the performance of global Otsu's [84] and Kittler and Illingworth's (KI) methods [54] along with best performing fixed value from the source materials.

2.3.6 Selection of No-Flood Reference

In principle, the selection of the no-flood reference σ^0_r has a great effect on all models described above. When choosing a real SAR image as reference, one would like to choose a scene that resembles – except for the inundation areas – the unflooded conditions as good as possible in terms of land cover and environmental conditions. This may e.g. be the latest pre-flood image or a SAR image acquired in the same season the previous year. While automated methods for the selection of such real reference images have been proposed [47, 139], the computation of synthetic no-flood reference is a viable alternative approach when working with SAR backscatter data cube. Here we test the generation of synthetic σ^0_r images by computing the mean backscatter and the expected seasonal backscatter value for the day of year [101]. Median, as used by Clement's work [18] was left out in the analysis due to its similarity with the mean estimate for this study site.

2.4 Data and Study Site

2.4.1 Sentinel-1 Data Cube

The analysis was performed on a Sentinel-1 SAR backscatter data cube that includes all imagery acquired over the study region from January 2018 to December 2020. The data cube was generated with a dedicated preprocessing engine that ingests Sentinel-1A/B Ground Range Detected (GRD) products, as outlined in detail in Wagner et. al [125]. The preprocessing workflow includes 1) application of precise orbit file, 2) border noise removal, 3) thermal noise reduction, 4) radiometric calibration, 5) range-doppler terrain correction, and 6) resampling and reprojection to the Equi7Grid tiling system [10]. The data cube was abstracted from these hierarchically organized Sentinel-1 images using the yeoda package developed by TU Wien [81]. The backscatter data cube was filtered for VV polarization and Sentinel-1'S relative orbit, to obtain all images from the same observation geometry.

2.4.2 Study Area

The study area is situated on Luzon, the largest and most populous island of the Philippines. The study area extent is defined by the 100 × 100 km-sized tile "E058N117T1" from the

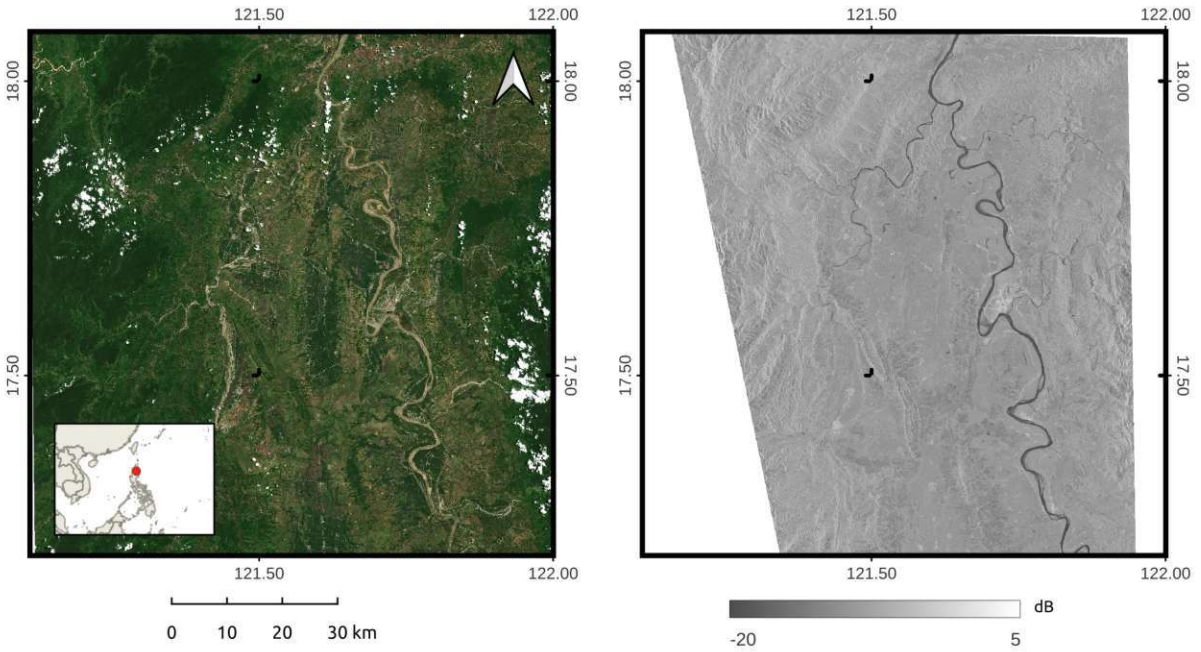

Fig. 2.1: Our study area in the northern Philippines under normal/no-flood conditions as in July 2020. Left: A Sentinel-2 true color image of the tile's area from July 2020. Right: Mean Sigma Nought backscatter value generated from Sentinel-1 data cube, filtered for the relative orbit used for this study's flood event.

Equi7Grid tiling system, shown as the red footprint in Fig. 2.1. The area covers a part of the Cagayan valley, where vast tracks of agricultural fields are situated. The Cagayan River traverses the tile from south to north. Urban settlements can mostly be found near the river, while most of the western portion of the tile is dominated by mountainous terrain. All subsequent analysis in this work were performed at 10×10 m resolution native to this data cube tile[1].

The flooding event investigated in this study was caused by typhoon Vamco that hit the northern Philippines from November 9 to 13, 2020. The typhoon affected more than five million individuals [99], and many along the Cagayan River were flood-stricken. The flood scene for the analysis was captured by Sentinel-1B on the ascending orbit 069 on 13 November 2020 around the time of peak flooding.

2.4.3 Reference Flood Maps

Due to the fleeting nature of floods ground truth is often lacking [40]. This is also the case here, but two satellite-based reference flood maps are available. The first is a flood map (in shapefile format) generated from the same Sentinel-1 flood scene from 13 November 2020 by experts working at the Sentinel Asia [51] who were well familiar with the study area and the flooding caused by the typhoon Vamco[2]. From personal communication with

[1] All collected data are rasterized (if needed) and reprojected to the OC010M_E058N117T1 of Equi7Grid

[2] Sentinel Asia Typhoon Vamco Activation – `https://sentinel-asia.org/EO/2020/article20201111PH.html`

the operators, we know that the Sentinel Asia product was created from the SAR intensity difference, whereas the threshold was manually selected and optimized. However, it should be noted that also the experts at Sentinel Asia did not have access to ground observations.

Sentinel-2 Scene	Description
S2B_MSIL2A_20200909T021609_N0214_R003_T51QUV_20200909T065335	No-flood reference
S2A_MSIL2A_20201113T021941_N0214_R003_T51QUV_20201113T055836	Flood scene

Tab. 2.1: Sentinel-2 data for validation

We generated a second reference flood map, using a pair of optical multispectral images from Sentinel-2 (Table 2.1), one acquired two months before (on 9 September 2020) and one during the flood event (on 13 November 2020). Specifically, we used Level2A (Bottom of Atmosphere) images downloaded from the Copernicus Open Access Hub[3] and processed them using Sentinel-2 toolbox of SNAP v8.0 [27], applying a thick clouds and cirrus cloud mask. Then we computed the Modified Normalized Difference Water Index (MNDWI) that was designed to delineate water and built-up areas [133]. The flood extent was finally derived by comparing the two MNDWI images and fine-tuning the threshold. Due to the significant cloud cover on 13 November 2020, only a portion of the flood scene could be mapped. Fortunately, the main channel of the Cagayan River is cloud-free and offers sufficient samples. While the Sentinel-2 acquisition took place 7 h after Sentinel-1, no major appreciable differences in the flood extent are visible (See Figure 2.2).

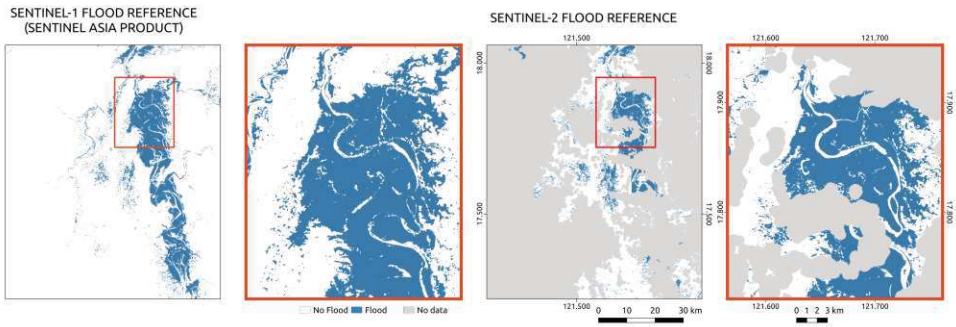

Fig. 2.2: Reference flood maps. Left most flood maps shows the Sentinel-1 based flood map from Sentinel Asia. Right most panels showing the Sentinel-2 derived reference flood map, with cloud-covered areas in gray. Zoomed in map panels showing the high agreement of the flood extents from both reference maps.

2.4.4 Auxiliary Data

The workflows implemented in this work require auxiliary information on topography and geomorphology. In this study, we used the Height Above Nearest Drainange (HAND) Index [82] and the Projected Local Incidence Angle (PLIA) as shown in Figure 2.3. The

[3]Copernicus Open Access Hub– `https://scihub.copernicus.eu/`

HAND index data was derived from the Copernicus Digital Elevation Model (CopDEM GLO-30)[4] upsampled to the resolution of the working tile. The PLIA map was generated as a by-product of the Sentinel-1 pre-processing workflow and is thus stored in the same tile's projection system. The applicability of these auxiliary data - HAND and PLIA are discussed in the following section.

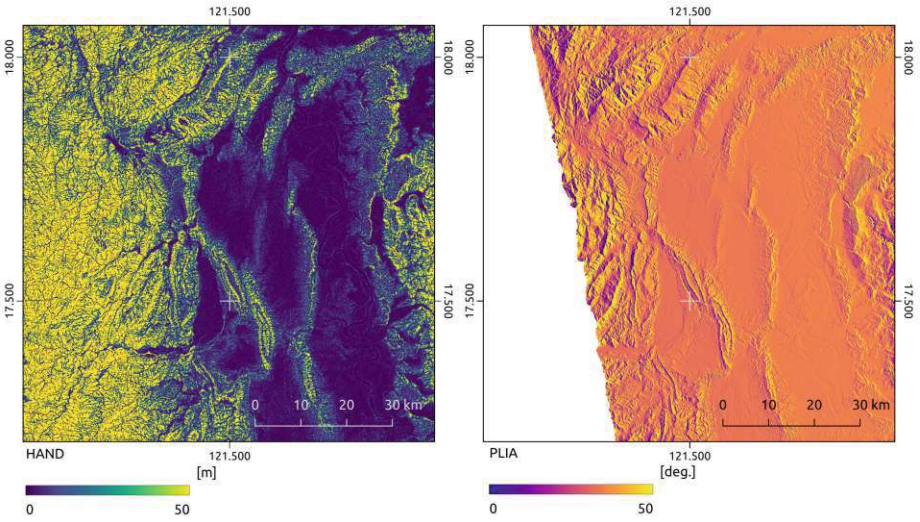

Fig. 2.3: Auxiliary Data. Left panel: map showing the Height Above Nearest Drainange (HAND) Index values. Right panel: map showing the the Projected Local Incidence Angle (PLIA) of the used Sentinel-1 relative orbit.

2.5 Methods

To compare the performance of the four change detection models and their sensitivity to changes in their parameterization, we follow a two step approach: In the first step, we assess for each change detection model separately how different parameterizations impact the results. As we are only interested in the relative performance of the parameterizations when applying the models to Sentinel-1 data, the benchmark in this step is the Sentinel-1 flood map produced by the experts of Sentinel Asia. In the second step, we intercompare the performance of the four change detection models with their best-performing parameterizations by assessing their accuracy against the Sentinel-2 flood map.

The detailed workflow is shown in Figure 2.4. The starting point is the Sentinel-1 backscatter data cube from which all required VV backscatter images from relative orbit 69 and the corresponding projected local incidence angle (PLIA) are extracted. Furthermore, a common set of geomorphological and exclusion masking post-processing steps are applied to all flood maps. First, the Height Above Nearest Drainage (HAND) index is used to mask for terrain distortions in the SAR data, such as radar shadow and layover [48] at a height

[4]Produced using Copernicus WorldDEM-30 © DLR e.V. 2010-2014 and © Airbus Defence and Space GmbH 2014-2018 provided under COPERNICUS by the European Union and ESA; all rights reserved – https://doi.org/10.5270/ESA-c5d3d65

above 20 m (in this case) from drainage. Second, a PLIA mask is applied to remove pixels which have PLIA outside the typical range of incidence angles for flat areas (where floods are typically appearing), following the approach by Bauer-Marschallinger et al. These masks helped to reduce the number of falsely classified flood pixels over the mountainous parts of the study area—which are generally troubling SAR retrievals—thereby slightly improving the accuracy of the flood maps. Lastly, 5×5 spatial majority filters are applied as a morphological correction of salt-and-pepper-like classification coming from SAR signal components unrelated to flood conditions.

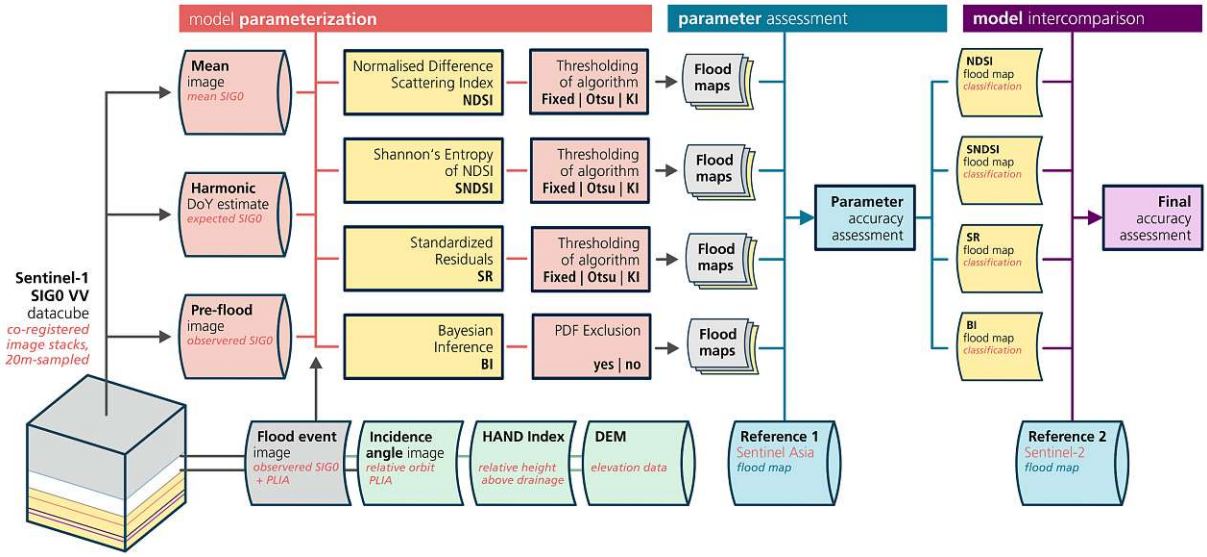

Fig. 2.4: Workflow from Sentinel-1 datacube and derived parameters, joined by auxiliary topography data, to generate and assess the flood maps. For four different change detection models (NDSI, SNDSI, SR and BI), a multitude of different parameterizations are assessed (determined by one out of three no-flood references, as well as by algorithm settings for threshold and exclusion; results in Section 2.6). Best-performing flood maps undergo model inter-comparison in the final stage (see Section 2.7).

2.5.1 Paramterizations

To test the NDSI, SNDSI, and SR models —and their parameterizations— we computed a multitude of flood maps using different combinations of the no-flood reference and the thresholding technique to parameterize the models. Here, we show the results for the combination of three no-flood references and three different thresholds, yielding in total 3 x 3 x 3 = 27 flood maps. With respect to the no-flood reference, the three used parameterizations are:

- **Mean Backscatter**: We computed the mean and standard deviation of σ^0 per pixel over the three year long data record (2018-2020). Note, that while the NDSI and SNDSI only require the mean as input, the SR requires both the mean and $StDev(\sigma^0)$.

- **Harmonic Model**: To account for seasonal signal variations, we fitted a harmonic model to the data record, yielding for each pixel and each day of year (DOY) an estimate of the expected backscatter intensity and its standard deviation respectively. For a detailed description of this Harmonic model formulation we refer the readers to the recent work of Bauer-Marschallinger et al. [8].

- **Pre-flood Image**: A Sentinel-1 image acquired about two weeks before the flood event on 1 November 2020 and from the same relative orbit was selected as no-flood reference of the backscatter intensity. As the SR and BI models also require an estimate of the backscatter dynamics, we compute $StDev(\sigma^0)$, similar to harmonic formulation, using the Root Mean of Square of the difference between backscatter in the time-series data record and the expected no-flood backscatter (from pre-flood image).

The three models NDSI, SNDSI, and SR require a threshold for label pixels as either flood or no-flood. In the course of finding an optimal threshold, we apply the simple pre-filtering technique applied by Schlaffer et al. [101] using the HAND index, where the pixels of high HAND values i.e. HAND $>$ 20, are removed from the histogram before thresholds are determined.

We tested three different methods to determine the threshold:

- **Fixed**: Here we rely on published reports. Among the NDSI and SNDSI implmentations, thresholds from the work of Ulloa et al. [123] were adopted. These are -0.725 for NDSI and 0.78 for SNDSI. While for SR a fixed value of -1.5 was found by several studies to provide good results [18].

- **Otsu**: In the method of Otsu [84], an assumption of bi-modality is followed by fitting two distributions by minimizing intra-class intensity variance. Hence, we determine the threshold from the intersection of the fitted distributions within our reference- and flood-images.

- **Kittler and Illingsworth (KI)**: As an alternative we also tested the KI method [54]. Also known as the Minimum-Error thresholding method, it seeks to fit the two distributions, using the minimum error criterion, to a given model histogram. Hence, the threshold is similarly determined from the intersection of the fitted distributions as with Otsu above.

To test the BI model, we employ the same three no-flood reference parameterizations to derive the full conditional probability function $p(\sigma^0|N)$. While BI does not rely on parameterized thresholds, we test the application (and non-application) of distribution-based masking methods introduced in the previous work of Bauer-Maschallinger et al [8]. Accordingly, the BI method is improved by excluding pixels with high classification uncertainty, either from very similar a-priori distributions for flood and no-flood, or from actual observation values that fall in-between the two. Consequently, the significant probability density function (PDF) overlap between flooded and non-flooded classes, and in this paper, we refer to this as PDF exclusion mask. Hence, for BI we test 1 x 3 x 2 = 6 parameterizations, and finally obtain a set of 33 flood maps for our experiment.

2.5.2 Accuracy Assessment

The flood maps are evaluated by comparing them to the two reference flood maps described in Section 2.4.3. Given that these two expert-produced reference maps also do not represent an absolute "truth", the computed accuracy metrics must be interpreted with some caution. Nonetheless, as we are mostly interested in understanding the relative performances of the algorithms and their parameterizations, they represent a good benchmark.

We computed traditional land cover classification metrics: Overall accuracy (OA), Producer's Accuracy (PA), and User's Accuracy (UA). OA was selected over chance agreement corrected metric i.e. Kappa coefficient, from recommendation in the literature [31, 66]. In addition, we calculate the Critical Success Index (CSI), which is often used in data science and flood mapping work to address the inequality of the classes. CSI has been specifically found to provide good insights for flood mapping accuracy assessments at the same scale [56]. All of these metrics were computed from a binary confusion matrix and its four elements: True Positive (TP), True Negative (TN), False Positive (FP), and False Negative (FN), among classified pixels, according to the following formulas:

$$OA = \frac{TP + TN}{TP + TN + FP + FN} \tag{2.5}$$

$$UA = \frac{TP}{(TP + FP)} \tag{2.6}$$

$$PA = \frac{TP}{(TP + FN)} \tag{2.7}$$

$$CSI = \frac{TP}{(TP + FP + FN)} \tag{2.8}$$

Following good practice examples and sampling size determination equations from Foody's work [32], we acquired a total of 5000 random samples. Independent random samples per change detection model were taken to remove possible bias in the application of model dependent exclusion masks. From this, we surmise that a difference greater than 2% in OA implies a consequential distinction between the results.

2.6 Model Parameter Assessment

In this section, we analyze the sensitivity of the four change detection models to changes in their parameterization by comparing the derived flood maps to the Sentinel-1 reference flood map produced by Sentinel Asia (Sections 2.6.1 to 2.6.4). Furthermore, we select the best performing parameterizations for each method to be subject of our model inter-comparison in Section 2.7.

To allow a well-founded interpretation of the performance of the four models, we first examine their statistical bases used for the distinction between flood and no flood. Figure 2.5 shows the histograms and maps of the observed backscatter σ^0 together with the calculated NDSI, SNDSI, SR, and BI with, as an example, the mean image as no-flood reference. From this compilation, it can be observed that the histograms of the model values

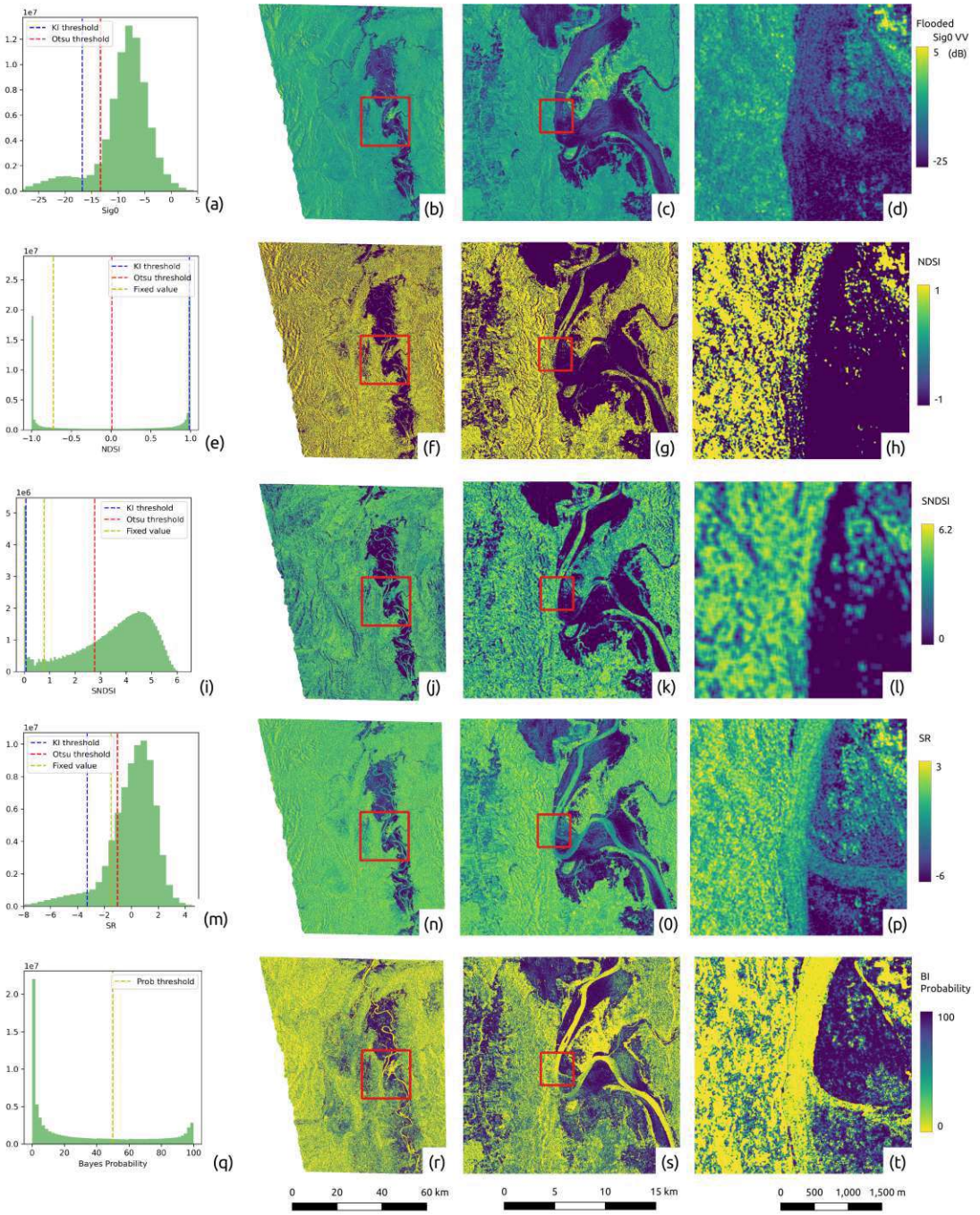

Fig. 2.5: Compilation of Sentinel-1 flood scene and results from the four change detection models, which are parameterized with the mean backscatter as no-flood reference (selected as example in this illustration). Top row (a–d): Sentinel-1 flood image acquired on 13 November 2020, followed by rows for NDSI, SNDSI, SR, and BI values. Leftmost column (a, e, i, m, q): histograms for images in the second column, plus relevant thresholds. 2nd column: maps for the whole extent of the study area tile. 3rd column: corresponding maps zoomed to Tuguegarao City. Rightmost panel: further zooming into the Cagayan River section that is adjacent to the city.

allow in most cases an improved distinction between flooded and non-flooded sections, compared with the initial flooded σ^0 image. Generally, the decrease in backscatter during floods is highlighted, and the change detection models show—as expected—increased image contrast and more distributed histograms. The SR map (Fig. 2.5 m–p), however, appears to highlight different signatures within the observed σ^0 image while not transforming the shape of the histogram. Another observation is that particularly the SR and BI data manage to register the pattern from the permanent water surfaces along the river, thus supporting the delineation against flood bodies.

For the whole area, NDSI (Fig. 2.5 e–h) provides the most considerable increase in the relative spread of values. The SNDSI (Fig. 2.5 i–l) shows less improvement in this regard, but reduces the spatial dispersion of these values compared with NDSI, which structurally features a noise-like spatial pattern (see e.g. in Fig. 2.5 h). Meanwhile, SR shows the least gain in contrast, and we would argue that there is no significant effect on the separability of the classes in its histogram (see in Fig. 2.5 m). This is most apparent in permanent low backscatter areas, such as the river pixels, that are not as well delineated as for the other methods (see in Fig. 2.5 p).

Concerning the threshold parameters (indicated by colored lines in the histograms of Fig. 2.5), specifically for SR and σ^0, we observe that the respective Otsu and KI thresholds follow the same characteristics described by Landuyt et al. The results show more liberal flood labeling for Otsu's method and more conservative labeling using KI. Meanwhile, the NDSI and SNDSI indicate significant variance and instability when it comes to finding the respective thresholds. This could be attributed to the seemingly non-Gaussian distributions of the non-flood class and flood class (as observed in Fig. 2.5 e and i), noting that these thresholding algorithms assume Gaussian distributions.

In the BI model data (Fig. 2.5 q–t), most of the visually perceived flooded areas were successfully assigned with high flood probability. Overall, the Bayes probability values show intriguing results, as the river pixels show a low flood probability in spite of the locally significant distribution overlaps coming from the river/water signature. While this is a positive result, this behavior could easily swing from non-flooded and flooded classes, as seen in the salt and pepper appearance of probability values along the river (see in Fig. 2.5 t). This similar noise-like appearance is also apparent in the probability values found in agricultural areas.

2.6.1 Parameterization of NDSI Model

We now examine the NDSI model and the performance of its different parameterizations. As shown in Table 2.2, the harmonic approach performs best of the no-flood references, while KI performs best of the threshold methods. Consequently, the combination of these two (represented by parameterization no. 6) builds the favored parametrization. This combination features a CSI value larger than 85%. One can observe the significant variance in the UA, ranging from moderate (59%) to excellent performance (97%). In contrast, the PA has smaller differences, with most showing excellent results above 90%. This suggests that the models favor, in general, overestimation. Thus, KI thresholding is a proper method to dampen this effect. One can also notice the erratic performance of the tested thresholding methods for the NDSI model. We attribute this to the fact that the

NDSI histogram does not form a Gaussian distribution, a precondition leading to previous findings as e.g. by Ulloa et al.

PN	No-flood Reference	Threshold	User's Accuracy	Producer's Accuracy	Overall Accuracy	Critical Success Index
1	Mean	Fixed	82.8%	96.0%	88.0%	80.0%
2	Mean	Otsu	76.5%	97.6%	83.8%	75.0%
3	Mean	KI	59.6%	99.4%	66.0%	59.3%
4	Harmonic	Fixed	86.9%	95.4%	90.5%	83.5%
5	Harmonic	Otsu	72.1%	97.8%	80.0%	71.0%
6	Harmonic	KI	97.3%	87.7%	92.6%	85.6%
7	Pre-flood	Fixed	77.2%	94.0%	83.1%	73.6%
8	Pre-flood	Otsu	65.2%	96.6%	72.5%	63.7%
9	Pre-flood	KI	94.8%	87.2%	91.2%	83.2%

Tab. 2.2: Accuracy metrics (in percent) for the nine different parameterizations of the NDSI model. PN - Parameterization number.

2.6.2 SNDSI Parameterization

Similar to NDSI, the harmonic no-flood reference leads to the best performance (see Table 2.3), followed by the pre-flood and the mean reference. The best-performing parameterization combines the harmonic reference and KI thresholding method. However, Otsu's method appears to be the most stable among the thresholding methods, probably due to the fact that SNDSI shows no propensity towards overestimation as the NDSI does. Moreover, using Shannon's entropy appears to be an effective spatial morphological filter to reduce noise-like classification.

PN	No-flood Reference	Threshold	User's Accuracy	Producer's Accuracy	Overall Accuracy	Critical Success Index
1	Mean	Fixed	95.0%	68.7%	82.5%	66.3%
2	Mean	Otsu	81.9%	88.0%	84.3%	73.7%
3	Mean	KI	98.3%	54.0%	76.5%	53.5%
4	Harmonic	Fixed	99.7%	65.8%	82.8%	65.7%
5	Harmonic	Otsu	98.4%	85.6%	92.1%	84.5%
6	Harmonic	KI	95.1%	92.3%	93.8%	88.1%
7	Pre-flood	Fixed	99.7%	63.3%	81.6%	63.2%
8	Pre-flood	Otsu	97.8%	83.9%	91.0%	82.4%
9	Pre-flood	KI	97.1%	85.9%	91.7%	83.7%

Tab. 2.3: Accuracy metrics (in percent) for the nine different parametrizations of the SNDSI model. PN - Parameterization number.

2.6.3 Standardized Residuals Parameterization

In general, aside from UA, SR shows a similar large variance in accuracy metrics of the parameterizations(see Table 2.4). Concerning no-flood reference parameterization, also here the harmonic outperforms mean and pre-flood references. The pre-flood reference does not perform well for this method because of the larger standard deviations in the temporal model for the three-year period we tested. The fixed $SR = -1.5$ threshold shows the best performance for this model in this study site. It shows a slightly better performance compared to Otsu's method, while KI underperforms in this model. Overall, the model leans towards improving UA rather than PA values. The reported propensity towards underestimation by KI's method is apparent for the SR model, as indicated by the lower PA results.

PN	No-flood Reference	Threshold	User's Accuracy	Producer's Accuracy	Overall Accuracy	Critical Success Index
1	Mean	Fixed	97.7%	83.5%	90.8%	81.9%
2	Mean	Otsu	98.1%	81.8%	90.1%	80.6%
3	Mean	KI	99.9%	63.0%	81.5%	63.0%
4	Harmonic	Fixed	96.3%	85.9%	91.3%	83.1%
5	Harmonic	Otsu	98.8%	81.6%	90.3%	80.8%
6	Harmonic	KI	99.9%	64.9%	82.4%	64.9%
7	Pre-flood	Fixed	98.5%	72.5%	85.7%	71.7%
8	Pre-flood	Otsu	99.9%	44.8%	72.4%	44.8%
9	Pre-flood	KI	99.6%	59.9%	79.8%	59.8%

Tab. 2.4: Accuracy metrics (in percent) for the nine different parametrizations of the SR model. PN - Parameterization number.

2.6.4 Bayes Inference Parameterization

In the case of the BI method, no threshold needs to be found, and the general rule of labeling is based on higher probability, i.e., > 50.0 %. Instead, Table 2.5 includes the PDF exclusion (see Section 2.6) as an option. One can see that there are minimal variations in the accuracy metrics for the BI method compared to the other change detection methods. The BI consistently performed very well in terms of UA; almost no non-flooded pixels are labeled as a flood. And slightly lower PA indicates minor underestimation. Furthermore, all parametrizations reached a high CSI larger than 80 %. Overall, the best-performing parameterization No.4 uses the harmonic no-flood reference and the PDF-based exclusion masks from the Bayes model.

Based on the nominal values of OA and CSI, the BI method using harmonic reference slightly outperforms the other no-flood references. It should be noted that these differences are too marginal to conclude a significant distinction. Unlike in other methods, the pre-flood image performs similarly well as the mean and harmonic no-flood reference. It is also noticeable that the introduction of PDF exclusion masking consistently improves the

PN	No-flood Reference	PDF Exclusion	User's Accuracy	Producer's Accuracy	Overall Accuracy	Critical Success Index
1	Mean	No	98.8%	82.0%	90.5%	81.2%
2	Mean	Yes	99.6%	84.9%	91.3%	84.6%
3	Harmonic	No	98.8%	83.4%	91.2%	82.6%
4	Harmonic	Yes	99.8%	84.9%	91.7%	84.8%
5	Pre-flood	No	99.6%	82.9%	90.5%	82.6%
6	Pre-flood	Yes	99.6%	83.7%	91.0%	83.4%

Tab. 2.5: Accuracy metrics (in percent) for the six different parametrizations of the BI model. PN - Parameterization number.

BI model, albeit by small margins in CSI and OA. This, however, comes at the cost of masking some areas that could not be reliably classified.

2.6.5 Parameterization Summary

Table 2.6 collects the best-performing parameterization for each change detection model. All four models perform best with the harmonic model for the no-flood reference. The mean and pre-flood no-flood references performed variably depending on the other parameters. Concerning threshold method, KI's method performed the best for NDSI and SNDSI. Despite KI's method being found to be more conservative in thresholding [56], it performs best for certain instances due to improved separability of flood and non-flood pixels in the models (see histograms in Figure 2.5). For the SR model, however, the fixed threshold was found to provide consistently good results for this study site, while KI and Otsu depend on the no-flood reference. While Otsu's method is not present within the collection of best-performing parameterizations, it shows less variance in performance compared to KI. This result is consistent with reports of Otsu's performance [56]; here, significant flooding is apparent in the study site. Thus its propensity to overestimate floods is not as pronounced. Lastly, the application PDF Exclusion step consistently improves the accuracy metrics for BI, albeit by only small percentage points.

Tab. 2.6: Best Performing Method Parameterization.

Method	No-flood Reference	Threshold
NDSI 6	Harmonic	KI
SNDSI 6	Harmonic	KI
SR 4	Harmonic	Fixed
Method	**No-flood Reference**	**PDF Exclusion**
Bayes 4	Harmonic	yes

After comparing different parameterizations for each change detection method, we infer the robustness of the methods for this study site given by the variability of the resulting

accuracy metrics. The highest robustness is shown by the BI method. We suspect that the use of statistical distributions instead of a particular threshold is responsible for the superior robustness.

2.7 Model Intercomparison

The optimal parameterizations for each of the four change detection methods are identified in Section 2.6 and are summarized in Table 2.6. These are considered in the subsequent step, where the accuracy assessment metrics are computed against the Sentinel-2 flood map (see Table 2.7).

Tab. 2.7: Method Comparisons Sentinel-2 flood result as reference.

Method	Users Accuracy	Producers Accuracy	Overall Accuracy	Critical Success Index
NDSI 6	92.6%	72.2%	83.2%	68.2%
SNDSI 6	87.7%	77.0%	83.1%	69.5%
SR 4	91.8%	69.8%	81.8%	65.7%
BI 4	95.9%	74.6%	85.3%	72.3%

After parameter optimization, there are generally few false positive pixels in the SAR-based flood maps, as all selected flood maps show User's Accuracy (UA) values greater than 87%. The Bayes method used has the highest value of 95.9%. As expected, the PA of all methods is significantly lower than UA. The PA results range from SNDSI with 77.0% to SR with 69.8%. Based on our assumption that there is no significant difference in the flood extent due to little time lag between the Sentinel-1 observation and the Sentinel-2-based reference map, this result can be attributed to the limitation of SAR-based methods over certain land cover types. As reported already by Bauer-Marschallinger et. al [8], the SAR-based flood mapping is challenged in densely vegetated and urban areas, where optical systems such as Sentinel-2 can detect floods under good circumstances and in the absence of clouds.

The OA results indicate good or excellent general agreement between the tested flood maps and the reference maps, which is also promoted by the overall large area and the relatively large flooding event. Among the selected parameterizations, the Bayes method shows the highest OA value with 85.3%, while the last-ranked method SR has only a difference of 3.5%. Based on the little differences in OA, it can be said that BI has the only noteworthy difference from the other methods tested based on 2% difference criteria we established in Section 2.5.2. When examining the Critical Success Index (CSI) results, the Bayes method is also ranked best with 72.3%, followed by the SNDSI with 69.5%, NDSI with 68.2%, and SR with the lowest result at 65.7%. Only the BI method has CSI greater than 70.0%, while all others are rated closely. However, in reflection of the underlying differences in flood mapping mechanisms between optical and SAR-based maps, we consider all methods to perform well.

It should be noted that above's statistical metrics show a generalized performance description for the whole scene. Therefore, we have a closer look at the qualitative differences for some selected areas. PA and UA relate to classification pixels of false negatives (omission errors) and false positives (commission errors), which describe (dis-) agreement well when zoomed in on particular areas of interest. Figures 2.6 and 2.7 show representative subsets and their confusion maps between the tested model's flood maps and the Sentinel-2 reference map. These maps highlight the area near the city of Tuguegarao with its meandering river channel and surrounding agricultural areas, respectively.

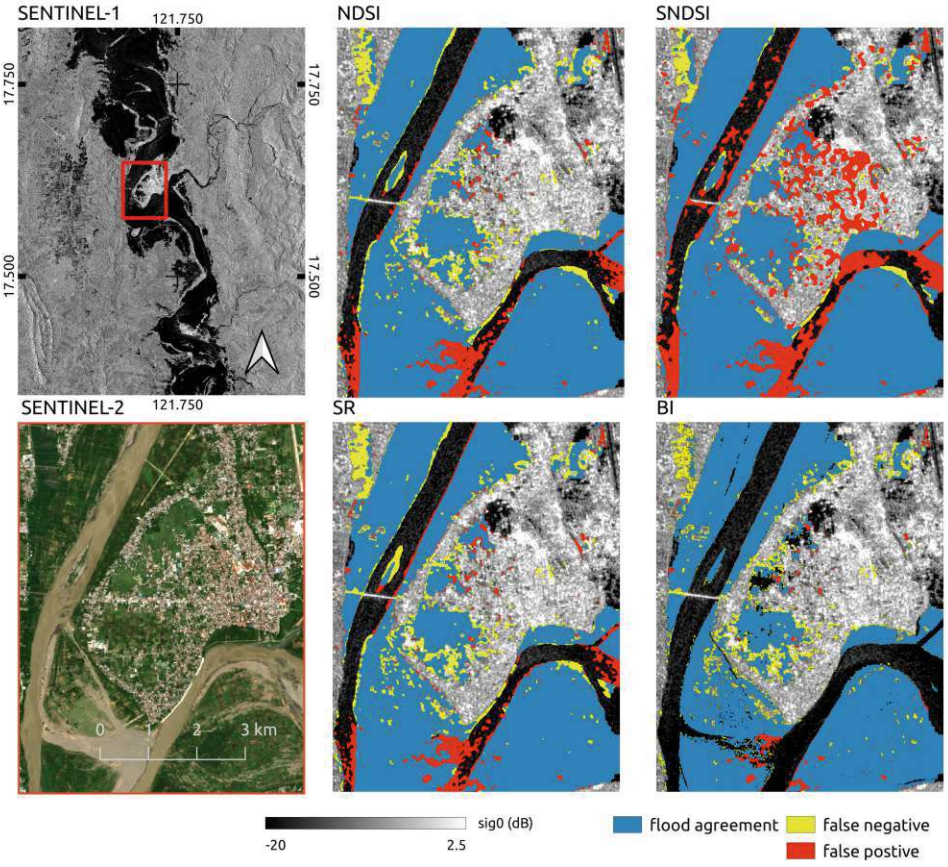

Fig. 2.6: Spatial detail from model inter-comparison for the vicinity of Tuguegarao City. Top left: Sentinel-1 scene from flood event on 13 November 2020 at larger scale, with zoom-in-box for other panels. Bottom left: clear-sky, no-flood Sentinel-2 image (for orientation). Other panels show, overlaid to the Sentinel-1 observation, the confusion maps for NDSI, SNDSI, SR, and BI, indicating areas where algorithm classify false negatives (omission errors) and false positives (commission errors) against the Sentinel-2 reference flood map.

The four methods successfully remove non-water areas of permanent low backscatter, such as the Cagayan airport shown in the upper right edge of the maps in Figure 2.6, fully exploiting the strength of the change detection concept. Moreover, the BI method shows an excellent delineation of the permanent river courses, being excluded in the flood result through the PDF exclusion approach. The SR method shows suitable results for

permanent water exclusion but could be improved by further morphological operators as only small patches are observed. The NDSI-based results, show poor performance in this regard.

In contrast to the other models, SNDSI shows larger patches of false positives over the built-up areas in the center and east of the zoom-in (Figure 2.6). In this area, high backscatter from double bounce effects are clustered, which results in low entropy values that lead to erroneous labeling. The observed improvement in the NDSI and SNDSI in parameter transformation for thresholding does not significantly improve these methods compared to the other tested methods. This degraded performance could be attributed to the limitation of the parameter formulation to account for false positives, which are clearly seen in the confusion maps. For example, low SNDSI values mainly refer to swaths of water in an image, but are also likely for radar shadows which may have been missed by the post-processing masks. Another observation is the NDSI, and SNDSI results have more overestimation in flooded agricultural areas(Figure 2.7), while the SR and BI methods are less prone to this type of commission error.

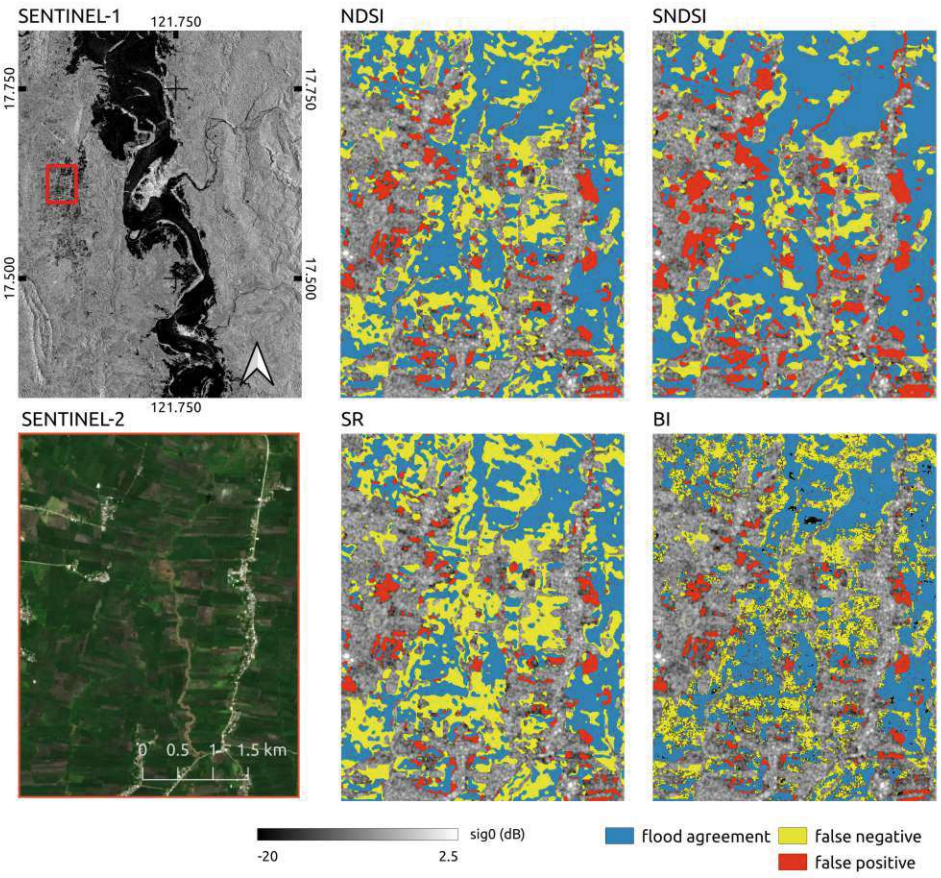

Fig. 2.7: As Figure 2.6, but a spatial detail on agricultural areas.

As also seen in Table 2.7, SR has notably more false negatives. These are generally observed in agricultural areas, as exemplified in Figure 2.7, and can be attributed to the higher temporal variance from agricultural activities (in the historical time series), which dampens the SR parameter. Surprisingly, the BI method performs better than the other

methods, considering that agricultural areas were recognized in need of improvement for the BI method presented by Bauer-Marschallinger et al.

In terms of spatial cohesion of the flood maps, as inferred from the confusion maps in Figures 2.6 and 2.7, the SNDSI and BI method show more cohesive overall results. For the area of Tuguegarao, Figure 2.6, the NDSI map shows noisy or patchy results in terms of higher rates of both FP and FN, while SR has the same concern to a lesser degree in the specific regions. At the same time, Figure 2.7 show much noise in all methods, including the BI result illustrating the challenges of such areas in flood mapping. It could be argued that NDSI and SR methods could further be improved with better morphological filtering during a post-processing step. Alternatively, by use of Shannon's entropy as in the SNDSI, a filter-like improvement is achieved, which slightly improves the overall result for this case study.

However, notable in the BI result in Figure 2.7 are the patches of excluded areas. While in most cases, these coincide with misclassifications in the other maps, thus highlighting the PDF exclusion's effectiveness. For example, some areas such as the old river meander in the lower left corner of the BI map in Figure 2.6 were excluded rather than labeled being as flood. Despite this and other things considered, the BI method generally performs better than the other methods tested in this study.

2.8 Conclusions

This study tested and compared four automated SAR-based change detection flood mapping methods and their parameterization against Sentinel-1-based expert data for the case study in the northern Philippines. Our parameterization experiments comprise the testing of different threshold and masking options, as well as the suitability of three different methods to generate the no-flood-reference map, which is crucial to any change detection approach. We further carried out an inter-comparison of the four best-performing model parameterizations, with accuracy assessment against a Sentinel-2-based flood map specifically generated for this study.

In our assessment of the model parameterizations against the semi-manual results from Sentinel Asia (using Sentinel-1), the Bayes Inference (BI) method showed the most consistent performance, regardless of the input no-flood reference. The BI model was found to be robust in the sense that it does not require tailor-fitting, whereas the other change detection methods were found to be more significantly impacted by one's choice of input non-flood reference and the thresholding method. Focusing on the latter, Otsu's method was found to work well with the SR and SNDSI methods. In contrast, KI's method showed a better result for NDSI and SNDSI, albeit showing highly variable results when the input no-flood reference is changed. The published threshold of $SR \equiv -1.5$ also showed a good result for this study area. Lastly, considering that we applied a HAND-based prefiltering before thresholding and the obtained variability of the results, it is recommended to explore spatial prefiltering techniques with these models, which are driven by temporal parameters.

Concerning the no-flood-reference parameterization, the harmonic model lead to the best results for all four change detection models, apparently profiting from the good fit of the seasonally expected backscatter. The missing consideration of the backscatter's seasonal variability causes the lower performance of the mean. The pre-flood image is generally

observed close to the flood event and hence is expected to represent actual conditions like vegetation state or soil moisture most accurately. Nevertheless, results from the pre-flood-parameterized models are less consistent compared to the harmonic model. We found that the pre-flood image—as an actual single-time observation—still holds speckle that leads to noise-like classifications, which is effectively removed in no-flood references made from temporal aggregations. Therefore, we recommended that the datacube-derived no-flood reference are further investigated, such as other time-series models, e.g., exponential filters, or parameter tuning through, e.g., modulating the length of the contributing time-series.

The evaluation of the best-performing model parameterizations against the optical-derived Sentinel-2 reference showed that the BI method performed best. Considering the parameterization results and this final comparison suggest that the BI core concept is generally more robust and possibly more adaptable to other study sites. Albeit computationally more demanding, the BI approach of taking the sample's full distribution into account proves to be more adaptive than the discrete thresholding in the other methods.

All tested datacube flood mapping methods show meaningful agreement with the reference flood maps from Sentinel-2 and a semi-automatic expert product by Sentinel Asia. The best-performing methods all achieved good to excellent results based on OA and CSI. The four tested change detection methods show very satisfying User's Accuracies, mainly through a correct classification of permanent low backscatter areas. The Producer's Accuracies, on the other hand, also had reasonable performance but exhibit well-known SAR-related deficiencies over challenging land covers.

To summarize, this study represents one of the first efforts to inter-compare several SAR change-detection-based flood mapping methods and their parameterizations, with a view on the feasibility of applying them in an operational fashion over large areas. Overall, all four change detection models performed reasonably well considering that their input parameters were neither locally optimized nor adapted by a human operator. Nonetheless, the sensitivity of the NSDI, SNSRI, and SR models to parameterizations suggests the need for further localized tests. On the other hand, the Bayesian Inference model coupled with the harmonic model as no-flood reference seems to be relatively stable in its performance, which is an important prerequisite for (global) automatic operations.

2.9 Acknowledgments

The computational results presented have been achieved using inter alia the Vienna Scientific Cluster (VSC). We would further like to thank our colleagues at TU Wien and EODC for supporting us on technical tasks on maintaining the datacube.

Special thanks is given to Chathumal Madhuranga of the Geoinformatic Center - Aisan Institute of Technology (GIC-AIT) for his valuable insights on the Sentinel Asia flood products. GIC-AIT acts as a Primary Data Analyzing node for Sentinel Asia.

2.9.1 Funding

This research work was performed with support of the Engineering Research & Development for Technology Program of the Philippine Department of Science and Technology, the project "S1Floods.AT" (Grant no. BW000028378) founded by the Austrian Rsearch

Promotion Agency (FFG) and the project "Provision of an Automated, Global, Satellite-based Flood Monitoring Product for the Copernicus Emergency Management Service" (GFM), Contract No. 939866-IPR-2020 for the European Commission's Joint Research Centre (EC-JRC). The authors acknowledge TU Wien Bibliothek for financial support through its Open Access Funding by TU Wien.

2.9.2 Data Avialability

The data presented in this study are openly available at:
`https://github.com/marxt/dc-flood-mapping-comp-ph`

Chapter 3

Improving Sentinel-1 Flood Maps Using a Topographic Index as Prior in Bayesian Inference

This chapter is a reformatted accepted version of:
Tupas, M. E., Roth, F., Bauer-Marschallinger, B., & Wagner, W. (2023). Improving Sentinel-1 Flood Maps Using a Topographic Index as Prior in Bayesian Inference. Water, 15(23), Article 23. https://doi.org/10.3390/w15234034

3.1 Abstract

Sentinel-1-based flood mapping works well but with well-known issues over rugged terrain. Applying exclusion masks to improve results is common practice in unsupervised and global applications. One such mask is the Height Above the Nearest Drainage (HAND), which uses terrain information to reduce flood look-a-likes in SAR images. The TU Wien flood mapping algorithm is one operational workflow using this mask. Being a Bayesian method, this algorithm can integrate auxiliary information as prior probabilities to improve classifications. This work improves the TU Wien flood mapping algorithm by introducing a HAND prior function instead of using it as a mask. We estimate optimal function parameters and observe the performance in flooded and non-flooded scenarios in six study sites. We compare the flood maps generated with HAND and (baseline) non-informed priors with reference CEMS Rapid mapping flood extents. Our results show enhanced performance by decreasing false negatives at the cost of slightly increasing false positives. In utilizing a single parametrization, the improved algorithm shows potential for global implementation.

Keywords: Synthetic Aperture Radar; Sentinel-1; Flood Mapping; Bayes' Inference; Hand Above Nearest Drainage

3.2 Introduction

In recent years, Earth-observation-based mapping and monitoring of floods has increasingly utilized Synthetic Aperture Radar (SAR) data [2]. This situation can be attributed to the excellent systematic acquisition capabilities of the Copernicus Sentinel-1 mission [79]. In the past two years alone, multiple large-scale flood events have been monitored and analyzed in unprecedented detail using SAR-based methods. [1, 97]. These methods must work on time and provide accurate results, giving decision-makers actionable information for disaster relief, recovery, and reconstruction [21].

Previous studies have demonstrated SAR-based flood mapping workflows to work well but with some well-known limitations [12, 73, 90, 105, 120, 132]. Problems arise in areas where SAR data (only) flood retrievals become ambiguous. Examples are other low backscatter areas, such as radar shadows regions; or no sensitivity areas like dense vegetation. In some studies, localized parameterizations (e.g., changing thresholds) or more complex methods [61, 65, 70, 114, 136] address these concerns but are seldom near-real-time (NRT) or globally viable.

Other workflows rely on exclusion masking of these problematic areas [120, 140]. While masking is a reasonable solution, over-application is a concern and should be minimized. One commonly used masking method that minimizes misclassification of SAR flood look-a-likes uses the Height Above the Nearest Drainage (HAND) index [82, 95]. HAND masking, while known to work well in removing false positives based on topography [48, 120], often affects significant portions of a flood scene rendering the mapping algorithm futile for these parts. Despite this concern, HAND masking's simple execution and robust global performance make it an ideal inclusion to operational workflows [16].

One flood mapping algorithm in operational use for the new Global Flood Monitoring service [98] of the Copernicus Emergency Management Service (CEMS, `https://emergency.copernicus.eu/`) is the TU Wien flood mapping algorithm. This method is based on a probabilistic Bayesian method [8] that can integrate pre-existing information (from auxiliary sources) to arrive at improved decisions or classifications. However, using other information to form prior probabilities (or *priors* for short) is often overlooked in SAR-based flood mapping efforts in favor of non-informed priors [34]. In doing so, they miss the potential to improve areas where SAR backscatter alone is ambiguous or problematic. With limited studies having shown success [21, 94] and others presenting evidence to the contrary [34] a systematic study of priors in Bayesian SAR-based flood mapping is needed.

This work aims to improve to the TU Wien flood mapping algorithm. To accomplish this, instead of using it for masking, we leverage the HAND index to derive priors. We introduce a HAND prior probability function, deriving globally applicable parameters, and showing its performance on flooded and non-flooded cases in six study sites across the globe.

3.3 Height Above the Nearest Drainage As A Prior

3.3.1 SAR flood mapping using Bayes Inference

Bayesian classifiers are probabilistic classifiers that apply Bayes' Theorem. In Earth observation applications, particularly flood mapping applications, these classifiers are usually applied on the pixel level. Pixels are classified as flooded when the probability after inference, or the so-called posterior probability, exceeds a pre-defined threshold (usually 50%). One can calculate the posterior probabilities from Bayes' Inference using:

$$p(F|\sigma^0) = \frac{p(\sigma^0|F)p(F)}{p(\sigma^0|F)p(F) + p(\sigma^0|N)p(N)} \tag{3.1}$$

where $p(\sigma^0|N)$ is the conditional probability for a pixel being non-flooded and $p(\sigma^0|F)$ for the flooded case, while $p(F)$ and $p(N)$ are the prior probabilities of a pixel being flooded and non-flooded respectively. Most literature has focused on formulating the conditional probability functions, using:

- *Observed SAR parameter*: backscatter intensity [8, 34], backscatter difference [100], or coherence [94];
- *Probability distribution models*: Gaussian [8, 94, 100, 106] against non-gaussian ([34];
- *Data set used as a reference for flooded probability distribution*: scene based [34, 94, 106], or historically sampled [8, 100];
- *Data set used as a reference for non-flooded probability distribution*: scene based [34, 94, 106], against time-series derived [8, 100].

In the case of the TU Wien algorithm [8] tested in this work, $p(\sigma^0|N)$ is derived from a harmonic model describing the local VV backscatter, expressed as expected sigma-naught

value (σ^0 or SIG0) for a given day-of-year. $p(\sigma^0|F)$ is estimated from calm water samples, taken at different locations over sea and lakes at times without strong winds.

On the other hand, prior probabilities are often reduced to the non-informative case [100, 129] i.e., equal chance of being flooded and non-flooded. Giustarini et al. justified this assertion by testing varying prior probability values without significantly affecting the reliability metric of their flood maps [34]. Further testing priors based on flooded area percentages from reference datasets also did not significantly improve the results in their study. However, their study applied prior values uniformly across their study areas and did not investigate priors that spatially vary.

Reffice et al. discuss the possibilities of such localized priors in their work [94]. Their work demonstrates a prior probability distribution function from the inverse distance to rivers. Moreover, their subsequent work with a Bayesian Network included a piece-wise geomorphic-flooding-index-based function as an auxiliary input [21]. While both functions offer simple solutions, their approach involves localized optimization of their proposed functions.

3.3.2 HAND Based Prior Probability Function

HAND is a hydrological model derived from terrain data such as Digital Elevation Models (DEMs) [82]. As an index, it is often utilized in SAR-based flood methods to exclude improbable flooded pixels [86], specifically for low-backscatter pixels above a pre-defined height threshold relative to the nearest drainage level. While in machine learning-based flood mapping algorithms, it has also been used as an auxiliary input [62]. Notably, flood modelers use HAND with synthetic rating curves for rapid inundation mapping [36, 49, 63], and has been touted for its performance despite its simplicity.

Our hypothesis is that the HAND index is an ideal candidate prior information in the global operational context because: 1) as there are several (near-) globally DEMs openly available it can be computed globally [29, 134], 2) it is a simple model (applied the same way everywhere), and 3) it does not require regular updates (since most terrains are primarily stable).

Considering this, we conceptualize a prior probability function that shares HAND's robustness and simplicity. Thus, only the HAND index is used as an input in our Bayes' Inference formulation to estimate flooded prior probabilities, $p(F)$, while the non-flooded prior, $p(N)$, is computed from 1 - $p(F)$. For $p(F)$, we propose an exponential function $p(F|h)$ given as follows:

$$p(F|h) = \frac{1}{1 + e^{\frac{(h-\mu)}{\sigma}}} \tag{3.2}$$

where h = HAND index value per pixel
μ = midpoint
σ = steepness

The midpoint (μ) defines the HAND value where the probability indicates a 50% chance of the pixel being labeled as water. In contrast, the steepness parameter (σ) dictates the degree to which the resulting probability changes per increase in HAND value, essentially

controlling the function's characteristic shape. A lower σ value (e.g. $\sigma < 1$) results in a function behaving like a step(down)-function, while a higher σ value (e.g. $\sigma > 30$) leads to an almost linearly decreasing function.

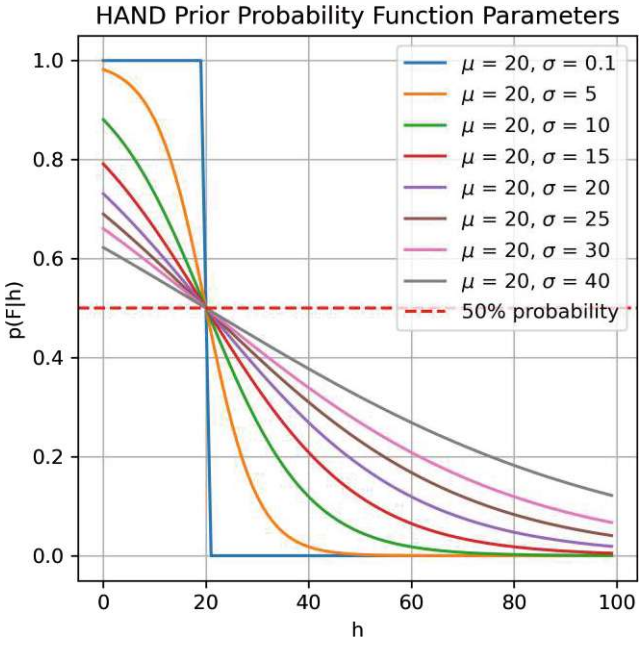

Fig. 3.1: HAND prior probability function response to varying steepness (σ) at mid-point (μ) = 20. Y-axis indicates the probability– p(F|h). X-axis indicates the HAND values (h).

Figure 3.1 illustrates the response of the proposed function to varying steepness parameter, here centered at $\mu = 20$. This exponential formulation models a gentle decrease in probabilities at lower HAND values where flooding is more likely to occur; while having steeper decline towards the midpoint where floods are less likely to happen.

Similar exponential functions have been proposed by Refice et al. for their distance to river function [94] and Jafarzadegan et al. for their log-normal flood probability function used for HAND-based flood mapping [49]. The latter reports a similar function being stable during parameter optimization –showing robustness to parameterization, a preferred characteristic for global operations [117].

3.4 Materials and Methods

3.4.1 Study Sites

To test the performance of Bayesian flood mapping with HAND priors, we analyzed flood events and no-flood cases at six test sites covering different geographical regions, climatic conditions, and terrain properties. Details are described in Section 3.5.2. Table 3.1 shows an overview of these six test sites.

The flood events were identified from available Copernicus Emergency Management Service (CEMS) [128] Rapid mapping activation covering flood events mapped with Sentinel-1 as satellite data input from March to November 2022. This ensured having reference flood extents for our analysis that matches our generated flood maps exactly spatially (minimal resolution and sampling effects) and temporally (no time lags).

Tab. 3.1: Test Sites and Matching CEMS Activations with Flood Event Dates and No Flood Dates.

CEMS Activation	Type	Location	Flood Event Date	No-flood Date
EMSR569	Flood	Valencia, Spain	22/03/2022	21/03/2021
EMSR577	Flood	Suriname	16/06/2022	09/06/2021
EMSR586	Flood	New South Wales, Australia	05/07/2022	16/06/2021
EMSR637	Flood	New South Wales, Australia	24/10/2022	17/10/2021
EMSR639	Flood	Belize	03/11/2022	27/10/2021
EMSR640	Flood	Scotland, United Kingdom	20/11/2022	25/11/2021

3.4.2 Materials

3.4.2.1 Sentinel-1 Datacube

The Sentinel-1 datacube curated and managed by TU Wien and EODC [125] serves as the primary data source for the Bayesian flood mapping workflow [8] employed in this study. This data cube was generated from Sentinel-1 Ground Range Detected (GRD) datasets [113], which are sampled at 20m x 20m pixel size and and tiled at the T3 tiling level (300km extents) of the Equi7Grid system [10]. The matching SAR images with the VV polarization band for the six flood events were queried from this data cube. Harmonic parameters were also derived from this datacube [115] to estimate the day-of-year no flood reference for the pixel-based flood inference.

3.4.2.2 Height Above the Nearest Drainage

Deriving the HAND index is a reasonably straightforward raster-based methodology using hydrologically conditioned Digital Elevation Models [82]. While several global HAND datasets are openly available [26, 134], we computed HAND index datasets from 90m SRTM [29] using a python script with ArcGIS 'Spatial Analyst Tools.tbx' and 'Topography Tools 10_2_1.tbx'. This dataset was resampled at 20m resolution and tiled to align with the Sentinel-1 datacube.

Locally improving HAND by optimizing the contributing drainage area is recommended [134]. However, good performance as an exclusion mask with global parameters [16] has been shown to work for SAR-based flood mapping without such optimization. Thus no localized optimizations were undertaken.

3.4.2.3 Reference Flood Extents

Obtaining ground truth data for flood mapping is not always possible [40]. A reasonable alternative is using existing, manually quality-controlled flood extent maps, such as those made available through CEMS. Using the criteria described in Section 3.4.1, CEMS reference vector flood extents and associated ancillary data (e.g. AOI, Hydrology) [50] were downloaded from https://emergency.copernicus.eu/. The downloaded reference datasets were subsequently rasterized, reprojected to the Equi7grid tiles, and masked to match the Area of Interest (AOI) in preparation for the assessments. To better match the flood maps generated with the CEMS flood reference, we use the same CEMS hydrology dataset (rivers, lakes) as water mask to differentiate flood from permanently inundated areas [130].

3.4.3 HAND Prior Probability Function Parameter Estimation

First, we determine globally appropriate midpoint (μ) and steepness (σ) parameters for the HAND prior probability function through the iteration and analysis of the average Critical Success Index (CSI), Users Accuracy (UA) and Producers Accuracy (PA) of all test sites relative to their CEMS counterparts.

CSI, defined by Equation 3.3, is used because it is a robust estimator of overall flood map performance [56]. Furthermore UA and PA, defined by Equations 3.4 and 3.5, are also used to discern over- and under-estimation tendencies of the proposed improvement. While no assessment metric is without issues, these metrics were selected to reduce dependence on the size of flood extents[107]. These metrics are computed from the binary confusion matrix of a classified map versus a reference. All assessment metrics are defined by four binary confusion matrix elements, namely: True Positive (TP), True Negative (TN), False Positive (FP), and False Negative (FN).

$$CSI = \frac{TP}{(TP + FP + FN)} \tag{3.3}$$

$$UA = \frac{TP}{(TP + FP)} \tag{3.4}$$

$$PA = \frac{TP}{(TP + FN)} \tag{3.5}$$

Given the definition of the midpoint (μ), we selected our iteration range based on the published values used as HAND exclusion mask thresholds. With typical optimization ranges from 5 to 40 meters, and selected values range from 10m to 20m [49, 87, 114]. Value ranges in the same magnitude are tested for the steepness (σ) to maintain reasonable steepness of the resulting function.

For each combination of these two parameters, spatially varying HAND-based prior probabilities are computed for flood map generation. Then the accuracy metrics (against the CEMS reference) are computed, tabulated, and averaged per parameter combination for all test sites. Finally, estimated optimal parameters are selected based on the maximization of the three metrics.

3.4.4 Comparative Performance

Using the determined HAND function, we can compare the flood maps generated with non-informed prior and HAND-derived prior probabilities cases to show their performance in flooded and non-flooded scenarios. Fig 3.2 shows the TU Wien flood mapping flowcharts of the two cases, highlighting the difference between the two workflows consisting of 1) type of input priors and 2) (non-)removal of the HAND mask post-processing step.

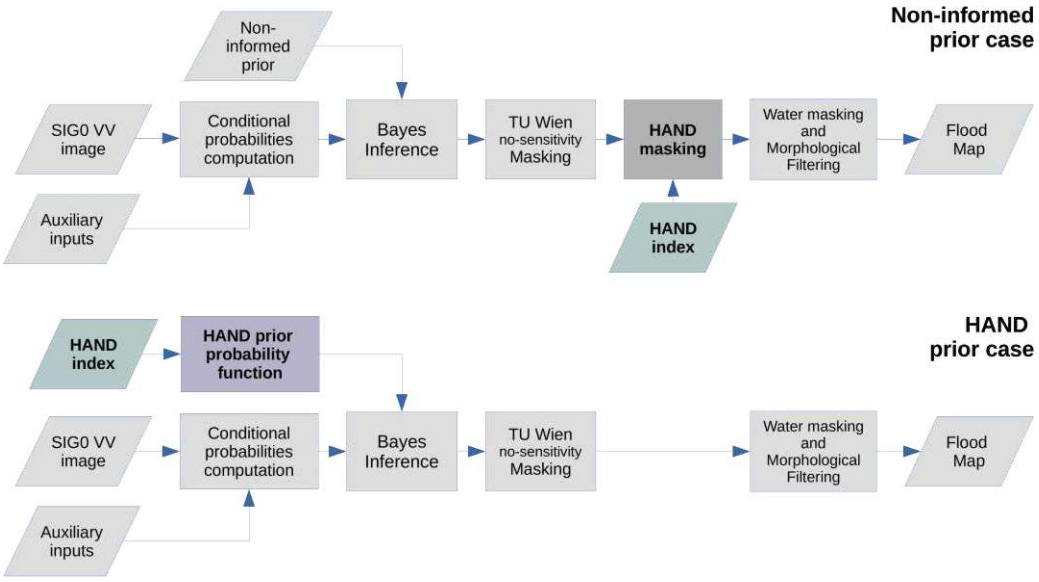

Fig. 3.2: Simplified TU Wien Flood mapping flowcharts. Non-informed prior probability case (above). HAND prior probability case (below). Details of the other auxiliary inputs and the TU Wien no-sensitivity and probability distribution-based masking workflow are detailed in the work of Bauer-Maschallinger et al. [8].

As earlier described, raster-based prior probabilities are generated from the HAND dataset using Equation 3.2. These prior probabilities are used for the first set of test cases, which we refer to as the HAND prior cases. In contrast, a spatially uniform 0.5 prior probability is used for the second set of test cases for the non-informed prior cases. HAND exclusion masks (using the matching μ) are applied as a post-processing step for non-informed prior cases, while this is skipped for the maps computed with HAND prior cases.

Flood maps with both prior cases were generated for flooded scene scenarios, covering the six flood events. We then compute the (above-mentioned) assessment metrics against the matching pre-processed reference CEMS flood data. After this, we examine the differences in the three metrics between the prior probability cases. Exemplary confusion maps of each site are also created to qualify these differences.

In many cases, flood mapping algorithms are tailor-fitted to work for flooded scenes, which may have a negative effect for monitoring non-flooded scenarios. If an algorithm is applied to a non-flooded image, false positives should not be excessive to give the

impression of a scene being flooded. This is important for global monitoring applications where not all results can be manually vetted.

However, in non-flooded scenarios, we lack true positives; thus, the CSI, UA, and PA metrics are not applicable. In their place, we calculate the False Positive Rate (FPR) [6] defined by Equation 3.6 for maps using both prior cases on exemplary non-flooded images for the same study sites. Here the binary confusion matrix is generated with a synthetic all no-flood pixels as reference. In effect, all identified floods are false positives, while non-flooded pixels are true negatives.

$$FPR = \frac{FP}{FP + TN} \tag{3.6}$$

The exemplary images are selected to match the same vegetation state as the flooded images. Thus images approximately one year earlier are identified and matched by orbit to ensure almost identical imaging geometry. These image acquisition dates are noted in Table 3.1. While not explicitly screened, no extraneous SAR effects (abnormally high or low backscatter for a scene caused by extremely wet, dry, or windy conditions) were observed in the selected images.

3.5 Results and Discussions

3.5.1 Prior Probability Parameterization

We averaged the CSI, UA, and PA of all six sites across all the parameter iterations to discern an optimal estimate of the function parameters μ and σ. As noted earlier, the function response does not significantly change for small parameter changes; hence for our purpose, the iteration by 5m of both parameters up to 40m –leading to 64 combinations– is adequate to arrive at a reasonable estimate of the HAND prior probability function. We plot the metrics for all the combinations for the HAND-based prior function and the non-informed prior case as a reference.

As seen in Figure 3.3, panel (**a**), the best average CSI values were observed with μ between 20 - 35 meters and σ between 5 to 10 meters. Moreover, the highest CSI was observed with $\mu = 30m$ and $\sigma = 10m$. It should be noted that the CEMS rapid mapping activation uses both VV and VH bands [50], while this study focuses on the existing TU Wien workflow using VV polarization only, which could explain the low average CSI values. (We scrutinize these further on a study site basis in Section 3.5.2.) In terms of thresholding, VH polarization has a slight advantage in mapping complex floods or transition areas as it more likely exhibits a decrease in backscatter intensity compared to VV polarization that is more sensitive to complex scattering mechanism [46].

As our objective for this study is to improve the algorithm, the absolute CSI values are less important than the observed difference compared with the baseline non-informed prior case. For reference, overall accuracy values in all test cases for all sites exceeded 87%. They were not presented here for brevity, as the CSI is sufficient to highlight the differences in the overall performance.

On the other hand, the HAND prior parameter combinations and reference non-informed prior results have in general high UA values but show significantly lower values at low σ

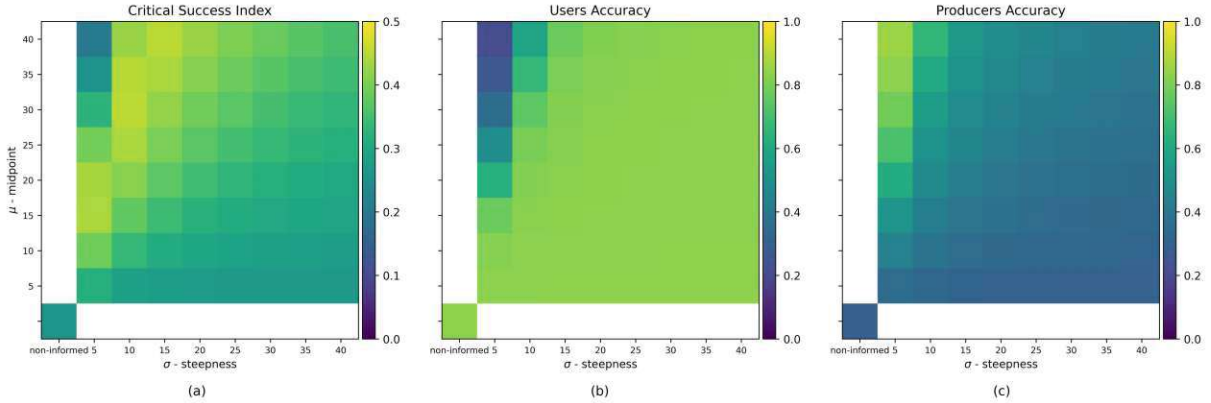

Fig. 3.3: The average comparative metrics of the study sites versus the prior probability function parameterizations. (**a**) Average Critical Success Index, (**b**) Average the Users Accuracy, and (**c**) Average Producers Accuracy. Y-axis indicates the mid-point (μ). X-axis indicates the steepness (σ). The lower left panel shows the non-informed prior case for reference.

values. PA values, similar to CSI, are not ideal. Most combinations do not significantly change the UA (**b**). Furthermore, a significant decrease in the UA is observed at σ between 5 to 10, with a reasonable decrease at μ less than 25. Lastly, the PA plot in panel (**c**) show an increasing value with μ but a decreasing value with σ.

Since no combination shows a clear maximum for all three metrics, we can limit the parameters selection to $\mu = 25$ and $\sigma = 10$ or $\mu = 20$ and $\sigma = 10$ to minimize the decrease in UA while retaining good CSI and PA improvement. We chose the latter as a conservative estimate for the function parameters.

3.5.2 Comparative Results HAND prior

In the following, we describe in detail the performance of this selected parameterization. From Figure 3.4, it can be observed that the overall performance in all test sites, except the Suriname test site, has significantly improved CSI and PA at the expense of a slight decrease in UA.

Interestingly, the study sites that showed the significant improvement in CSI are areas with rolling terrain (Scotland) and low-lying wetland areas (New South Wales, Australia). Improvements are small for urban terrain (Valencia, Spain) and relatively flat areas. This result may be related to the limitation of HAND as a model for relatively flat areas [36], which in turn is often traced to the discrepancies of the source DEM in these areas [33].

The following sections show confusion maps with water masks overlain for reference [130]. We look at the details of the confusion maps of both HAND prior cases and non-informed prior cases to better understand the summarized findings.

3.5.2.1 Spain

The flood extent from Valencia, Spain, seen in Figure 3.5 primarily affected the river Turia and the adjacent green areas. The flooded area visible in the SAR flood maps is centered

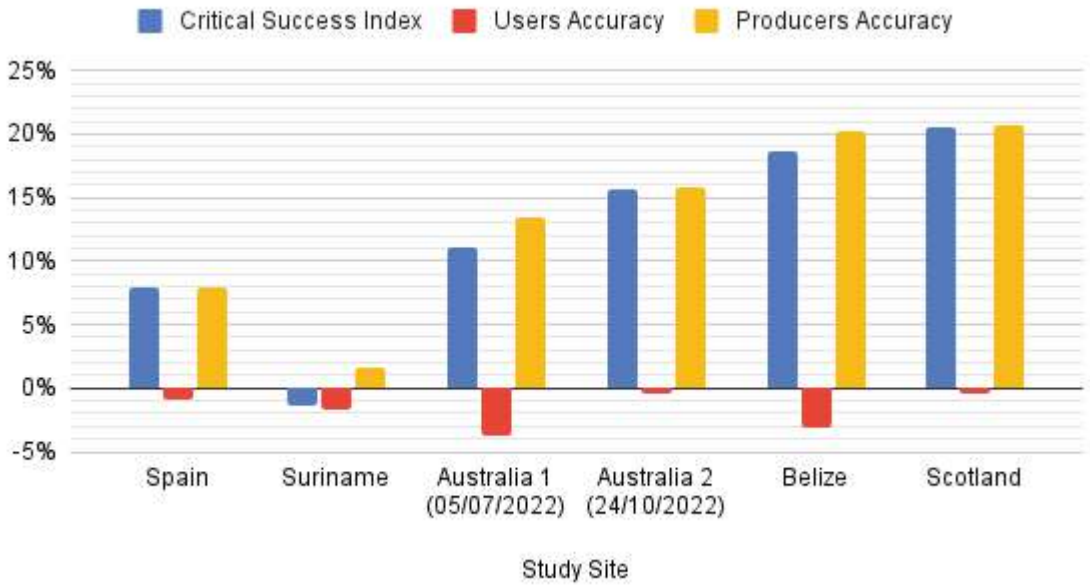

Fig. 3.4: Differences between the comparative metrics. HAND prior case minus non-informed prior case.

on its artificial channel. The channel is dotted with varying densities of vegetation. Dense foliage act as a volume scatterer and block the impinging signal from reaching the water surface. Thus sections of the flood along the channel are not visible in the SAR flood maps.

False negatives along the edges of the channel (red arrows) are the most pronounced issue for the flood maps generated, which results in very low CSI and UA. The channel is characterized by the relatively steep embankment, acting as a transition area, resulting in a complex scattering mechanism where the decrease in backscatter is not as pronounced.

The wider flood extent is better identified by the HAND prior case (b) than the non-informed prior case (a), causing the improvement in PA and CSI. For the most part, the HAND data reflects the low elevations of the channel. However, the resolution of the HAND data (e) is too coarse to cope with the misclassified pixels at the edges. The reference data and flood maps also miss the dense vegetation in the channel (yellow arrows); in this case, even with the highest possible prior probability of being flooded, it is not enough to overturn the non-flood result.

3.5.2.2 Suriname and Belize

The result for the Suriname test site is shown on the top row of Figure 3.6; the area is near Grand Santi, French Guiana. The flood scene indicates overflow along the Marowijne River at the border of Suriname and French Guiana at several small locations. For this site, the HAND prior case does not seem to add value to the original method.

Only minor changes between the HAND prior case (a) and the non-informed prior case (b) were observed for this study site. Since the area is densely vegetated, the quality of the SRTM DEM to represent ground topography is in question [59, 91]. As observed,

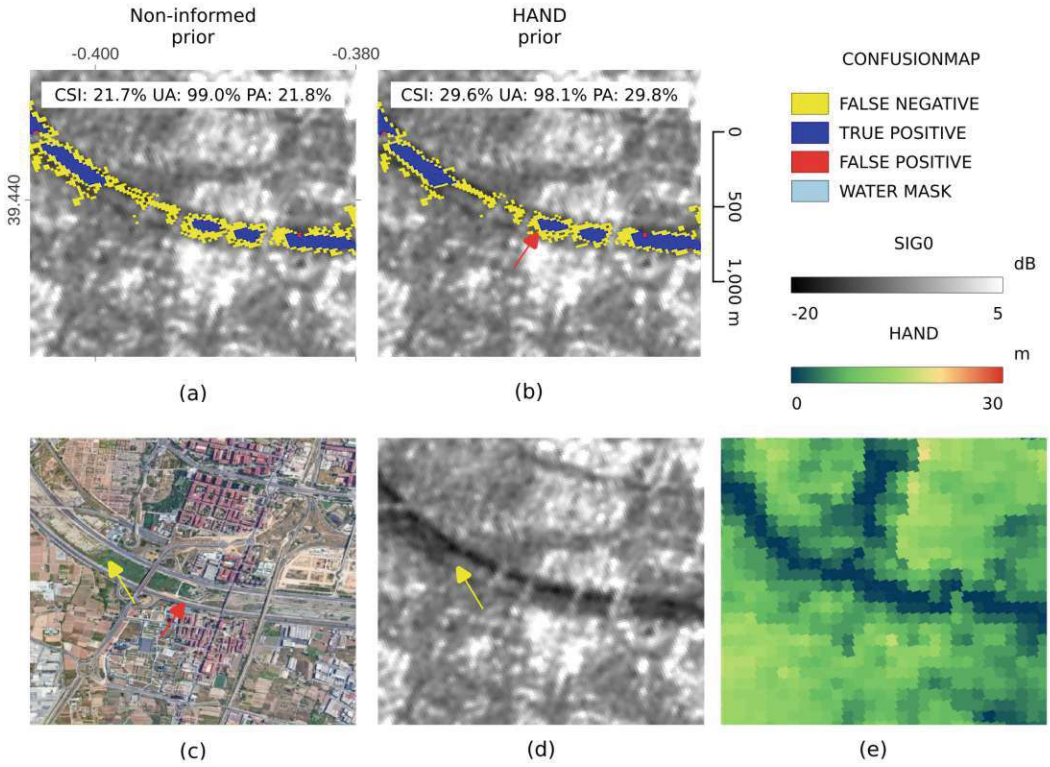

Fig. 3.5: Confusion map of a portion of the Spain study site. Top row: shows the confusion maps for non-informed prior case (a) and HAND prior case(b). Bottom row: True color Google satellite map (c), SIG0 backscatter intensity at VV polarization (d), and HAND index map(e)

most areas have relatively similar and relatively higher values HAND values (c) outside the drainage network compared to the other sites, possibly confirming the tree canopy height issue. Thus the method shows issues due to limitations of the input DEM affecting HAND prior case performance.

The bottom row of Figure 3.6 features the Belize study area focusing on an area west of Hattieville, Belize. Similar to the Suriname site, most of the area is covered by dense vegetation but with noticeable patches of sparsely vegetated areas. The confusion maps (e and f) show floods for low-lying clearings. Here possible flooded vegetation with less considerable decrease in backscatter intensity and flood edges are the most common source of false negatives in both prior case flood maps. Some of these areas are corrected in the HAND prior case (white arrows). False positives are observed in the HAND prior case not present in the non-informed prior (blue arrow) are pixels with higher backscatter values compared with surrounding flooded pixels.

3.5.2.3 Australia

Located in different parts of New South Wales, the 05/07/2022 (Australia 1) and 24/10/2022 (Australia 2) flood events share similar terrain characteristics. Both are located in low-lying areas littered with swamps, creeks, and streams. The 05/07/2022 (Australia 1) event

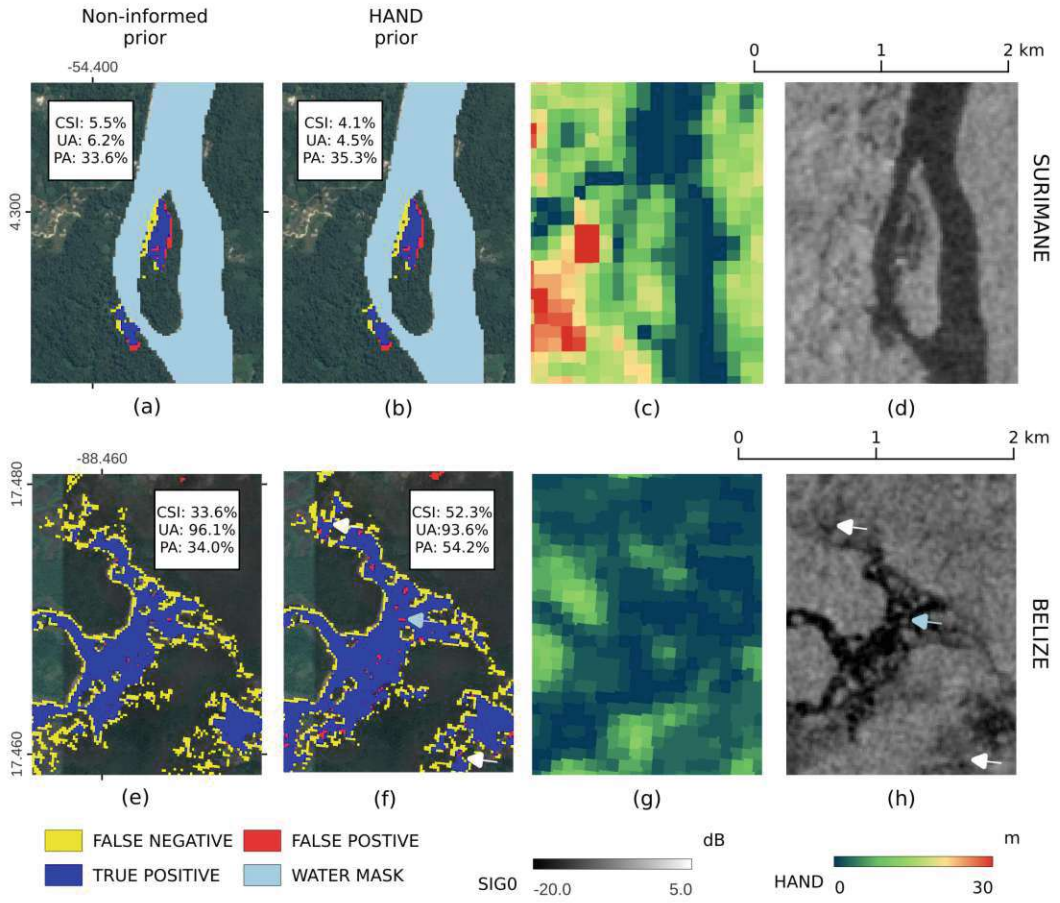

Fig. 3.6: Confusion map of a portion of the Suriname and Belize study sites. Top row: Confusion maps for the Suriname study site overlain on Google satellite map for non-informed prior case (a) and HAND prior case (b); HAND index map (c) and SIG0 backscatter intensity at VV polarization (d). Bottom row: Confusion maps for the Belize study site overlain on Google satellite map for non-informed case (e), and HAND prior prior case(f); HAND index map (g) and SIG0 backscatter intensity at VV polarization (h).

covered the swampy area north of Hunter River, while the 24/10/2022 (Australia 2) event occurred further inland near the town of Gunnedah and Namoi River.

Both events cover substantial areas, as seen in Figure 3.7. False negatives along the flood borders (or transition zones) are a common issue for both the HAND prior cases (b) and (f) as well as the non-informed prior cases (a) and (e). The HAND prior case showed superior performance in both flood events. Also worth noting are false positives (white arrows) that suggest this area is within the swampy region that is most likely flooded.

3.5.2.4 Scotland

The Scotland test case shown in Figure 3.8 shows false negative issues around the border areas (white arrows), and masking of dark SAR backscatter pixels at higher elevation (green arrow).

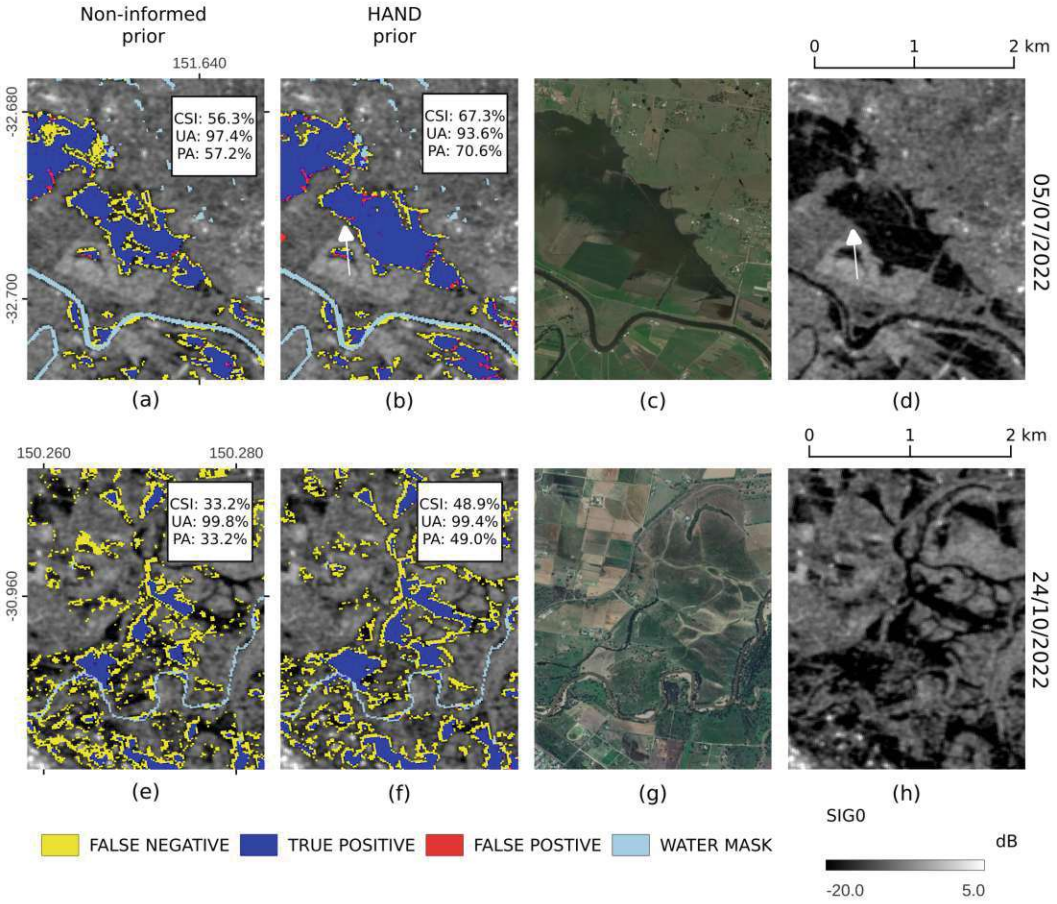

Fig. 3.7: Confusion map of a portion of the New South Wales, Australia study sites. Top row: Confusion maps for the 05/07/2022 (Australia 1) flood event overlain on SIG0 backscatter intensity at VV polarization for non-informed prior case (a), and HAND prior case(b); Google satellite map (c) and SIG0 backscatter intensity at VV polarization (d). Bottom row: Confusion maps for the 24/10/2022 (Australia 2) flood event overlain on SIG0 backscatter intensity at VV polarization for non-informed prior case (e), and HAND prior case(f); Google satellite map (g) and SIG0 backscatter intensity at VV polarization (h).

Similar to other test sites, improvements along the flood edges are visible from comparing the non-informed prior case (a) to the HAND prior case (b). As these edges or transition zones may contain mixed pixels [40] and complex scattering mechanisms [46] that causes lesser decrease in SAR (VV polarization) backscatter that the original algorithm [8] has issues with that the HAND priors rectifies. Lastly, low backscatter pixels masked by the HAND mask in the non-informed prior case (b) are labeled as non-flood in the HAND prior case (a).

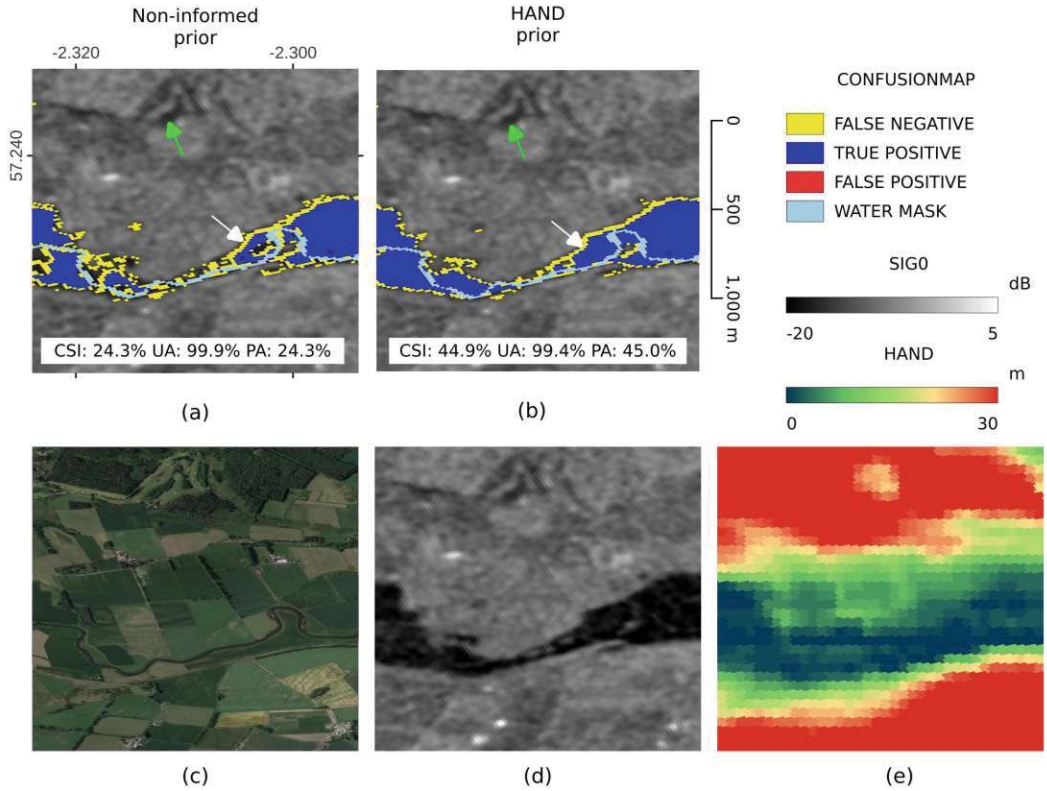

Fig. 3.8: Confusion map of a portion of the Scotland study site. Top row: shows the non-informed confusion maps for prior case (a) and HAND prior case(b). Bottom row: True color Google satellite map (c), SIG0 backscatter intensity at VV polarization (d), and HAND index map(e)

3.5.3 No-flood Conditions

Table 3.2 shows FPR calculated from the exemplary non-flooded images. The HAND column shows the FPR of flood maps using the HAND prior probability function, while the No Prior column shows the FPR of the maps with non-informed priors. It can be seen that the Valencia, Spain test site incurs both the largest FPR nominally for both cases and the most significant increase between the two. At the same time, minimal FPR was computed for Suriname. All study sites showed a small increase in FPR with the HAND-based prior all below 1%.

To qualitatively describe the performance of the HAND prior case versus the non-informed prior case in no flood scenarios, we present the case with the highest FPR (Spain study site) shown in Fig. 3.9. The zoomed in area shown is located east of the Alarcon reservoir. It can be observed that the false positives cover 1) reservoir areas that are not normally inundated (black arrows) and 2) low backscatter areas covering agricultural fields (white arrows). In the former, agricultural fields do not conform with the predicted seasonal backscatter response (see difference between panel d and b), leading to over-estimation– a known issue with the TU Wien algorithm [8]. At the same time, the latter is a similar case and a common issue in EO flood mapping. Both issues appear to be slightly exacerbated by the HAND prior.

Tab. 3.2: False Positive Rates for No Flood Cases.

Location	No Prior	HAND Prior	Difference
Spain	1.50%	2.43%	0.92%
Suriname	0.00%	0.00%	0.00%
Australia 1	0.03%	0.12%	0.09%
Australia 2	0.07%	0.66%	0.59%
Belize	0.04%	0.20%	0.16%
Scotland	0.14%	0.14%	0.00%
average	0.30%	0.59%	0.29%

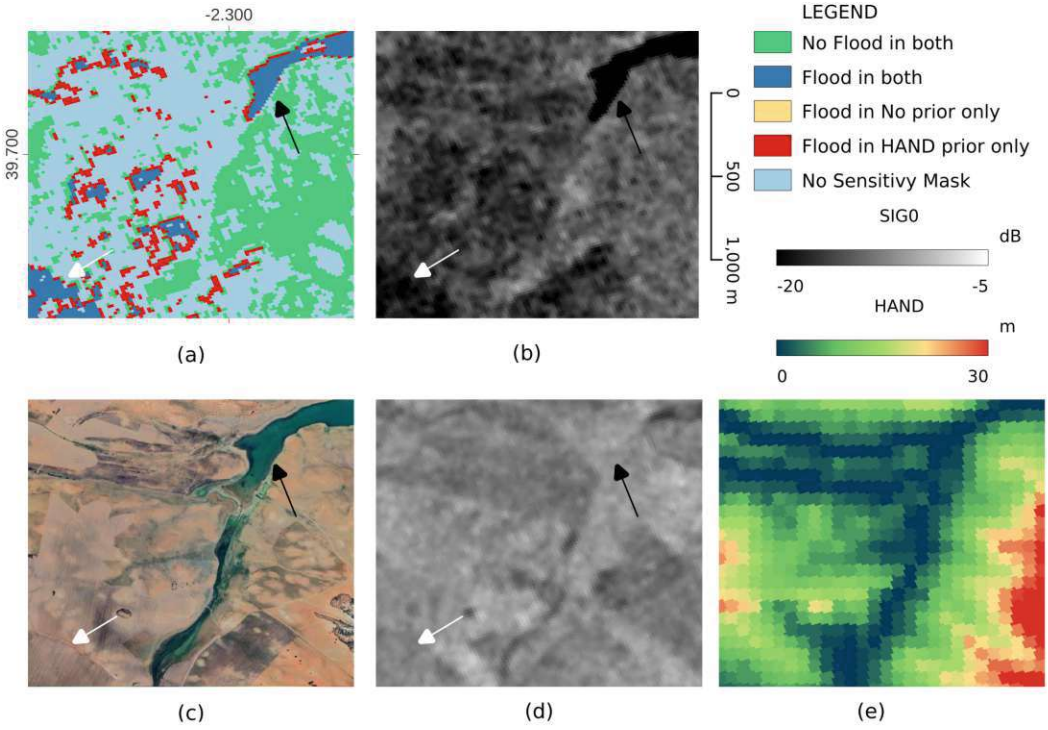

Fig. 3.9: Confusion map of a non-flooded scenario in a portion of the Spain study site. Top row: shows the difference map between the non-informed prior case and HAND prior case (a). SIG0 backscatter intensity at VV polarization on 2023-03-21 (b). Bottom row: True color Google satellite map (c), Day of year estimated SIG0 backscatter intensity at VV polarization from the harmonic model (d), and HAND index map (e)

3.6 Summary and Conclusions

Our results demonstrate a noticeable improvement to the TU Wien flood mapping algorithm by applying a HAND-based prior probability function compared to the baseline non-informed prior. We introduced an exponential function and estimated globally applicable

parameters to produce the HAND-based priors. We showed its performance on flooded and non-flooded cases in six study sites.

Concerning the the HAND prior probability function, we have not found an optimum for its parameters, as the observed improvement of CSI and PA comes at the cost of UA. Thus, it is prudent to select a conservative estimate for the HAND prior probability function parameters, which does not severely impact UA.

While empirically derived, the mid-point at 20m agrees with the assumption that this value should be within the usual range of HAND threshold values. On the other hand, lower steepness values proved to be useful, with 10m working well with the mid-points tested. Further parameter optimization could still improve flood mapping with HAND-based priors. However, given the close responses of the function to changes in parameters, we find the estimated parameters already suitable.

The HAND prior probability function introduced and tested here showed promising performance. Applying the HAND-based priors decreases false negatives at the expense of a slight increase in false positives. In this regard, we observed less improvement in relatively flat areas than areas with rolling terrain and low-lying areas. At the same time, we have observed instances of similar masking effects when using the HAND prior probability function, thus removing the dependence on HAND masking.

In terms of reducing false negatives, flooded areas with a lesser decrease in backscatter intensities benefit from the HAND prior probabilities. The most common observed occurrences of such areas are 1) floods in sparsely vegetated areas and 2) flood boundary or transition regions.

On the other hand, added false positive areas are typically found in low lying areas with minimal adverse effect of not masking at higher HAND values. Noting that the CEMS reference flood maps used were also delineated from the same Sentinel-1 images, we observed that some labeled false positives from the HAND prior test cases are most likely true positives that the CEMS rapid mapping method misclassified. On this point, we recommend further testing with independently sourced reference data.

For the no-flood scenarios, a slight increase in the false positive rates was observed for all six study sites tested. This test showed reasonable performance, with no more than a 1% increase in FPR rates. We observe that the HAND prior slightly exacerbates existing issues with deviations with the expected seasonal backscatter response. Nevertheless, it should be pointed out that no extreme events (very dry or wet conditions) were captured in the six sites tested. As certain extreme events result in low backscatter signals that lead to wholesale false positives, testing the performance of the HAND prior probabilities at such conditions is recommended.

To conclude, our flood mapping with HAND-based priors demonstrated improvements by decreasing false negatives at low HAND values and preventing false positives at high HAND values. The latter implies we removed the need for independent pre or post-processing HAND mask. However, the improved algorithm has drawbacks: a slight increase in false positive rates and noted limitations for densely vegetated areas. We showed the suitability of applying a single parameterization to the six test sites, suggesting feasible application of such priors to the TU Wien flood mapping algorithm at a global scale. With its simple formulation and ubiquitous input, this *prior* formulation could potentially benefit other Bayesian or probabilistic flood mapping workflows.

3.7 Acknowledgements

The computational results presented have been achieved using inter alia the Vienna Scientific Cluster (VSC). The authors acknowledge the contributions of Iftikhar Ali for his contributions in processing the HAND dataset. We would further like to thank our colleagues at TU Wien and EODC for supporting us on technical tasks on maintaining the datacube.

3.7.1 Funding

This research work was performed with support of the Engineering Research and Development for Technology Program of the Philippine Department of Science and Technology, the project "S1Floods.AT" (Grant no. BW000028378) founded by the Austrian Rsearch Promotion Agency (FFG) and the project “Provision of an Automated, Global, Satellite-based Flood Monitoring Product for the Copernicus Emergency Management Service” (GFM), Contract No. 939866-IPR-2020 for the European Commission’s Joint Research Centre (EC-JRC). The authors acknowledge TU Wien Bibliothek for financial support through its Open Access Funding by TU Wien.

3.7.2 Data Availability

The data presented in this study is openly available at:
`https://doi.org/10.48436/vtfkq-snz36`

Chapter 4

Assessment of Time-Series-Derived No-Flood References for SAR-based Bayesian Flood Mapping

This chapter is a reformatted accepted version of:
Tupas, M. E., Roth, F., Bauer-Marschallinger, B., & Wagner, W. (2024). Assessment of Time-Series-Derived No-Flood References for SAR-based Bayesian Flood Mapping. GIScience & Remote Sensing, 61(1), 2427304. `https://doi.org/10.1080/15481603.2024.2427304`
The original document will be openly accessible at: `https://doi.org/10.1080/15481603.2024.2427304` under the Creative Commons Attribution (CC-BY) license.

4.1 Abstract

The systematic mapping of flood events with Synthetic Aperture Radar (SAR) data is an area of growing importance. One global flood mapping algorithm utilized within the Copernicus Emergency Management Service is based upon a Bayesian Inference model that compares a SAR image to a simulated reference image representing no-flood conditions. This no-flood reference image is at present generated using a harmonic model trained using historic time series, thereby producing a backscatter image representing mean seasonal conditions. One known weakness of this approach is that it cannot account for changing environmental conditions from year to year, potentially causing an overestimation of flood extent during dry periods, snow and frost, or other effects causing lower-than normal backscatter. To minimize this detrimental effect, we introduce an exponential filter to estimate the no-flood reference image by weighting the most recent backscatter observations according to their time difference to the current SAR acquisition. We compare the performance of the new exponential filter model against the harmonic model using a novel time-series flood mapping assessment approach. First, we assess their predictions against the actual SAR image time series for the year 2023. Then, we analyze the false positive rate of the corresponding flood maps generated to ensure the robustness of the automated algorithm outside of flood events. Furthermore, we perform qualitative and quantitative analyses of flood maps matching with semi-automatic results from Copernicus Emergency Management Services and Sentinel Asia as a reference. Our time-series analysis confirms increased false positive rates due to well known environmental drivers and highlights issues with agricultural overestimation. In this regard, the time-series comparisons of the no-flood reference models show a clear improvement in the TU Wien algorithm with the exponential filter, effectively reducing false positive rates on non-flooded scenes in most study sites. The exponential filter performed better than the harmonic model in most flooded scenes, where sites show generally improved Critical Success Index and User's accuracy. However, the exponential filter model has difficulties with sites with prolonged floods in the time series, requiring further development. Overall, the exponential filter no-flood reference model shows great promise for improved global near-real-time flood mapping.

Keywords: Flood Mapping; Synthetic Aperture Radar; Sentinel-1; Bayes Theorem; Harmonic Model; Exponential Filter

4.2 Introduction

Floods are among the most frequent natural disasters affecting an increasing segment of the global population [13, 110]. A recent estimate suggests that 1.81 billion people, or almost one in four persons are directly exposed to severe flooding [96]. Using remote sensing for large-scale mapping of flood situations is invaluable for emergency response, recovery, and reconstruction. Supporting these applications, Synthetic Aperture Radar (SAR) based flood mapping is gaining prominence for systematic global operations due to its spatio-temporal coverage and independence from weather and ligthining conditions [98, 102, 109].

SAR-based flood mapping techniques that have proven effective include single-image thresholding algorithms [39, 71], parametric or tile-based thresholding schemes [15, 72, 120, 141], and machine learning methods [53, 105, 132]. However, due to floods' transient and anomalous nature, most approaches employ some form of change detection. Therefore, these algorithms highly depend on appropriate pre-flood baselines or no-flood references. Careful selection of such images is a crucial – often manual – task in algorithms using single pre-flood images [4, 123]. These selection procedures are challenging for systematic flood mapping operations. As such, the automated selection of these no-flood references from time series stacks has attracted attention in the literature [47, 60, 141].

Instead of selection algorithms, which often face problems in Near-real-time (NRT) operations, synthetic no-flood references can be produced from time-series analysis. Common methods include using mean or median values [18, 24, 80], or employing harmonic models with seasonally adjusted day-of-year estimates [101]. These synthetic references have the advantage of speckle suppression [117] and ease of automation. However, while having an essential impact on mapping performance, model selection and parameterization of these underlying models (e.g., the period length of time-series analysis) are difficult to generalize in the context of global application.

SAR change detection algorithms, where these no-flood references are used, may involve differencing or index-based methods [101], time-series anomaly detection, to no-flood probability functions in Bayesian methods [100]. An example of the latter is the flood mapping algorithm developed at Technische Universität Wien (TU Wien), which employs a pixel-based Bayesian decision between flooded references from historical samples versus a non-food reference based on a predefined harmonic model [8]. The algorithm is currently deployed in an operational setup under the Copernicus' Global Flood Monitoring service[98]. It has performed well in areas with well-defined seasonality but shows higher uncertainties for areas with ill-fitting temporal patterns, leading to overestimation.

Time-series derived estimates deviating from the actual SAR measurements can result from non-conformity with predefined parametric functions, leading to the proposal of non-parametric approaches [19, 93]. Balancing algorithm robustness and computational complexity is crucial. Rolling filters may provide an alternative. One such filter – the exponential filter – weighted filter, has been effectively used for improving soil moisture monitoring [126]. Unlike other filters, it features a near-real-time iterative formulation [3, 9] that makes it enticing for systematic mapping operations. Here, we test its use for improving flood mapping for the first time.

Most flood algorithms are tuned and tested for specific events, while mapping performance on non-flooded scenes is often ignored. This optimization of algorithms for flood scenes may disregard possible overestimation and false flagging of images as flooded where there is none. In this contribution, we present a novel time-series flood mapping assessment approach to the TU Wien algorithm to compare time-series derived no-flood references. We analyze and compare the original harmonic model with a proposed exponential-filter model. In seven study sites, we assess both non-flooded and flooded scenarios. First, we assess the no-flood models' backscatter estimates against the actual SAR image time series for 2023. Then, we analyze the false positive rate of the corresponding flood maps generated. Qualitative and quantitative analyses of flood maps are conducted using rapid mapping

activations from Copernicus Emergency Management Services (CEMS) and Sentinel Asia as references.

4.3 TU Wien Flood Mapping Algorithm

We present the TU Wien flood mapping algorithm's theoretical foundation and the no-flood references we intend to examine.

A Bayesian classifier, the TU Wien algorithm uses a pixel-based rule in labeling floods dependent on the posterior probability $p(F|\sigma^0)$ surpassing a predefined threshold (e.g., 50%). The posterior probability from Bayes' inference from different authors (e.g.Bauer-Marschallinger et al., Giustarini et al., Refice et al., Schlaffer et al., Westerhoff et al.) is computed using Equation 4.1:

$$p(F|\sigma^0) = \frac{p(\sigma^0|F)p(F)}{p(\sigma^0|F)p(F) + p(\sigma^0|N)p(N)} \tag{4.1}$$

where the conditional probability, $p(\sigma^0|N)$, to be non-flooded, is computed using the pixel's incoming backscatter against a probability distribution defined by the expected no-flood backscatter value and its temporal standard deviation (defined by the no-flood references presented in Section 4.3.1 and 4.3.2). $p(\sigma^0|F)$ for the flooded case is computed against the incidence angle-dependent water distribution derived from historical samples. Lastly, $p(F)$ and $p(N)$ are the prior probabilities of a pixel being flooded and non-flooded, respectively. Non-informed priors [34] were used for both.

4.3.1 Harmonic Model

The current approach of the TU Wien algorithm defines the no-flood backscatter probability distribution using the harmonic model. This model (shown in eq. 4.2) provides a practical way to estimate backscatter using the sum of harmonic (sinusoidal) terms to characterize its behavior over time. The presented algorithm builds upon the formulation of Schlaffer et al., where the trend is neglected and applies three iterations of harmonic terms, i.e., $k = 3$. With this realization, the model fluctuates in the order of months. Therefore, short-term backscatter variations, such as those caused by flooding, are smoothed, making it a notable no-flood reference.

$$\hat{\sigma}^0(t_n) = \overline{\sigma^0} + \sum_{i=1}^{k} \left\{ c_i \cos \frac{2\pi i t_n}{365} + s_i \sin \frac{2\pi i t_n}{365} \right\} \tag{4.2}$$

Here, $\hat{\sigma}^0$ is the expected Sentinel-1 backscatter at day-of-year (DOY) t_n and is estimated based on c_i and s_i representing the harmonic parameters. The first cosine coefficient is $\overline{\sigma^0}$, equivalent to the mean Sentinel-1 backscatter for the time series.

The harmonic parameters used for this model were precalculated using a linear least squares estimation [115] using an input time series of three years. These are the same parameters currently used for Global Flood Monitoring (GFM) operations. This three-year formulation performs overall better than the original two-year parameters [74].

The computational complexity of the harmonic model does not allow regular updating and is best pre-computed to meet operational demands [115]. This limitation leads to issues for areas with abrupt land cover change or areas deviating from the modeled seasonal trend. The latter is typically observed in bare soil, grasslands, and agricultural areas, which are more prone to backscatter fluctuations induced by vegetation and soil moisture dynamics [124]. This leads to no-flood probability distributions inaccurately reflecting the actual vegetation and soil moisture states that can lean towards flood labeling resulting in overestimation [8].

4.3.2 Exponential Filter Model

To compensate for such overestimation, we seek alternative methods that could be updated dynamically, allowing a more accurate and up-to-date representation of vegetation or soil moisture dynamics. Consequently, we considered shorter moving averages or rolling filters. One such filter applies exponential weights decaying through time. We present the continuous formulation of the exponential filter model in equation 4.3 taken from Wagner et al. but adopted to estimate backscatter, $\widehat{\sigma}^0$, at some day in time: t_n.

$$\widehat{\sigma}^0(t_n) = \frac{\sum_i^n \sigma^0(t_i) e^{-\frac{t_n - t_i}{T}}}{\sum_i^n e^{-\frac{t_n - t_i}{T}}} \tag{4.3}$$

where $\sigma^0(t_i)$ is the observed Sentinel-1 backscatter at time t_i. T is the equations' characteristic time length parameter, representing the timescale of backscatter variation in days.

Preliminary tests with other rolling filters (like mean and median) showed similar or slightly worse performance than exponential filters and is presented in the Supplementary material (Section 4.10.4) for brevity. Nonetheless, the practical prospect of the exponential filter lies in its recursive formulation [9]. While mathematically giving the same result, the recursive formulation allows updated estimates to be calculated at new time steps with only incrementally updated gain value and new measurements, dramatically reducing computational requirements compared other rolling filters where a recursive formulation is not feasible. However, to better illustrate the effect of T parameter and our current focus on performance rather than efficiency, we only present the continuous form in this work.

To reduce the volume of datasets used in the continuous formulation, we excluded measurements with effective weights of less than 0.05. This procedure roughly corresponds to considering measurements within the time range of $[t_n - 3T, t_n)$ (excluding t_n).

In soil moisture studies, the selection of T value is topic of ongoing investigation [3, 88], where Paulik et al. established basic relations of T values to soil depth from correlation analysis against in-situ reference measurements. As the optimal value of T in flood mapping is still unknown, we aim to determine a suitable T parameter for robust flood mapping by experimenting with different values. We test multiple T, i.e., T = 10, 20, 30, 40, 60, 90, and 120.

From preliminary tests, we found that exponential filter estimates with shorter time-series inputs do not suppress speckle well. Therefore, input radar backscatter images for exponential filter were de-speckled using Lee-Sigma Filter[57, 58] with 3x3 kernel size.

4.3.3 Standard Deviation

To form the no-flood backscatter probability distribution, we assume its form as Gaussian based on suggestions from the literature [94, 100, 106]. Thus, in addition to an expectation value, a degree of dispersion (standard deviation) is required.

We compute the standard deviation using Equation 4.4 based on Bauer-Marschallinger et al.'s approach, given by the square root of the time-independent sum of squared errors, $SSE(\sigma^0)$, between the actual backscatter time-series and the estimated values from the time-series models, divided by the models' degrees of freedom ν.

$$std = \sqrt{\frac{SSE(\sigma^0)}{\nu}} \quad [\text{dB}] \tag{4.4}$$

Here ν is the degrees of freedom and is solved by $n - (2k + 1)$ for the harmonic model and $n - 2$ for the exponential filter model, where n is the number of observations. For the harmonic model, the standard deviations were computed from the same three-year period used to estimate the parameters. In contrast, the exponential filter standard deviations, regardless of T values, were computed using the 2023 time series.

4.3.4 No-Sensitivity Masking and Post-processing

After inital labelling, the TU Wien algorithm applies a no-sensitivity masking procedure that tags pixels where the BI is not feasible. This includes areas with 1) extreme local incidence angle where the flood probability model is invalid, 2) conflicting flood and no-flood probability distributions, and 3) measurement outliers. We refer the reader to Bauer-Marschallinger et al. for further details on no-sensitivity masking. This study uses the same no-sensitivity mask thresholds as the original algorithm.

Finally, we omit the majority filter-based post-processing step, as we found that it results in undesired over- and under-labeling. Further exclusion masking (e.g., HAND mask, and radar shadow masks) [140] were not applied to allow for comparisons and observe possible improvements in these areas.

4.4 Materials and Study Sites

To give an overview of the materials and methods used in this study, Figure 4.1 shows the different phases of analysis. The green panel explains derivation from the Sentinel-1 data cube (Section 4.4.1) of the TU Wien algorithm and the no-flood reference models, we described in described in Section 4.3. To ensure a globally applicable analysis, we endeavor to analyze as many sites as possible. The purple panel represents the site selection process discussed in Section 4.4.4. We further ensure robustness in no-flood scenarios by extending our analysis to understand temporal behaviors. The yellow panel shows the no-flood time series analysis found in Section 4.5.1. Finally, we conduct traditional comparisons for a reference flood event for each test site. The orange panel represents the flood mapping accuracy assessment described in Section 4.5.2.

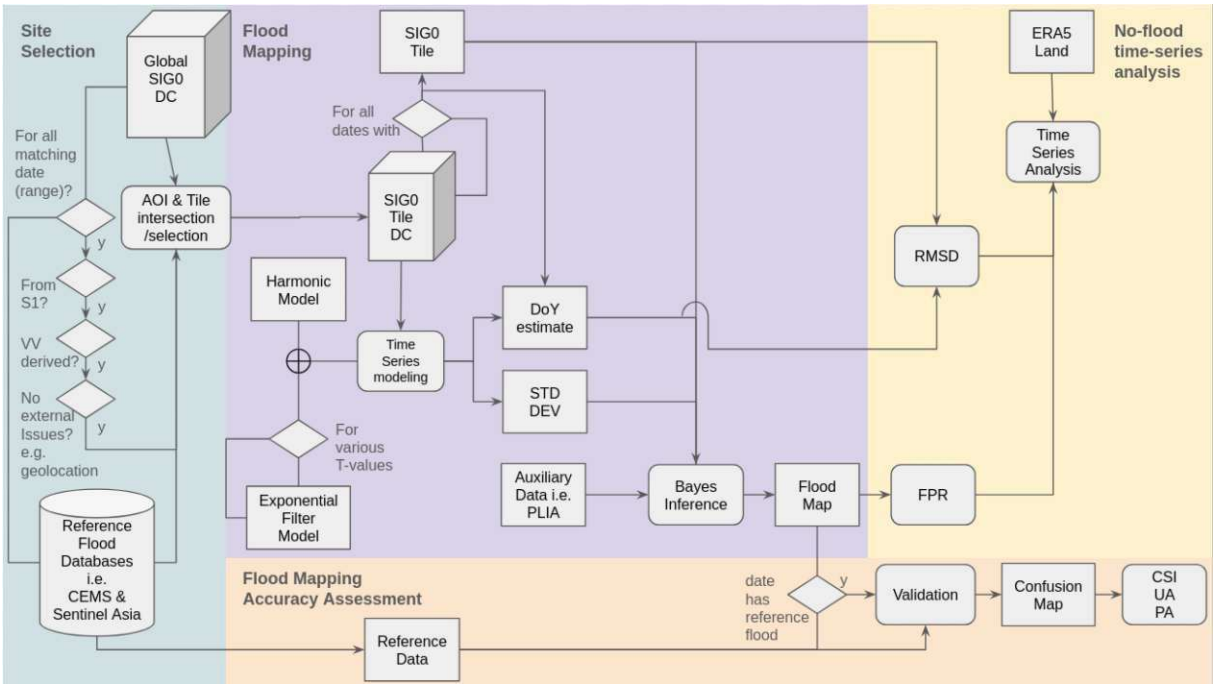

Fig. 4.1: Methodological Flowchart and Phases of Analysis. Green panel: Site selection procedure. Purple panel: Flood mapping algorithm. Yellow panel: No-flood time-series analysis. Orange panel: Flood mapping accuracy assessment.

4.4.1 Sentinel-1 Data cube

To produce the flood maps and their corresponding no-flood reference images analyzed in this study we use the VV polarized subset of Sentinel-1 [113] data cube maintained by TU Wien and EODC [125]. The data cube comprises curated Sentinel-1 Ground Range Detected (GRD) image tiles with 20 m × 20 m pixel size and organized using the T3 tiling level (300 km x 300 km extents) of the Equi7Grid system [10]. Spatial analysis performed throughout this study were conducted in the same tiling and grid system using the python based Yeoda software stack `https://github.com/TUW-GEO/yeoda` (accessed July 20, 2024).

4.4.2 Ancillary Data

To understand the environmental conditions and spatio-temporal backscatter dynamics governing our flood mapping results, we cross-referenced several ancillary datasets that were re-gridded and reprojected to the Equi7Grid tiles.

Soil temperature and water content are crucial factors in explaining overestimation [65], and were used to rule out floods in images in which frozen and dry soils cause large swaths of low backscatter. ERA5-Land [78] Daily Aggregated data accessed from Google Earth Engine [37] were used to calculate the means of soil temperature and volumetric soil water at the topmost level (0–7 cm).

Furthermore, we used the ESA WorldCover (2021) [135] to explain spatial patterns. And, where available, EU Crop Map (2022) [22] for finer separation of crop types. Land

cover and crop type (and their associated cropping practices) give further insights into the flood maps and overestimation patterns.

4.4.3 Reference Flood and Water Maps

We use activation-based flood maps as a reference for accuracy assessments under the premise that operational service relies on expert intervention in (semi-automated) map generation and quality assurance. These maps are reasonable alternatives in lieu of actual ground truth flood data.

In this regard, Copernicus Emergency Management Services (CEMS) [50] rapid mapping vector flood extents and associated ancillary data (e.g., AOI, Hydrology) were retrieved from `https://emergency.copernicus.eu/` (accessed on 13 March 2024). Sentinel Asia [51] vector flood extents were also downloaded from `https://sentinel-asia.org/EO/EmergencyObservation.html` (accessed on 13 March 2024). The reference flood maps were rasterized and reprojected to the Equi7Grid tiles.

To differentiate semi-permanent and permanent water bodies from flood results [130], we use the CEMS hydrology dataset for the assessed flooded AOIs. For comparisons of entire tiles and where CEMS data is absent, we use Copernicus DEM [28] Water Body mask. Both datasets are used to mask out water areas for both qualitative and quantitative assessments.

4.4.4 Study sites

All flood mapping activations listed in the CEMS and Sentinel Asia databases from March 2023 to November 2023 were considered in our study. The aim is to analyze a diverse representation of environmental and climatic conditions, allowing for global generalization. However, emergency response maps as reference data require careful inspection, selection, and contextualization to obtain nuanced assessments. Thus, we implement a rigorous matching and screening procedure.

A preliminary search of the two flood mapping services' activations was screened for flood maps delineated using Sentinel-1. This was done to ensure that our experimental results and the reference match temporally and spatially. The reference flood maps and corresponding Sentinel-1 images were scrutinized to ensure that there were no obvious geolocation errors and that flood extents could be reasonably determined from VV polarized data –for which the algorithm is tuned for. In cases with more than one area of interest (AOI), we selected the AOI with the most prominent flood coverage. The final area of interest for flooded assessments is selected based on the intersection of the Equi7Grid tile that contains the most significant portion of the AOIs. In contrast, the whole data cube tiles are used for non-flooded assessments.

Four test sites covered by CEMS are situated in Europe, where there is a noted increase in flood anomalies [108]. The flooding incidents in Scotland [38], Slovenia [11] and Greece were triggered by extreme precipitation, the latter noted for its exceptional rainfall duration and intensity [25, 44]. Meanwhile, CEMS reports that the snow melt contributed to the flood event in Latvia. The Sentinel Asia activations describe the events in Vietnam and India as caused by heavy rainfall, while tropical cyclone Doksuri caused the Philippine

Location	Rel. Orbit	Source	Activation Code	AOI/Subset	Est. Area(km^2)	Date	GEnS zone[a]
Scotland	A030	CEMS	EMSR698	03	20	2023.10.08	E, J
Vietnam	D091	Sentinel Asia	FL-2023-000179-VNM	Nghe An & Ha Tinh	286	2023.09.30	M, R
Greece	A102	CEMS	EMSR692	01	730	2023.09.07	K, L
Slovenia	A146	CEMS	EMSR680	04	3	2023.08.05	G, J
Philippines	D032	Sentinel Asia	TC-2023-000121-PHL	–	416	2023.07.28	R
India	A027	Sentinel Asia	FL-2023-000112-IND	–	537	2023.07.16	M, P
Latvia	D080	CEMS	EMSR657	01	55	2023.04.03	G

Tab. 4.1: Study Sites and Metadata on Equi7grid Tile Details, Reference Flood Maps and Climate Zones.

[a]Global environmental stratification (GEnS) zones: E-cold and wet, G-cold and mesic, J-cool temperate and moist, K-warm temperate and mesic, L-warm temperate and xeric, M-hot and mesic, P extremely hot and arid, R extremely hot and moist

mapped event. The area was subjected to intense rainfall from a preceding tropical depression [43].

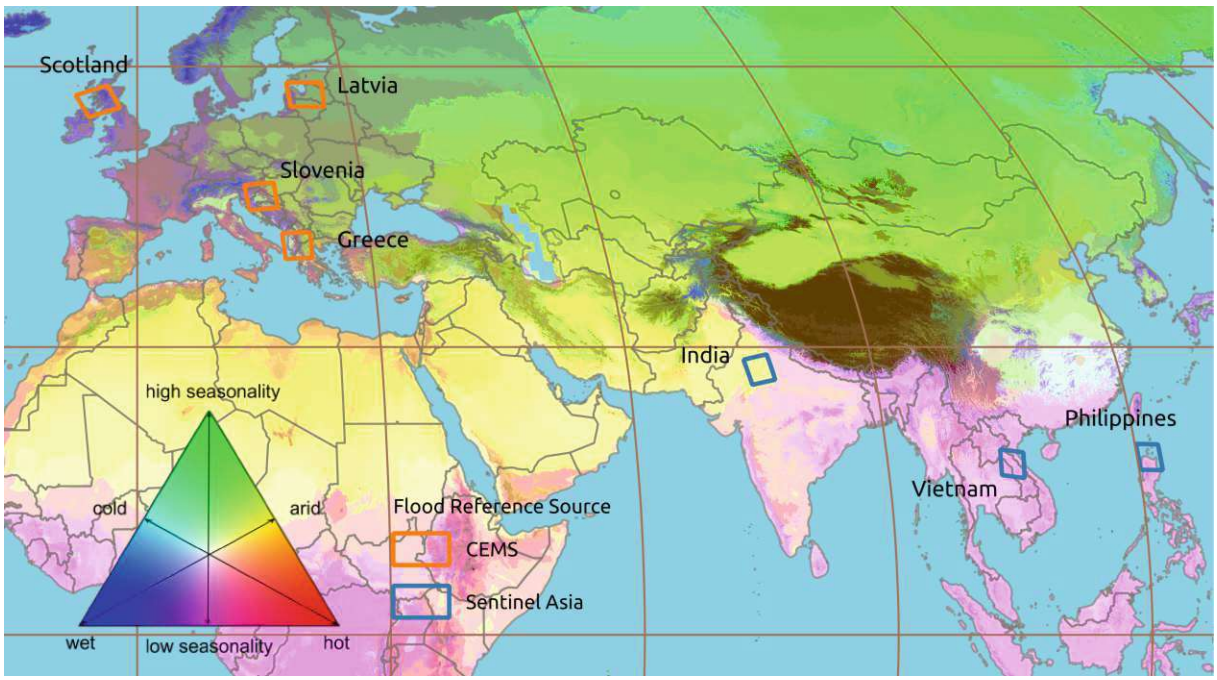

Fig. 4.2: Location of study sites (Equi7Grid Tiles) colored based on available reference flood maps overlain on global environmental stratification (GEnS) layer [76].

When plotted against global environmental stratification data [76], shown in Figure 4.2, one can see that our test sites contain a good mix of climate types and different seasonality inclinations. Metadata summary on the seven study sites is found in Table 4.1; these include the reference flood activation information, and the dominant Global environmental stratification (GEnS) zones per tile.

4.5 Assessment Methodology

4.5.1 Reference Image and No-Flood Time-Series Assessment

To compare the performance of the no-flood time series backscatter models (and T parameterization), we compute the root-mean-square deviation (RMSD) [6] between the estimates and actual Sentinel-1 measurements per image acquisition date for 2023. RMSD is computed using Equation 4.5:

$$RMSD(t_n) = \sqrt{\frac{\sum_{i=0}^{N-1}(\sigma_i^0(t_n) - \widehat{\sigma}_i^0(t_n))^2}{N}} \quad [\text{dB}] \tag{4.5}$$

where $\widehat{\sigma}^0(t_n)$ is the estimated Sentinel-1 backscatter per pixel for a given time tn, while $\sigma^0(t_n)$ is the observed Sentinel-1 backscatter for that pixel at the same time and N is the total number of valid pixels.

Flood maps are then produced for every Sentinel-1 acquisition date irrespective of flood occurrence. We create maps based on each no-flood reference for each date using the harmonic model and the exponential filter at varying T values.

We limit our assessments to one relative orbit per tile, which is selected to match the flooded reference maps' source Sentinel-1 image's relative orbit. At a specified relative orbit, with a 12-day revisit time, there are about 30 acquisition days per study site for a year. This mapping during each satellite pass simulates the automated procedure performed in the flood monitoring operations. Up to 240 flood maps for 2023 were created for each study site. We note actual flooded acquisition dates for each tile based on documented reports and flood mapping service activations, while all other acquisitions are assumed to be entirely non-flooded.

$$FPR = \frac{FP}{FP + TN} \tag{4.6}$$

After masking permanent and seasonal water, we can compute the false positive rate (FPR) using equation 4.6 based on the assumption that all remaining flooded pixels are false positives (FP) and non-flooded as true negatives (TN) [6, 119]. The FPR and RMSD are temporally plotted and cross-referenced with ERA5-Land data for soil temperature and volumetric soil water for the uppermost soil layer. We do this to explore possible overestimation through time and attribute its possible causes vis-a-vis the no-flood model used for flood mapping. To confirm the difference in performance of the tested no-flood models, we perform pairwise comparisons between all models. For each two no-flood model comparison, we employ paired statistical tests between the aggregated FPR differences from all study sites.

4.5.2 Flood Map Assessment

In addition to the no-flood evaluations, we analyze the performance of our algorithm on dates where reference flood maps are present, described in Table 4.1. Before quantitative assessments, we harmonize our generated flood map with the reference data. First, the maps are clipped to reference data AOIs. These are provided as a separate vector layer for

CEMS results, while the bounding box of the Sentinel Asia vector results is used as AOIs. Then, we apply the corresponding water masks before creating confusion maps and tables.

Subsequently, we compute accuracy assessment metrics for all flood maps. The metrics, Critical Success Index (CSI), User's Accuracy (UA), and Producer's Accuracy (PA), shown in the equations 4.7, 4.8 and 4.9 below:

$$CSI = \frac{TP}{(TP + FP + FN)} \tag{4.7}$$

$$UA = \frac{TP}{(TP + FP)} \tag{4.8}$$

$$PA = \frac{TP}{(TP + FN)} \tag{4.9}$$

where TP is the true positive, TN is the true negative, FP is the false positive, and FN is the false negative counts derived from the binary confusion matrix. These metrics are chosen to express the flooded maps' overall performance via the CSI [56], while over- and underestimations from UA and PA [6]. To compute these accuracy assessment metrics for the flood maps against the vector reference data, we use ABCRaster `https://github.com/TUW-GEO/ABCRaster` (accessed June 20, 2024) to automate the procedure. Relying solely on a few metrics may not fully capture mapping performance. Therefore, we conduct a qualitative visual evaluation of the confusion maps.

4.6 Results

4.6.1 No-flood Time Series

The plotted RMSD and FPR against ERA5-Land surface soil temperature and moisture shown in Figures 4.3, 4.4, and 4.5, are sample plots for the Latvia, Greece, and India study sites, respectively. We include the time-series plots for the rest of the sites in the Supplementary material for conciseness.

The figures present three horizontal panels depicting the performance of the no-flood references using the harmonic and exponential filter models at various T values and soil properties per Sentinel-1 acquisition per tile in a specific relative orbit. The top panel shows the FPRs per flood map for every Sentinel-1 acquisition date for the tile, assuming there is no actual flood. The middle panel shows the RMSDs for no-flood reference estimates versus the actual Sentinel-1 data. The bottom panel shows the ERA5-Land temperature and volumetric water content at the topmost soil layer (0–7 cm).

4.6.1.1 Latvia

We present the result for the Latvia test site (Figure 4.3)as a representative study site with a cool temperate climate. Similar phenomena can be observed with the Slovenia and Scotland study sites (in the Supplementary material).

Regarding FPRs, we observed peaks at the beginning and end of the year corresponding to frozen soils at those specific dates. As frozen soils exhibit a similar significant drop in

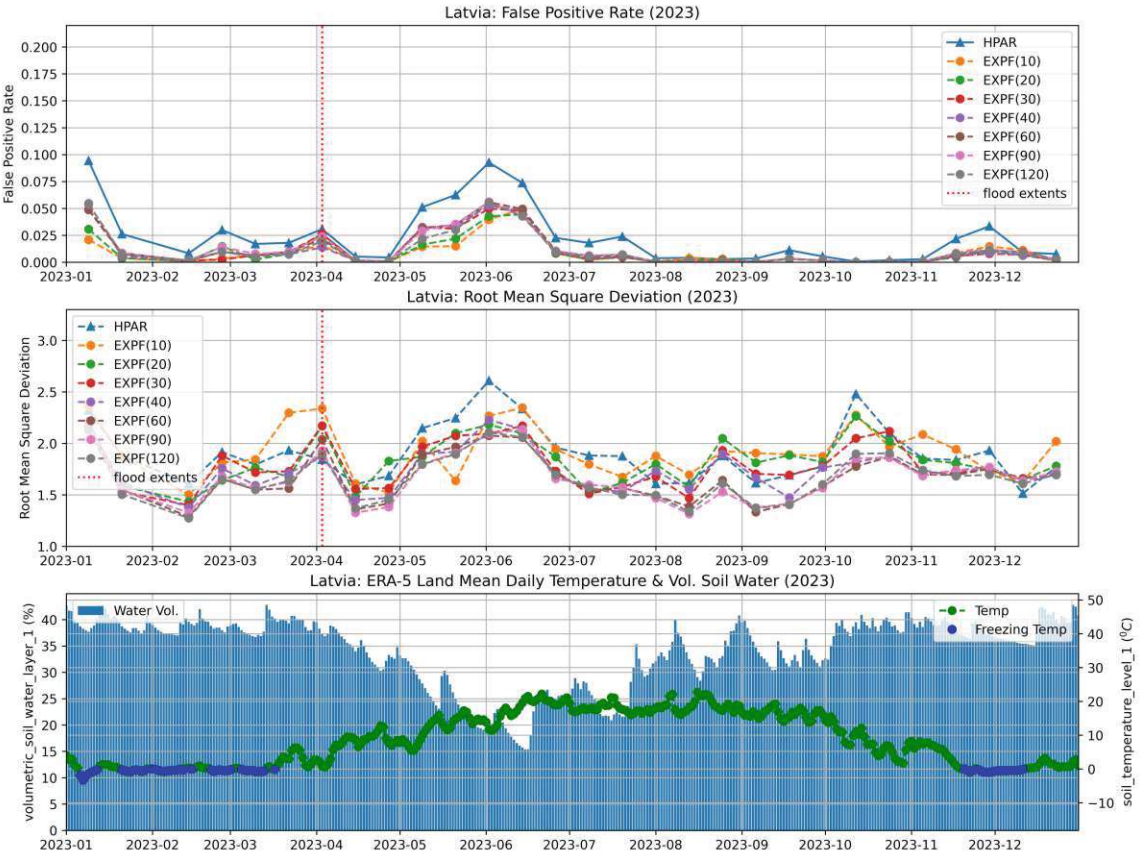

Fig. 4.3: Temporal Plots of False Positive Rate, Root Mean Square Deviation, and ERA5-Land Soil Temperature and Volumetric Soil Water for the Latvia Study Site

backscatter [5] thus is easily mistaken as floods. A smaller peak in FPR was observed during the flooding event in April. A prolonged peak is observed towards the summer months, corresponding to relatively dry soils from the ERA5-Land data. This rise in false positives relates to lower backscatter signals of drier soils being mistaken for the low backscatter caused by specular reflection of inundated areas as radar backscatter increases with soil moisture content [122] except for arid environments where subsurface scatterers are present [127]. The scattering behavior of wet soil changes fundamentally once standing water forms at the surface. The peaks in RMSD mostly correspond to the same peaks in FPR. However, it was observed that there is a more prominent peak in RMSD compared to FPR during the documented flood, which is the expected behavior for a no-flood reference.

For both the FPR and the RMSD, the HPAR performs less well than the exponential filter. In terms of exponential filter T value, most perform similarly. Aside from $T = 10$ and $T = 20$, they have varied performances relative to the other T values, sometimes getting the best and worst results in others.

4.6.1.2 Greece

Greece (Figure 4.4) is presented to show the behavior of a warm temperate study site. Regarding the FPR, it is observed that the exponential filter model performs better than

the harmonic model for most of the year. Like the previous plots, the lower T values showed inconsistent performance compared to the other T values. The performance of other T values is difficult to differentiate. A similar pattern is observed for the RMSD, where the harmonic model consistently shows higher values than the exponential filter model.

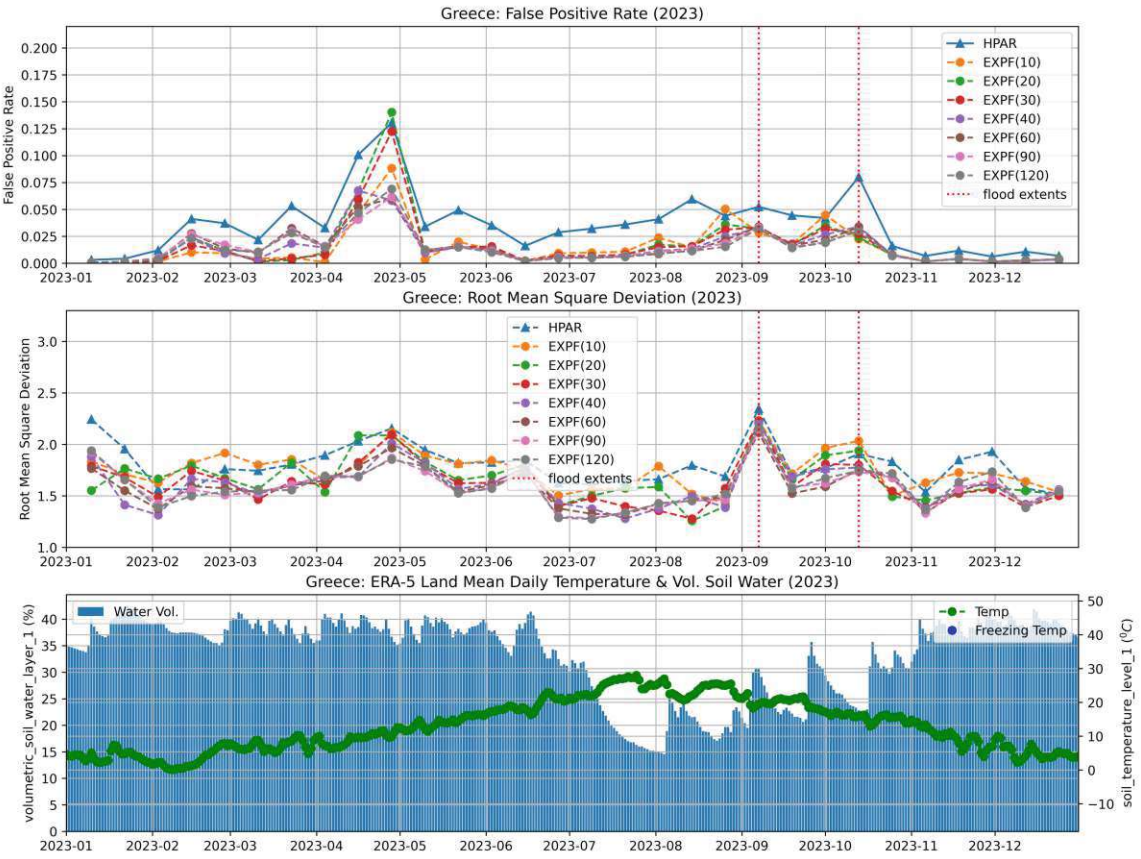

Fig. 4.4: Temporal Plots of False Positive Rate, Root Mean Square Deviation, and ERA5-Land Soil Temperature and Volumetric Soil Water for the Greece Study Site

A significant flooding event on this tile lasted from most of September to early October [44]. We observed elevated RMSD and FPR values during this period.

In contrast, there is a significant increase in FPR from most of April to May, which does not have a distinct rise in RMSD. Looking at the ERA5-Land plots, this April-May increase does not correspond to frozen soils or dry conditions. Thus, the most likely cause is the start of agricultural activity in the region, where bare ground or emergent vegetation typically exhibits low backscatter [42] and is maybe mistaken for flooding.

The considerable spike in FPR here can be explained by the large proportion of the agricultural area in the tile and the particular crops grown in this area. The more significant difference in performance between the harmonic model and exponential filter can be attributed to the same issue and is explained further in the spatial context in Section 4.6.2).

4.6.1.3 India

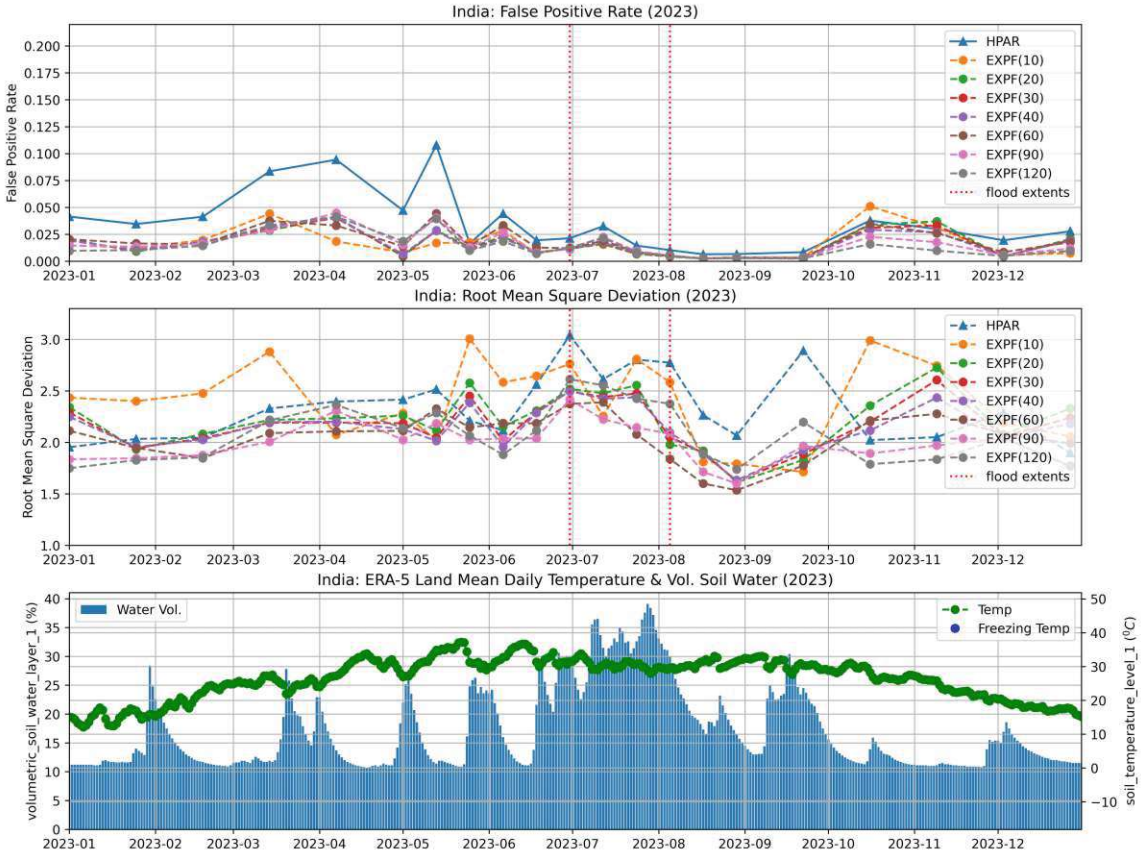

Fig. 4.5: Temporal Plots of False Positive Rate, Root Mean Square Deviation, and ERA5-Land Soil Temperature and Volumetric Soil Water for the India Study Site

The Indian study site (Figure 4.5) is in an arid climate. Therefore, dry soil conditions primarily drive the temporal dynamics of FPR and RMSD. An increase in FPR and RMSD is observed from April to May due to dry soil conditions. A larger increase in RMSD was observed during the prolonged flood event in July. Compared to dry conditions, no prominent increase in FPR was observed. For the India study site, the harmonic model and all T parameterizations of the exponential filter performed similarly for the second of the year, with a noticeable difference from the start of the year until June.

4.6.1.4 Southeast Asia

The Vietnam and Philippines test sites have tropical climates and show less variation in the FPR and RMSD. This observation can be attributed to relatively stable soil moisture and temperature throughout the year.

In the case of the Philippines (Figure 4.11), a large percentage of the tile are dense tropical forests; thus, backscatter variations are small [140], leading to stable tile-based aggregates where no peaks were observed in RMSD and FPR. The harmonic model and the exponential filter (regardless of the value T) are almost indistinguishable.

For Vietnam (Figure 4.13), there is greater variance in terms of RMSD as the climate is not purely hot and humid for the whole tile. Like Indian example, the harmonic model also performs worse than the exponential filter for the year's first half. Unlike the other test sites, the harmonic model and exponential filter perform similarly for no-flood scenarios in the Southeast Asian test sites.

4.6.1.5 General Perspective on False Positive Rates

To get a generalized perspective on the no-flood models' FPR performance, we further analyze the aggregated observations from all study sites. As observed in the time series metrics plots, the no-flood models' FPR performance show obvious similar trends following known environmental drivers. Thus, to differentiate the models, we statistically test the significance of the FPR differences per pair of no-flood models from all test sites.

The paired FPR differences between the various no-flood models showed significantly skewed (non-normal) distributions. Hence, the non-parametric Wilcoxon test [89, 131] was used instead of the paired t-test to test for significance. For this test, the null hypothesis (H0) states that there is no significant difference between the compared no-flood models. While the alternative hypothesis (H1) indicates a significant difference.

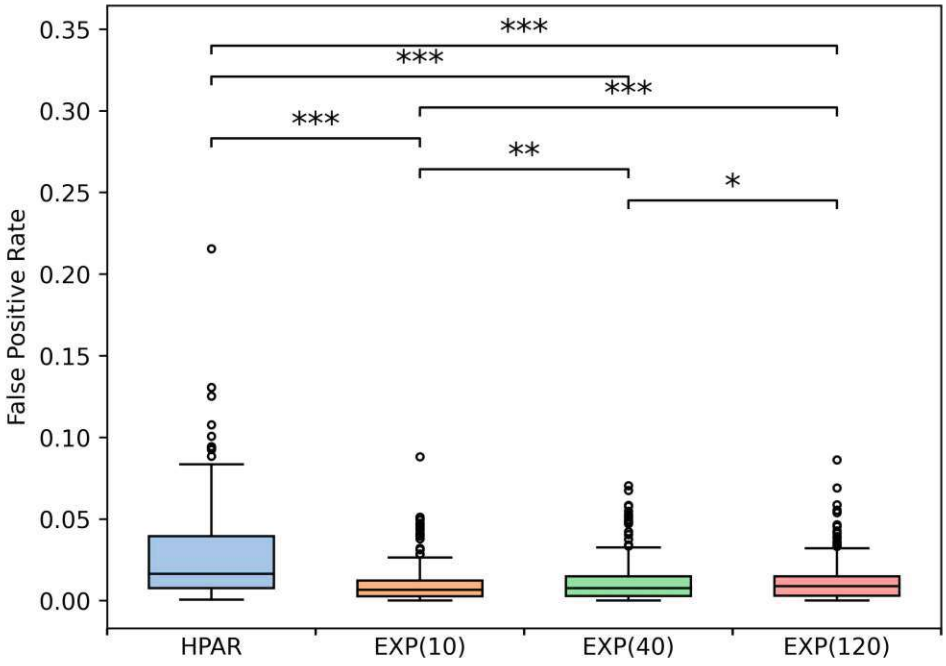

Fig. 4.6: Box and whisker plots of the aggregated False Positive Rates Forwith the significance level. ***: p-values < 0.001, **: p-values < 0.01, *: p-values < 0.05, and ns: p-values $>= 0.05$

Figure 4.6 shows Box and whisker plots of the aggregated False Positive Rates of selected no-flood reference model. Shown on top is the significance based on the pairwise Wilcoxon test. Almost all no-flood models showed significant statistical difference compared to others, except for T=60 compared to T=90 and T=120 (see Table 4.2). Notably, the HPAR model against all Exponential model showed the highest (***) significance, while between

the exponential filter models per T values show lower significance as T values become larger. On the box plots, we can see median FPR values of each no-flood model. The harmonic model in general shows about 0.027 FPR to less than 0.013 for all exponential filter models. Meanwhile, the differences in median FPR values between the exponential filter model at various T values are very small (although statistically different).

4.6.2 False Positive Frequency Mappings

To delve deeper into the issue of overestimation, we shift our focus from analyzing the time series data at the tile level to considering the spatial dimension. By generating flood frequency maps [87] and excluding instances from flood dates, we can represent the occurrence of false positives in each pixel. These maps enable us to assess how the false positive rates align with land cover and crop type. We compare the false positive (FP) frequency map based on the harmonic model and the exponential filter with $T = 40$ alongside the EU Crop map for specific locations as examples.

Consistent with the initial findings of Bauer-Marschallinger et al., we find further evidence of overestimation due to agriculture. In the Greek study site, as shown in the upper row of Figure 4.7, there is a noticeable variation in false positive frequency at the level of individual agricultural plots. Many agricultural plots are falsely labeled as flooded up to one-third of the year, some even exceeding 40%, and thus indicating a clear disadvantage of the harmonic modeling at this location.

There are noticeable differences in FP count between plots growing maize and cereals compared to industrial crop plots, the latter being more easily misinterpreted as flood labels. He et al. identify cotton as the most prevalent industrial crop. The sensitivity of cotton fields to false labeling can be attributed to agricultural practices (e.g., field flooding) and the higher backscatter of the cotton plant in the middle of the cropping stages, leading to a higher temporal model variance [68].

The grasslands of the Slovenian test site shown in the lower row of Figure 4.7 have higher FP frequencies. From open optical satellite imagery, these areas appeared to be seasonally flooded and were missed by water masks. In these regions, the exponential filter shows fewer FPs. In the northeast corner of the map, some distinct agricultural plots are also apparent in the frequency maps, such as rape. Maize has fewer FPs on this site compared to Greece.

Bare soils, grasslands, and croplands show more FPs than other land cover types. In terms of other specfic crops, we observed with elevated FPs from other test sites include wheat, cereals, and rice (see Section 4.10.3). These crops have been shown to have low backscatter periods during their growing stages [14, 42, 124]. However, there seems to be a site variation in the FP frequency of most crops.

In both exemplar flood frequency maps, the spatial patterns of FP are similar. However, the harmonic model shows significantly more FPs than the exponential filter, consistent with the temporal FPR plots.

4.6.3 Flood Scenarios Quantitative Analysis

Next, we focused on flood mapping performance on flooded dates with reference flood maps. The critical success index of the flood maps using the baseline harmonic no-flood reference

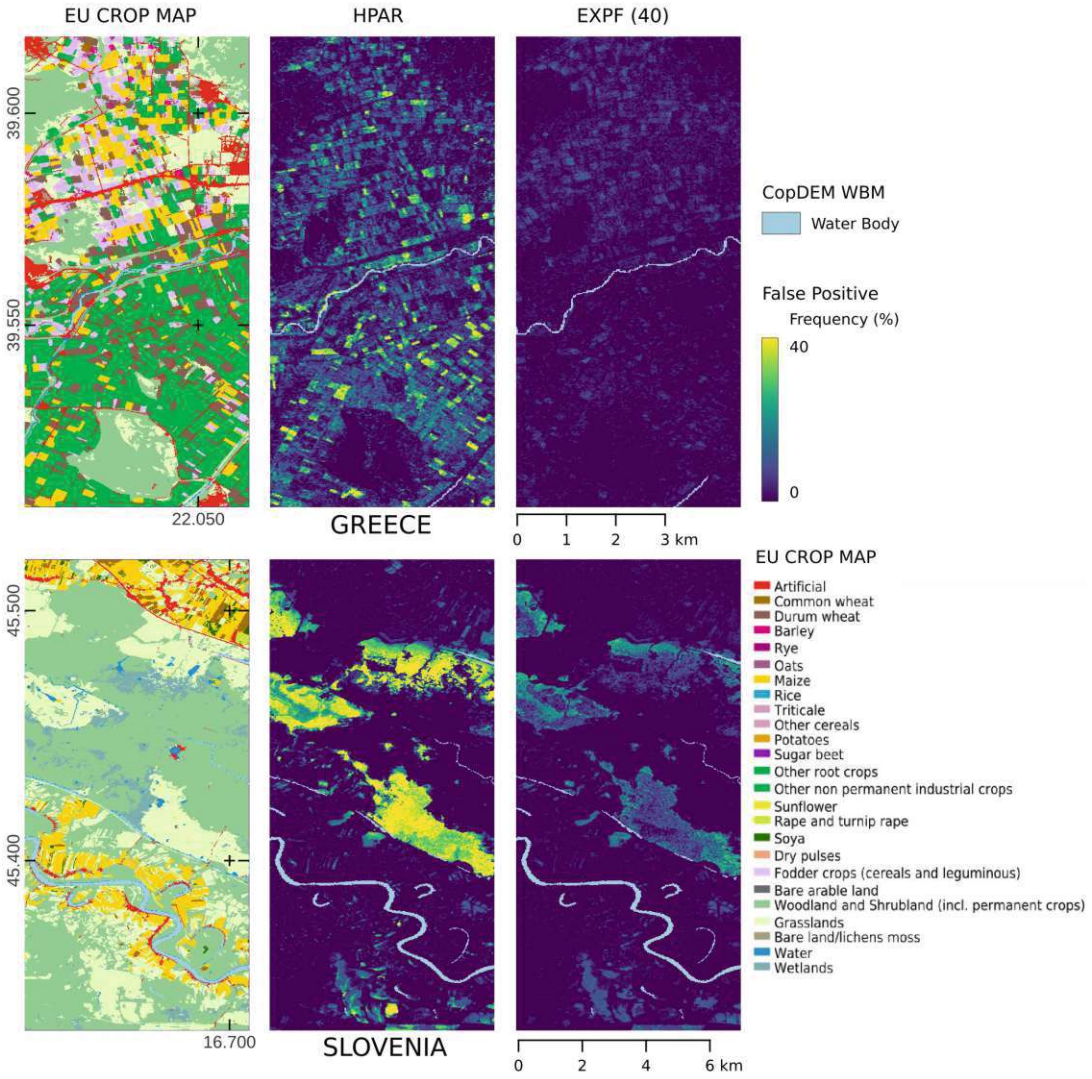

Fig. 4.7: Flood False Positive (FP) Frequency Maps of Greece and Slovenia Study Sites. Greece N=26, Slovenia N=29 where N is number of observations less actual flooded images. EU Crop cover map is provided as reference.

where 60.87%, 44.02%, 56.38%, 41.90%, 58.08%, 68.04%, and 54.71% for the study sites in Latvia, India, Philippines, Slovenia, Greece, Vietnam and Scotland respectively. On average, the seven study sites got 67.12% for User's Accuracy and 79.53% for Producer's Accuracy. These accuracy assessment results are consistent, but are nominally lower, with the similarly sized events and same environmental conditions examined when using the TU Wien flood mapping algorithm [119]. This study obtained lower values because of non-application of external exclusion masks.

To differentiate the performance of harmonic model versus the exponential filter, we show Figure 4.8 where we plot the differences in CSI, UA, and PA of all our test sites.

Regarding CSI, we compare the performance of the no-flood references within sites. The varying sizes of flood extents, as shown in Table 4.1, influence the CSI [107]. Consequently, we avoid direct inter-site comparisons based on the CSI. We focus on the comparison of

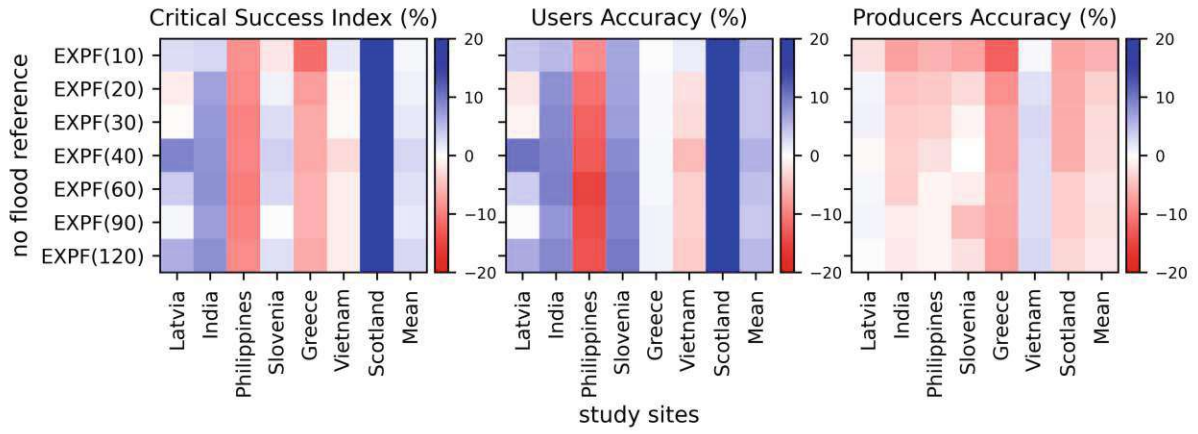

Fig. 4.8: Heat Maps Summarizing Difference in Critical Success Index, User's Accuracy, and Producer's Accuracy of Flood Maps Between the Harmonic Model and Exponential Filter Models with Various T Parameters (y-axis) for the Seven Study Sites (x-axis)

the no-flood models in regard to the original harmonic model method, thus we present the differences relative to the HPARs shown in Figure 4.8. With this differencing, we reduce the bias in CSI to be able to make more generalized observations.

The exponential filter performs better than the harmonic model in Latvia, Slovenia, and India. In Vietnam, the harmonic model is comparable to the exponential filter. Meanwhile, the exponential filter performs significantly better at the Scotland study site. The harmonic model performs better than the exponential filter in the Greece and Philippine study sites. We further discuss the cause of the poor performance of the exponential filter in section 4.6.4.3 on prolonged floods that are apparent in these two test sites.

In terms of the T parameter, the CSI difference decreases as T increases for both study sites in Southeast Asia. This observation is consistent with our initial results [117], where the harmonic model outperforms the long-term means as a no-flood reference. Apart from the Scotland study site, which shows slightly increasing performance at larger T values, all other test sites show better performance at mid T values, most often peaking at $T = 40$. This is reflected by the mean of the differences for the tested sites also peaking at the same T, with a modest 3.06% in CSI.

The middle panel in Figure 4.8 shows the UA plots of all study sites. It should be recalled that the UA is inversely related to the commission error. In most study sites, aside from the Vietnam and Philippine study sites, we see that the exponential filter typically shows less overestimation. Only the Scottish case showed a stark difference in UA values, while most others showed minor improvements. On average, there was 5.75% increase in the User's accuracy at the same peak T value of 40.

Commission errors increase with increasing exponential filter T values in Scotland, Vietnam, and the Philippines. In contrast, a middle peak is observed in Latvia and India. Furthermore, we note an almost stable but slightly decreasing trend in Greece and Slovenia.

In the rightmost panel in Figure 4.8, we plot the PA–the inverse of omission errors, of the sites we tested. In general, the harmonic model flood maps show less underestimation.

Greece is the only site with severe underestimation in the exponential filter. Most sites show slightly fewer omission errors. The exponential filter T values show a mainly increasing PA trend. Unlike the CSI and UA, PA of the exponential filter models had a decrease compared to the harmonic model. The best performing T value in case is $T = 120$ with 1.79% mean decrease, while at $T = 40$ with 2.58% decrease on average was observed.

4.6.4 Flood Scenarios Confusion Maps

To put the comparative metrics discussed into spatial context, we show exemplary confusion maps highlighting the benefits and issues with the no-flood reference models we tested.

4.6.4.1 T Parameter of the Exponential Filter

We present the study site in Scotland shown in Figure 4.9. Here, we show the eight confusion maps pertaining to the harmonic model and the exponential filter at varying T. The harmonic model produces more false positives compared to the exponential filter.

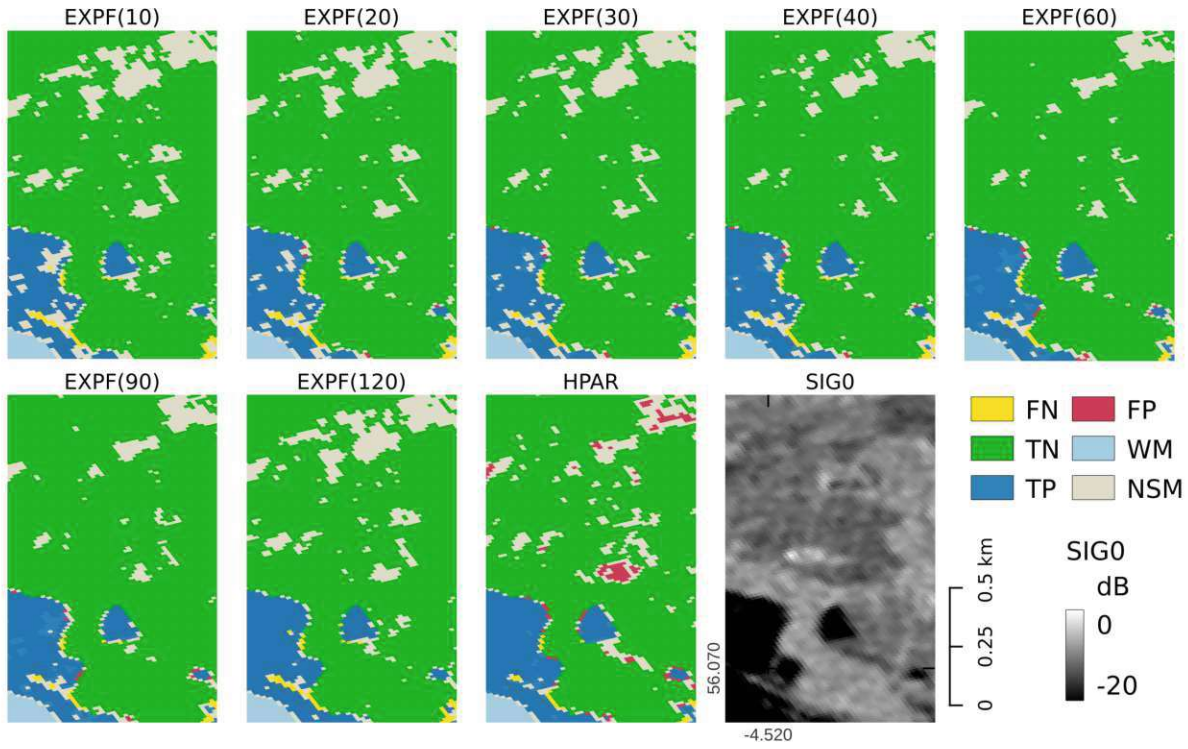

Fig. 4.9: Scotland study site confusion maps, computed from flood maps on 2023.10.08 generated using the harmonic model (HPAR) and exponential filter (EXPF) at various T values against CEMS rapid mapping product. Legend: FN - false negative, TN - true negative, TP - true positive, FP -false positive, WM - reference water mask, NSM - TU Wien no sensitivity mask. Flooded SIG0 backscatter is presented as reference.

Although the flood delineations from the exponential filter remain relatively consistent, intermediate values, such as $T = 40$ to $T = 90$, visually perform better. We observed

higher and lower T values to have more No-sensitivity masked (NSM) pixels in both flooded and non-flooded areas. Similarly to most cases, this example shows more TP pixels for the harmonic model, thus higher PAs. Based on these visual observations and optimal performance indicated by the mean differences, $T = 40$ is an appropriate initial choice for the flooded scenario.

4.6.4.2 Reduced Overestimation

For conciseness, we show the exemplary performance of the harmonic model and the exponential filter at $T = 40$ in Figure 4.10, as the performance based on the T values, in most cases, reflects that of the Scotland site depicted above. We show insightful subsets of the confusion maps for four other sites covering diverse environmental zones.

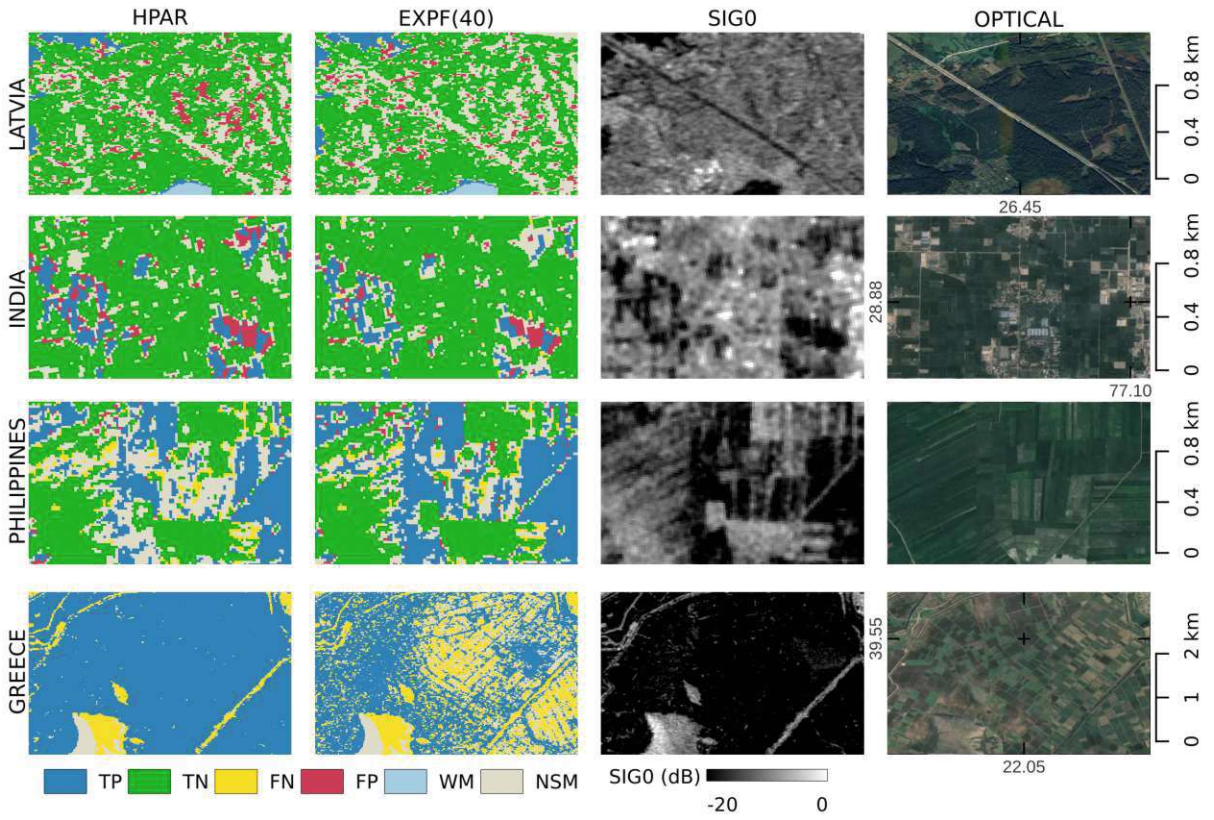

Fig. 4.10: Flood confusion maps from Latvia (top row), India (2nd row), Philippines (3rd row) and Greece (bottom row) study sites. Flood confusion maps from flood maps using harmonic model (left most column) versus exponential filter at T=40 (2nd column) with the flooded SIG0 backscatter (3rd column) and optical image from Google (rightmost column) as reference. Legend: FN - false negative, TN - true negative, TP - true positive, FP -false positive, WM - reference water mask, NSM - TU Wien no sensitivity mask.

The confusion maps for the study site in Latvia are shown in the first row of Figure 4.10. This study site suffers from high commission errors and is most apparent in sparse

blobs of FP pixels. There are larger FP blobs from harmonic model flood maps compared to the exponential filter maps. Some of the reduced FP patches in the exponential filter model appear on dense vegetation and might be removed through exclusion masking. This can be perceived both positively and negatively; it suggests potentially lesser dependency on exclusion masking but also indicates that there might be limited improvement if they were masked.

In contrast, the exponential filter maps have sparse no-sensitivity masked pixels within the flooded area, thus missing TP pixels. Recall that the no-sensitivity mask covers pixels with similar no-flood and flooded distributions. FNs are a minor issue for both maps tested in this study site.

The second row of Figure 4.10 shows the confusion maps for the Indian tile. This map shows reduced flood labels from the exponential filter for TP and FP areas. Consequently, this reduces the commission errors but increases the omission errors similar to the temperate study sites discussed above.

A subset of the Philippine test site is shown in the third row of Figure 4.10. A cursory check of the Philippine Rice Information System (`https://prism.philrice.gov.ph`)[67] reveals that this area is mainly cultivated for rice. The harmonic model showed more prominent areas of omitted TP but consequently fewer FP. This area appears to be problematic for the static harmonic model to estimate. We attribute this to year-to-year variations in the rice planting season [41], which causes temporal shifting leading to higher than usual variability in the temporal radar back scatter signature. While this issue occurs for most land cover types, this is very pronounced in rice fields due to paddy flooding (very low backscatter) at start of season. This results in ill fitting no-flood reference causing the significantly large no-sensitivity masked area.

In contrast, the dynamic nature of the exponential filter is beneficial in this area. It should be noted that the overall metrics of the whole Philippine site do not match this sample area, as there are far more significant areas of missed TP from the exponential filter from prolonged floods (further discussed below).

4.6.4.3 Long Floods

The test sites in Greece and the Philippines have lower exponential filter performance. We consider it consequential that these test sites were documented to have had prolonged floods [43, 44]. This points to a deficiency of the exponential filter in accurately modeling the no-flood reference probability distribution.

This results in underestimation at the Greece test site is highlighted in the bottom row of Figure 4.10. Prolonged flood results in lower backscatter estimates from the exponential filter; thus, the no-flood probability distribution moves closer to the flood probability distribution, causing conflicting distributions in some cases. As the exponential filter standard deviation was computed from the 2023 time series, we observed elevated variance which can be attributed to the prolonged floods in the area, thus exacerbating the underestimation issue.

4.7 Discussion

4.7.1 No-flood conditions

As expected, most of the increase in FPR at the tile level can be attributed to frozen soil [5] and dry conditions [83] supported by ERA5-Land data. Agricultural overestimation - unrelated to these conditions - which has been observed mostly on local scales [8, 17] we have now shown instances where they also cause a significant increase in FPR at the tile level.

Although the case of overestimation due to frozen soils and dry conditions could be effectively identified from auxiliary data (as is done in GFM [74]), the effect of low backscatter due to agriculture is much more challenging to address due to local variations. Our analysis of FP frequency reveals that this overestimation is influenced by the type of crops and cropping practices, as evidenced by plot-level variation. This observation suggests the possibility of seasonal and land cover class-based correction or reliability metric; thus, it is recommended for future work.

Although these overestimation issues in no-flood conditions were not completely eliminated, switching to an exponential filter-based no-flood reference improves overall performance. In most cases, the FPR of the exponential filter model is less than half of the harmonic model. We observed that the FPR differences between the harmonic model and the exponential filter is more pronounced in sites with clear seasonality. Temperate and arid regions benefit more compared to the tropical areas where there is no clear improvement.

In general, the FPR of the exponential model does not vary much based on T value. For several test cases, T values of 10 and 20 showed inconsistent results. There are instances where they have the lowest FPR but more often have the higher FPRs. Even on the tile level, all other T values were difficult to distinguish based on their performance FPR and RMSD values. Thus, to safely limit FPR in cases without flood, we suggest T values starting at 30.

The time series assessments were limited to the same Sentinel-1A relative orbit of the reference flood data to remove effects due to changing imaging geometry [100]. This means that for the 2023 time series per orbit, there were at most 30 samples per tile we analyzed. We recommend that a longer time-series analysis, e.g. two years, be conducted in the future. The flood time series and frequency analysis relies on the accuracy of the reference water mask [92]. The seven locations examined in this study do not exhibit substantial seasonally flooded regions; however, overlooking the possibility of localized genuine floods might result in the extent of false positives to be overstated (see Figure 4.7). Although we consider this a minor issue for the sites tested e.g., no big spikes in FPR in Slovenian case, we suggest using a higher quality and more consistent mask in future research.

4.7.2 Flood conditions

Based on CSI, UA, and PA values, the TU Wien flood mapping algorithm showed good performance relative to the reference flood maps for most of the seven validated flood events. The confusion maps presented mainly corroborated the quantitative trends of decreased FP from the exponential filter maps compared to the harmonic model maps.

We find a similar result of reduced overestimation with the exponential filter for the flooded scenes where reference flood maps were available. From the differences in the CSI, UA, and PA trends based on the values of T, we found that $T = 40$ is a good choice for most study sites. This selection corresponds to roughly nine Sentinel-1 observations and about four months in the temporal range. This criterion is similar to the common suggestion from literature to limit no-flood reference input to images near in time or season [18, 47].

Further, the computational needs for this number of input images seem reasonable, unlike higher T values which would be unmanageable at global scale. The number of input images appears consistent with suggestions of five images minimum [52] as we see $T <= 20$ with less than five inputs having degraded performance. These qualitative trends are corroborated by confusion maps that point to the tested middle values T preferred over the lower and higher values. As the T value is less significant in the non-flooded scenes we select $T = 40$ as our default choice.

However, unlike in soil moisture studies where the T parameter has been well documented [3, 85, 88] and uses higher temporal resolution inputs, we can only use comparatively limited backscatter observations. Consequently, the number of observations used to make a no-flood estimate depends on the T value. Distinguishing the effect of the model independent of the number of observations is not possible from our experiments. Further, while care was taken to match reference flood maps to our results to minimize external differences (e.g., temporal and spatial mismatches), the reference data used are not actual ground truth. Thus, over and under-detection due to the limitations of flood retrievals from SAR backscatter are persistent in the analysis.

4.7.3 T-value selection

Based on the flooded and non-flooded test scenarios described previously, we have identified $T = 40$ as a reasonable selection based on several considerations. First, while most T values are quite similar, lower T values ($<= 20$) for specific test sites exhibited increased variance, prompting us to limit our range to $T >= 30$. Second, as shown in Figure 4.9, mid-range T values (40 to 90) present a more favorable pattern with less noise and less no-sensitivity pixels. Third, average metrics for flooded scenarios indicate a preference for $T = 40$. Finally, higher T values ($>= 90$) are computationally expensive, even for initializing the recursive formulation.

4.7.4 Long Floods and Exponential Filter Prospects

It is also clear that prolonged floods severely affect the performance no-flood references using the exponential filter model. While this issue is localized to pixels with longer floods and does not affect the overall performance in other regions a generalized solution is needed. A simple solution is to remove flooded Sentinel-1 images as inputs. However, the automated identification of images that contain floods is a significant scientific question on its own. Some workflows suggest using auxiliary markers, such as precipitation [52], to omit dates with a high probability of being flooded. Another possibility is the removal of flooded scenes based on some (non-)similarity metric [47]. Although requiring significant

infrastructure to execute, a recent method based on detecting time series anomalies by Fichtner et al. is currently being used in GFM, showing promising results.

From our results in Section 4.6.1, there appears to be a potential to identify anomalies based on the ratios of the FPR and RMSD. There is often a good correlation between FPR and RMSD. When the FPR increases due to freezing soil conditions, a significant proportion of the area changes, meaning the RMSD also increases. In contrast, the increase in FPR due to dry (and, to an extent, cropping practices) has a longer duration but proportional increase in RMSD.

Flood events appear as anomalies that do not follow this trend. Floods often cover a small portion of a 300 km-wide Equi7Grid T3 scene; hence, FPR does not increase much. Since RMSD is sensitive to outliers, a significant decrease in backscatter due to floods increases the RMSD even in cases where floods are relatively small. However, there seems to be inter-site variance; thus, it is unexplored here and left for future work.

4.8 Conclusions and Outlook

In this study, we assessed the performance of different no-flood parameterizations of the TU Wien flood mapping algorithm using a novel non-flooded time-series approach and traditional qualitative and quantitative flood map assessments. We analyzed the algorithms performance on varying environmental and climactic zones for one year time-series. In doing so, we highlight spatio-temporal patterns of overestimation.

While the importance of a no-flood reference in SAR flood mapping algorithms has been extensively covered [35, 47, 60, 101, 141], the impact it has on the overestimation of automatically classified non-flooded scenes has not been given attention until now. We find that flood overestimation at scale could be triggered not just by frost and dry soil conditions but also by agriculture. Further, the degree of agricultural overestimation depends on the crop type and agricultural practices.

Aside from limited testing we introduced in a previous work [119], to our knowledge this concept of testing flood mapping methods on non-flooded times series scenes have not yet been attempted before. This work sheds light on the frequency of these different overestimation issues, thus highlighting the need for further studies to reduce them.

We compared the original harmonic and novel exponential filter models with no-flood references, with the latter showing promising performance. Similar to observations from recent studies [19] the enhanced modeling of the no-flood reference resulted in improved flood maps. The exponential filter reduced overestimation in both flooded and non-flooded conditions. This is supported by improved flood labeling in areas where dynamically updated no-flood models are required. Reduced overestimation by switching to the exponential filter can be complemented using topography-based priors [119], which improved the underestimation.

We found that the exponential filter with $T = 40$ provides a good balance in performance for both flooded and non-flooded conditions. This T value requires a reasonable time series input (allowing for application at a global scale) to achieve good initial results. However, the recursive formulation is still a must for actual NRT operations. Provided computational cost does not prohibit NRT application, more advanced updating of temporal models e.g., Kalman filters [23, 55] should be explored.

Prolonged floods present an issue for the exponential filter based no-flood backscatter estimate and generated standard deviation, the two parameters needed to estimate the no-flood model probability distribution. Therefore, an automated screening of flooded Sentinel-1 images as input is strongly recommended for operational implementation both for the backscatter estimation and no-flood standard deviation calculation.

To conclude, we showed a holistic assessment of the TU Wien algorithm geared toward automated deployment over multiple climatic zones for flooded and non-flooded cases. As far as we are aware, analyses of flood mapping on this spatial and temporal extents have not been conducted previously. Understanding of the algorithm's limitations in the temporal and environmental context opens new avenues for improvement. While further development is needed, the exponential filter as a no-flood reference was shown to be a feasible alternative to the harmonic model. Overall, the exponential filter no-flood reference model shows great promise for improved global near-real-time flood mapping.

4.9 Acknowledgements

The computational results presented have been achieved using inter alia the Vienna Scientific Cluster (VSC). We would further like to thank our colleagues at TU Wien and EODC for supporting us on technical tasks on maintaining the datacube.

4.9.1 Funding

This research work was performed with support of the Engineering Research and Development for Technology Program of the Philippine Department of Science and Technology, the project "S1Floods.AT" (Grant no. BW000028378) founded by the Austrian Rsearch Promotion Agency (FFG) and the project "Provision of an Automated, Global, Satellite-based Flood Monitoring Product for the Copernicus Emergency Management Service" (GFM), Contract No. 939866-IPR-2020 for the European Commission's Joint Research Centre (EC-JRC). The authors acknowledge TU Wien Bibliothek for financial support through its Open Access Funding by TU Wien.

4.9.2 Data Availability

The data presented in this study are openly available at:
`https://doi.org/10.48436/3dd60-ydz51`.

4.10 Supplementary material

4.10.1 No-Flood Temporal Plots

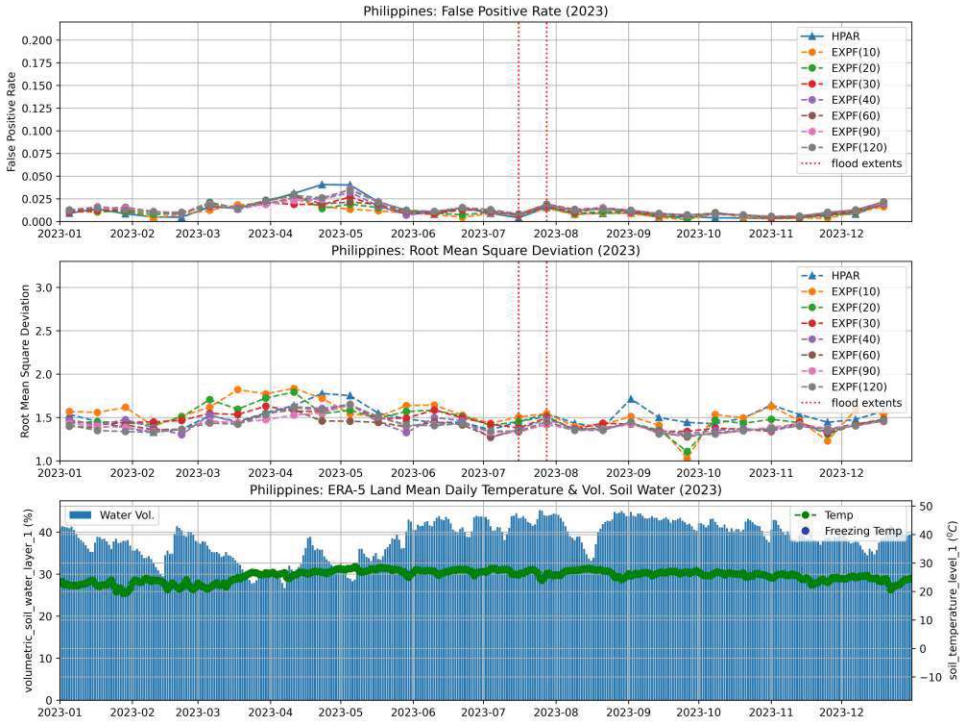

Fig. 4.11: Temporal Plots of False Positive Rate, Root Mean Square Deviation, and ERA5-Land Soil Temperature and Volumetric Soil Water for the Philippines Study Site

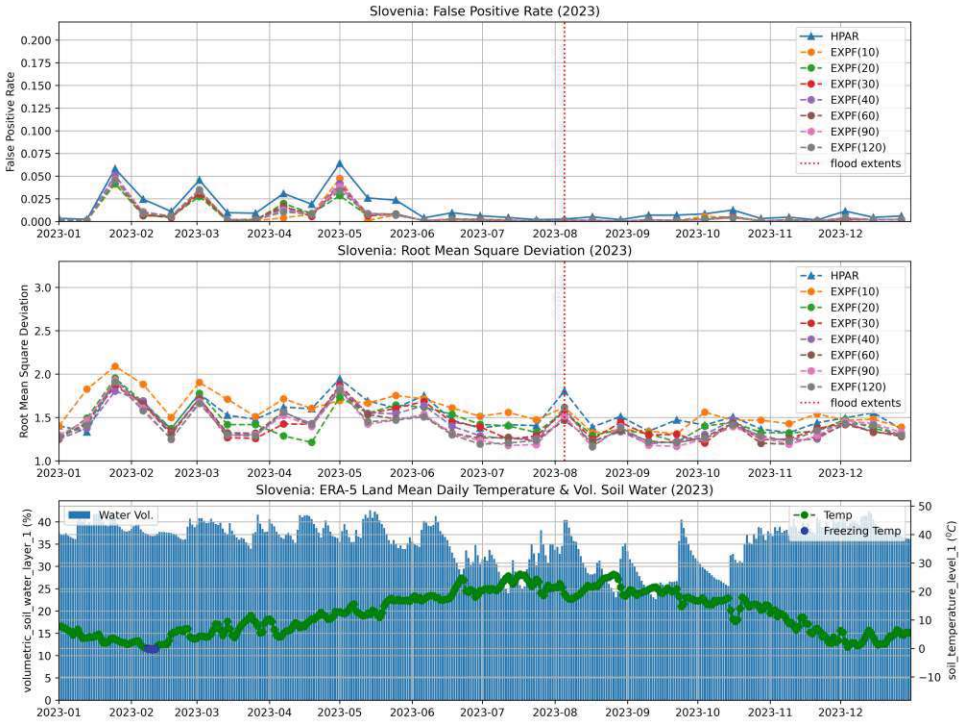

Fig. 4.12: Temporal Plots of False Positive Rate, Root Mean Square Deviation, and ERA5-Land Soil Temperature and Volumetric Soil Water for the Slovenia Study Site

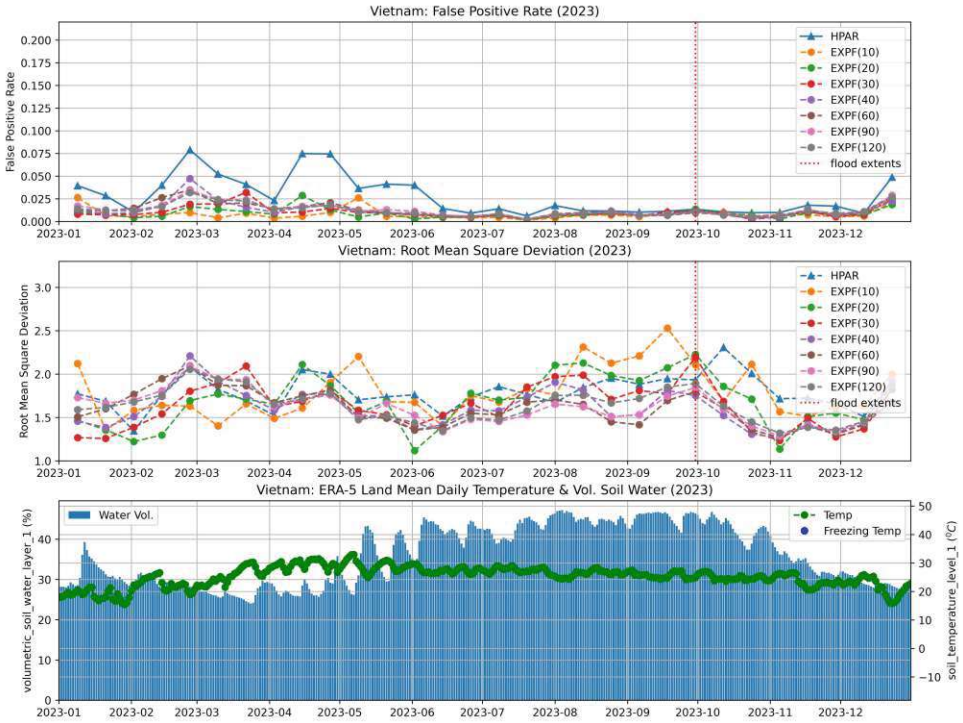

Fig. 4.13: Temporal Plots of False Positive Rate, Root Mean Square Deviation, and ERA5-Land Soil Temperature and Volumetric Soil Water for the Vietnam Study Site

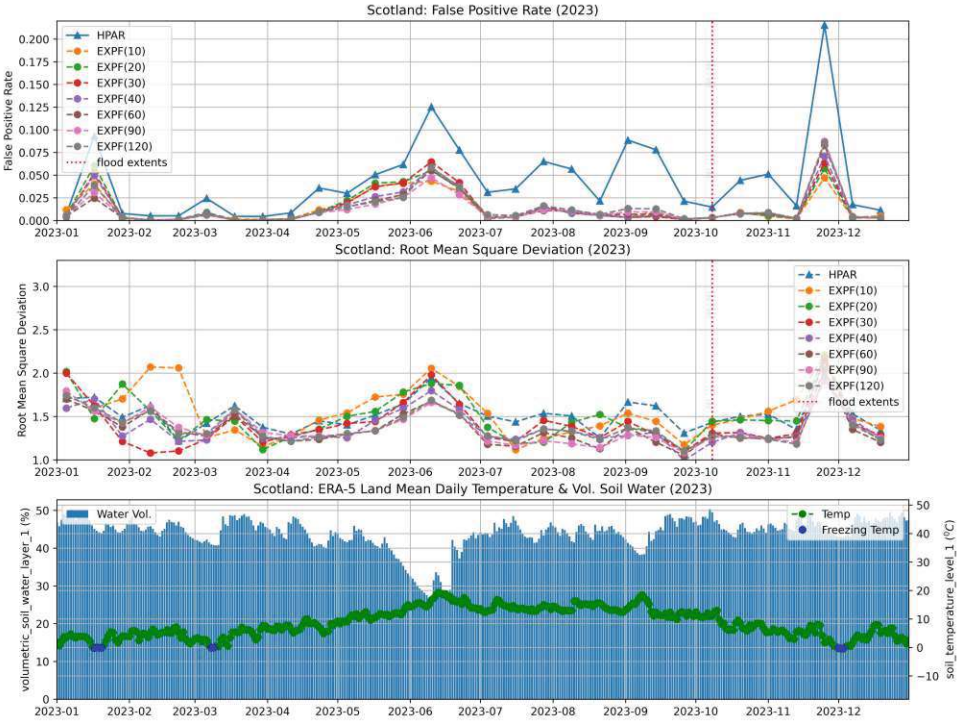

Fig. 4.14: Temporal Plots of False Positive Rate, Root Mean Square Deviation, and ERA5-Land Soil Temperature and Volumetric Soil Water for the Scotland Study Site

4.10.2 Pairwise Statistical Significance

Median FPR	paired p-values	HPAR	EXPF(10)	EXPF(20)	EXPF(30)	EXPF(40)	EXPF(60)	EXPF(90)	EXPF(120)
0.027	HPAR	—							
0.011	EXPF(10)	0.000	—						
0.012	EXPF(20)	0.000	0.011	—					
0.012	EXPF(30)	0.000	0.001	0.017	—				
0.012	EXPF(40)	0.000	0.002	0.005	0.012	—			
0.013	EXPF(60)	0.000	0.000	0.000	0.000	0.000	—		
0.012	EXPF(90)	0.000	0.000	0.000	0.000	0.001	0.489	—	
0.012	EXPF(120)	0.000	0.000	0.000	0.003	0.043	0.161	0.000	—

Tab. 4.2: FPR Wilcoxon tests p-values.

4.10.3 False Positive Frequency Maps

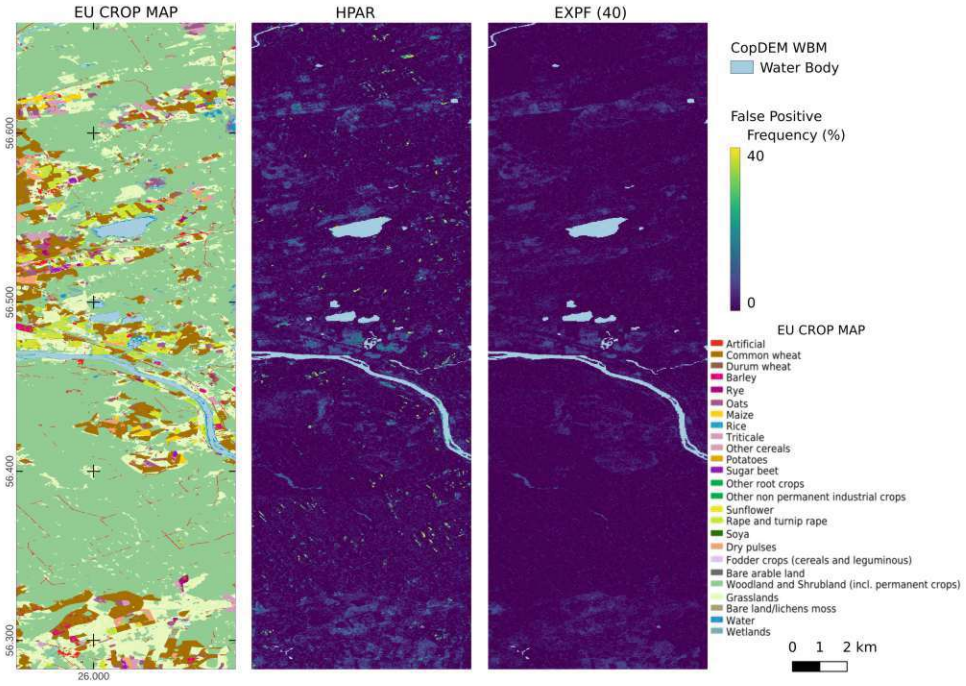

Fig. 4.15: Flood False Positive (FP) Frequency Maps of Latvia Study Sites. N=28 where N is number of observations less actual flooded images. EU Crop cover map is provided as reference.

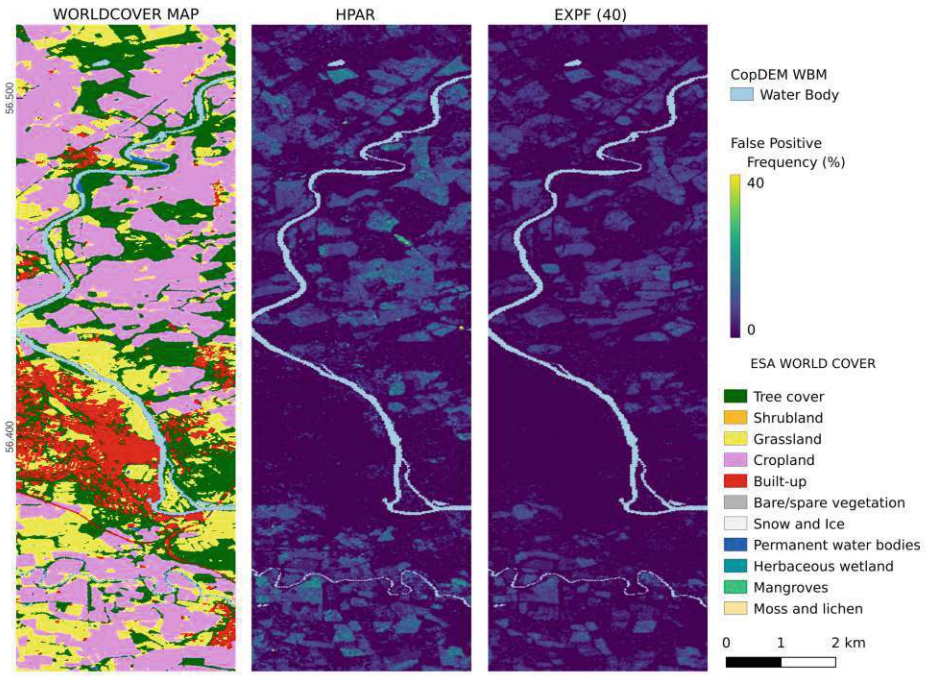

Fig. 4.16: Flood False Positive (FP) Frequency Maps of Scotland Study Sites. N=29 where N is number of observations less actual flooded images. ESA Woldcover map is provided as reference.

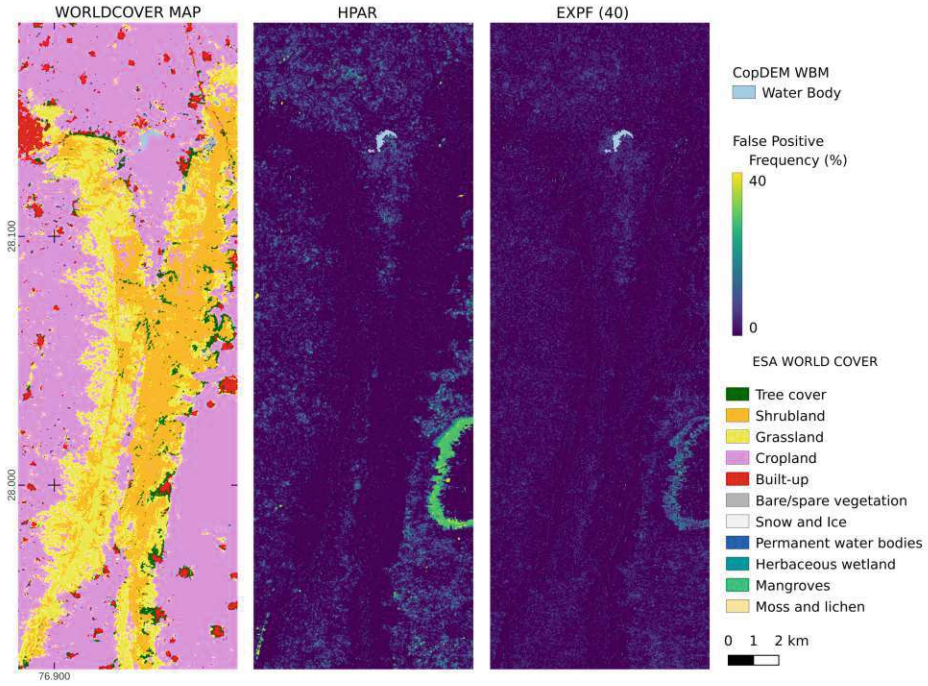

Fig. 4.17: Flood False Positive (FP) Frequency Maps of India Study Sites. N=17 where N is number of observations less actual flooded images. ESA Woldcover map is provided as reference.

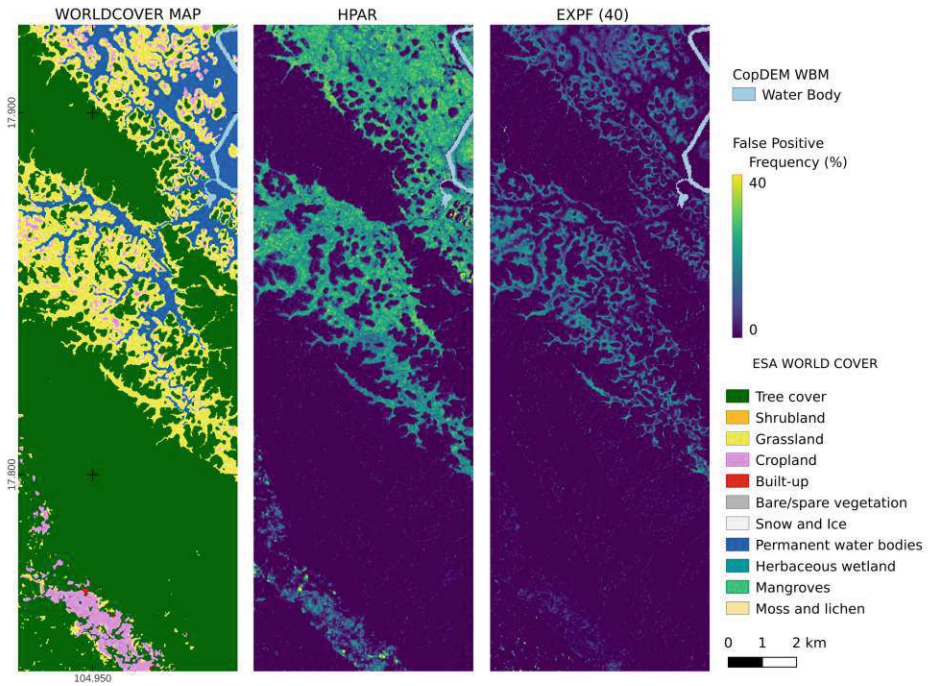

Fig. 4.18: Flood False Positive (FP) Frequency Maps of Vietnam Study Sites. N=29 where N is number of observations less actual flooded images. ESA Woldcover map is provided as reference.

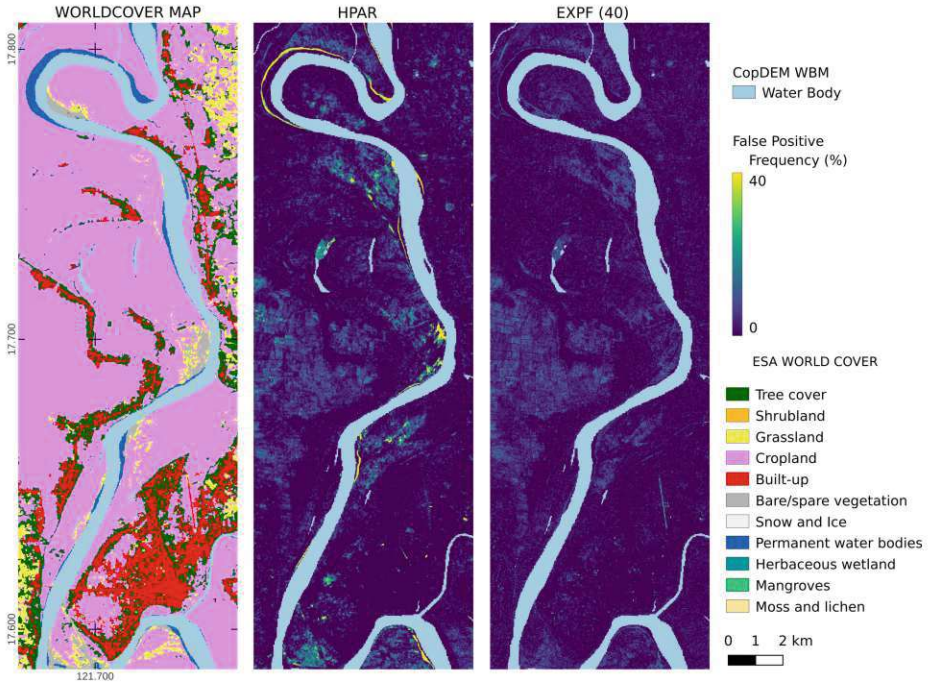

Fig. 4.19: Flood False Positive (FP) Frequency Maps of Philippines Study Sites. N=28 where N is number of observations less actual flooded images. ESA Woldcover map is provided as reference.

4.10.4 Comparison of Mean and Exponential Filter

To establish the feasibility of using the exponential filter as a no-flood reference over other time-series filters, we show a preliminary analysis of the mean and exponential filters compared to the harmonic-derived no-flood reference at different parameterizations. These baseline results were performed using the same SAR datacube for the CEMS (Greece, Slovenia, Latvia, and Scotland) study sites without the speckle filtering step (thus slightly varies with our main results). Mean and median filters had nearly identical results; therefore, only the mean, the harmonic model, versus the exponential filter, is presented here. The mean parameterizations presented are based on the temporal selection criteria (i.e., in days prior to the backscatter image acquisition date) for the input backscatter images.

In Figures 4.20, and 4.21, we compare the no-flood reference performance for flood mapping using the mean filter using 90 days prior images, the baseline harmonic model, and the exponential filter at T=30. These mean and exponential filters were selected to make a fair comparison because these parameterizations effectively require the same input images (see Section 4.3.2).

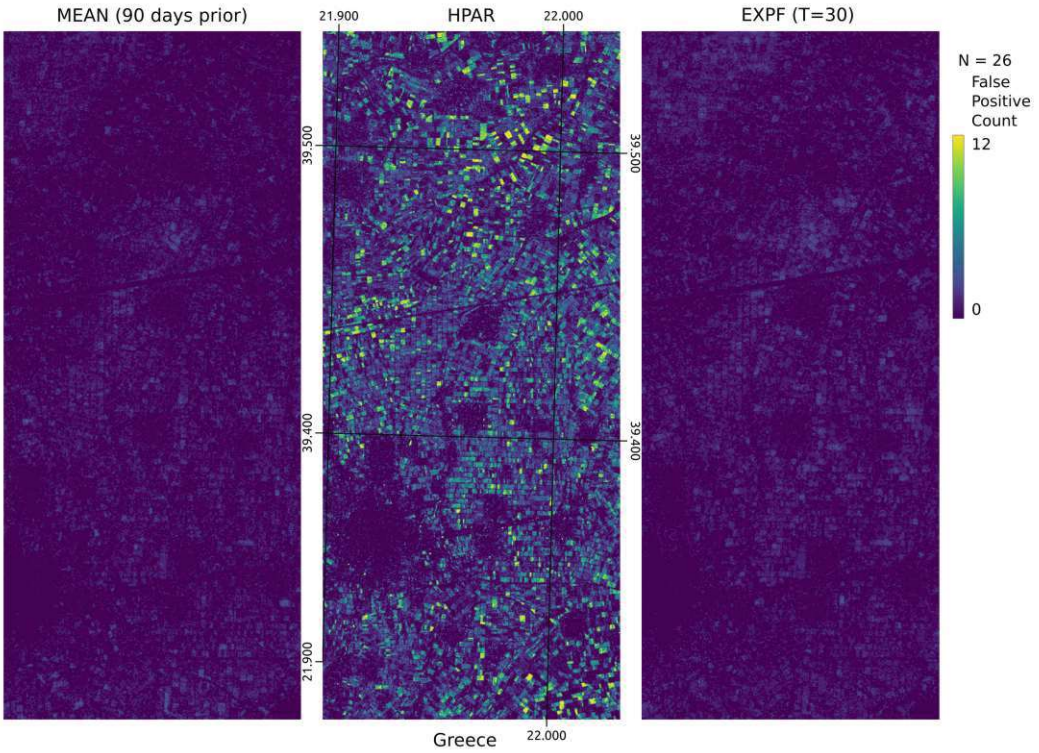

Fig. 4.20: Flood False Positive (FP) Count Maps of Greece Study Site Comparing the Mean and Exponential Filter versus the Harmonic Model as no-flood references. N=26, where N is the number of observations of less actual flooded images.

In Figure 4.20, we see the stark contrast between the false positive counts from the harmonic model versus the mean and exponential filters. On the other hand, the exponential and mean filters show minor differences in total false positive counts between them.

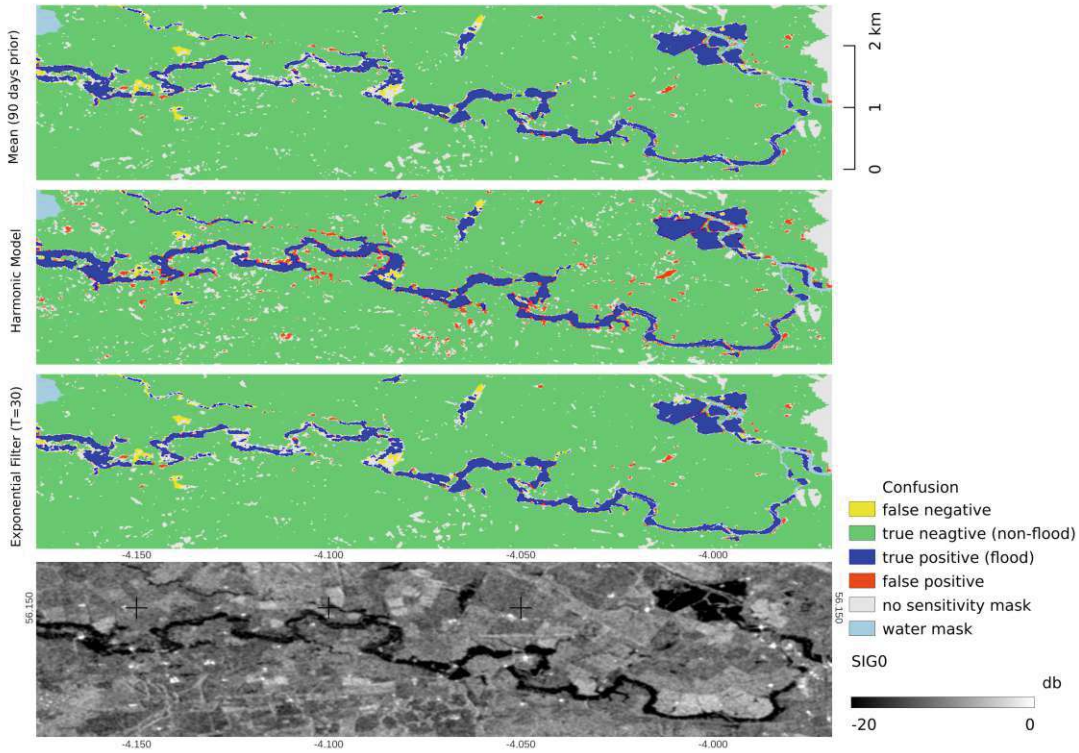

Fig. 4.21: Flood Confusion Maps of Scotland Study Site Comparing the Mean and Exponential Filter versus the Harmonic Model as no-flood references. Legend: FN - false negative, TN - true negative, TP - true positive, FP -false positive, WM - reference water mask, NSM - TU Wien no sensitivity mask.

In Figure 4.20, we observe similar flood maps generated for the Scotland study site using the mean filter (90 days prior) and the exponential filter (T=30). The harmonic model results are included for reference.

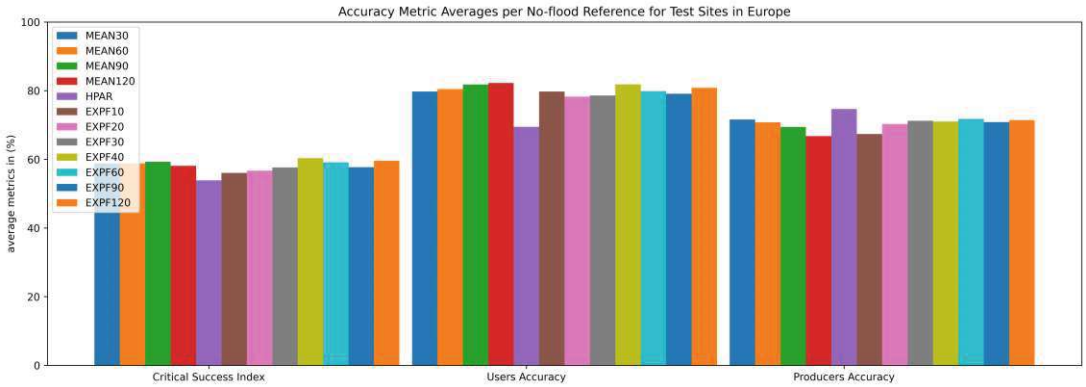

Fig. 4.22: Average of Accuracy Assessment Metrics for the Study Sites in Europe Comparing the various parameterizations of the Mean Filter, Exponential Filter, and Harmonic Model.

Figure 4.22 shows the average CSI, UA, and PA of the various parameterizations of the mean filter and exponential filter versus the harmonic model for the European study sites. It can be observed that the mean and exponential filters show similar improved performance in terms of CSI. Both filters show similar responses to UA and PA, where the time-series filter-based no-flood models perform better than the harmonic model in terms of UA but slightly worse performance in PA. Similar to the exponential filter, the mean filter also showed variations in performance based on its different parameterizations.

Chapter 5

Conclusions and Outlook

5.1 Conclusions and Potential Impact

As the demand for timely and accurate flood maps increases, it is essential to enhance our SAR-based algorithms continuously. While, more and more SAR flood mapping methods have been shown to work well, most of them were tuned and tested on a few study sites, and it is unclear whether they are viable for global NRT application. In this research we sought to improve on the TU Wien flood mapping algorithm that is already running operationally for the CEMS GFM. This thesis showed the viability of, and improvements to, the Sentinel-1 data cube based algorithm done by incremental changes to its Bayesian Inference framework.

Chapter 2 established the robustness of the TU Wien flood mapping algorithm compared to other change detection algorithms. This work showed that the harmonic model gives better results than individual prior images or long time-series means– indicating the need for dynamically or seasonally corrected no-flood references. Further, we found that the Bayesian algorithm is less affected by changes in its parameterization (unlike the other methods tested) and firmly supports its usage for global NRT operations. With no dependence on dynamically changing thresholds, it makes an excellent base algorithm that we subsequently improved on. The initial parameterization analysis done here has guided the ensuing improvement to the TU Wien algorithm and can be applied to other change detection or Bayesian methods.

In Chapter 3, we found that spatially varying prior formulation impacts flood mapping outcomes. We presented an improvement to the Bayesian algorithm achieved using HAND-derived prior probability. This improvement reduced false negatives around transition zones at the expense of a slight increase in FPR. Its simple input and formulation make it a viable solution for most areas globally. These findings open the path for further research on improving Bayesian algorithms by looking at the prior information, diverging from the usual non-informed priors. These findings could be applied to other Bayesian algorithms in this field.

Chapter 4 explored the potential of the exponential filter in place of the harmonic model to estimate the non-flooded probability function, which is essential in Bayesian Inference. We established that the proposed exponential filter improves the flood mapping result by reducing the FPR. This chapter also showed a novel perspective in assessing flood mapping results. We presented a time-series analysis of FPR through flooded and non-flooded scenes. In this manner, we emphasized the well-known causes for false flood labeling, e.g., frozen soils and dry conditions, and highlighted agricultural overestimation. We showed

that using the exponential filter helps to address this issue for the TU Wien algorithm. This result is rooted in the premise that the exponential filter better models the dynamic changes in the temporal backscatter signature. These insights is again useful for other flood mapping algorithms.

This chapter also raised awareness that flood mapping algorithms should be tested for non-flooding scenarios– in the context of fully automated workflows. This result implies that research on so-called automated flood mapping methods should not be overfitted only in flooded scenes. This suggested paradigm shift in assessing flood mapping methods is critical in building more suitable and robust, fully automated deployments in the future.

Overall, this thesis has firmly established that the Bayesian Inference framework is an excellent choice for flood mapping. We have shown significant improvements in the TU Wien algorithm and various paths for further improvement most of which involving manipulating data cube inputs. These key findings have directly contributed to the operation of the TU Wien algorithm for the CEMS GFM.

5.2 Outlook

Even after the conclusion of this thesis, several concepts and issues remained unresolved. These recommendations and other possible future studies stemming from this thesis are reiterated here.

A finding hinted at in Chapter 2 and further observed in Chapter 4 is the flood mapping result's dependence on the modeled standard deviation used for the no-flood reference probability distribution. We have observed that this is ultimately related to the land cover type, as areas with more diverse inter-annual change, such as agricultural fields, were observed to have higher temporal backscatter variances–often resulting in worse flood mapping performance. Compensation based on auxiliary information may be implemented to improve this result. As highlighted in Chapter 4, agricultural overestimation is a significant concern that needs further study– some algorithm refinement based on cropping practices should be studied.

Further, this standard deviation observation could also pave the way for a simplified Bayesian Inference implementation when dense data cubes are unavailable. For example, with the upcoming NASA ISRO SAR (NISAR) mission, the expectation value of no-flood references may be estimated from a handful of initial images. However, some estimation of the variance taken from Sentinel-1 data or auxiliary information may be used to have a simple solution at the onset of NISAR's operations. Needless to say the flood mapping insights gained here could be applied to other SAR missions.

Overall, gains were observed using the HAND-based prior proposed in Chapter 3. In a follow-up work [118], we tested the applicability of other openly available (near-)global HAND datasets as input to our proposed *prior function*. We found that using HAND datasets computed with improved input DEM and finer detailed stream delineations introduced more overestimation. In line with the suggestions of Refice et al., this leads us to believe that the current formulation of the HAND prior function needs to be locally tuned (e.g., based on watershed size) to get better performance. We intend to test this further in the context of a localized flood mapping algorithm in the Philippines context.

While the exponential filter method described in Chapter 4 already shows promise, an improved, fully automated version can be implemented with the automated removal of flooded images as input to the exponential filter. We look forward to the following work using the RMSD and FPR as indicators for labeling scenes as flooded or non-flooded to help in this regard.

Further improvement to the TU Wien algorithm and off-shoot methods will be explored in the near future. As the Bayesian Inference framework is flexible and adaptable, two directions are to be pursued. One involves a localized flood mapping algorithm in the Philippine context. This involves, among other things, adapting localized priors. And the other, further contribution to the globally applicable model. The foremost in this track is the improvement of the exponential filter through the automated removal of flooded input imagery.

Regardless of the work still to be done, we have established the TU Wien algorithm using the Sentinel-1 data cube as a robust method compared with other change detection algorithms. Further, we have shown improvements in the TU Wien algorithm from incremental changes to its Bayesian Inference framework. These improvements are being (and will be applied) to the TU Wien workflow under the CEMS GFM, thus impacting a true fully automated near-real-time global flood mapping operations.

Bibliography

[1] E. S. Agency. *Copernicus Sentinel-1 facilitates Australia's flood extent delineation - Copernicus Sentinel-1 facilitates Australia's flood extent delineation - Sentinel Success Stories - Sentinel Online*. URL: https://sentinel.esa.int/web/success-stories/-/copernicus-sentinel-1-facilitates-australia-s-flood-extent-delineation (Accessed 03/09/2023).

[2] A. Ajmar, P. Boccardo, M. Broglia, J. Kucera, F. Giulio-Tonolo, and A. Wania. "Response to Flood Events". en. In: *Flood Damage Survey and Assessment*. Section: 14 _eprint: https://onlinelibrary.wiley.com/doi/pdf/10.1002/9781119217930.ch14. American Geophysical Union (AGU), 2017, pp. 211–228. ISBN: 978-1-119-21793-0. DOI: 10.1002/9781119217930.ch14. URL: https://onlinelibrary.wiley.com/doi/abs/10.1002/9781119217930.ch14 (Accessed 03/27/2023).

[3] C. Albergel, C. Rüdiger, T. Pellarin, J.-C. Calvet, N. Fritz, F. Froissard, D. Suquia, A. Petitpa, B. Piguet, and E. Martin. "From near-surface to root-zone soil moisture using an exponential filter: an assessment of the method based on in-situ observations and model simulations". English. In: *Hydrology and Earth System Sciences* 12.6 (Dec. 2008). Publisher: Copernicus GmbH, pp. 1323–1337. ISSN: 1027-5606. DOI: 10.5194/hess-12-1323-2008. URL: https://hess.copernicus.org/articles/12/1323/2008/ (Accessed 07/03/2024).

[4] C. Alexandre, R. Johary, T. Catry, P. Mouquet, C. Révillion, S. Rakotondraompiana, and G. Pennober. "A Sentinel-1 based processing Chain for detection of cyclonic flood impacts". In: *Remote Sensing* 12.2 (2020). DOI: 10.3390/rs12020252.

[5] N. Baghdadi, H. Bazzi, M. El Hajj, and M. Zribi. "Detection of Frozen Soil Using Sentinel-1 SAR Data". en. In: *Remote Sensing* 10.8 (Aug. 2018). Number: 8 Publisher: Multidisciplinary Digital Publishing Institute, p. 1182. ISSN: 2072-4292. DOI: 10.3390/rs10081182. URL: https://www.mdpi.com/2072-4292/10/8/1182 (Accessed 04/18/2024).

[6] Á. Barsi, Z. Kugler, I. László, G. Szabó, and H. M. Abdulmutalib. "ACCURACY DIMENSIONS IN REMOTE SENSING". en. In: *The International Archives of the Photogrammetry, Remote Sensing and Spatial Information Sciences* XLII-3 (Apr. 2018), pp. 61–67. ISSN: 2194-9034. DOI: 10.5194/isprs-archives-XLII-3-61-2018. URL: https://www.int-arch-photogramm-remote-sens-spatial-inf-sci.net/XLII-3/61/2018/ (Accessed 02/20/2023).

[7] J. Basconcillo, A. Lucero, A. Solis, J. Robert SANDOVAL, E. Bautista, T. Koizumi, and H. Kanamaru. "Statistically Downscaled Projected Changes in Seasonal Mean Temperature and Rainfall in Cagayan Valley, Philippines". In: *Journal of the Meteorological Society of Japan. Ser. II* 94A (2016), pp. 151–164. DOI: 10.2151/jmsj.2015-058.

[8] B. Bauer-Marschallinger, S. Cao, M. E. Tupas, F. Roth, C. Navacchi, T. Melzer, V. Freeman, and W. Wagner. "Satellite-Based Flood Mapping through Bayesian Inference from a Sentinel-1 SAR Datacube". en. In: *Remote Sensing* 14.15 (Jan. 2022). Number: 15 Publisher: Multidisciplinary Digital Publishing Institute, p. 3673. ISSN: 2072-4292. DOI: 10.3390/rs14153673. URL: https://www.mdpi.com/2072-4292/14/15/3673 (Accessed 08/02/2022).

[9] B. Bauer-Marschallinger, C. Paulik, S. Hochstöger, T. Mistelbauer, S. Modanesi, L. Ciabatta, C. Massari, L. Brocca, and W. Wagner. "Soil Moisture from Fusion of Scatterometer and SAR: Closing the Scale Gap with Temporal Filtering". en. In: *Remote Sensing* 10.7 (July 2018). Number: 7 Publisher: Multidisciplinary Digital Publishing Institute, p. 1030. DOI: 10.3390/rs10071030. URL: https://www.mdpi.com/2072-4292/10/7/1030 (Accessed 01/18/2021).

[10] B. Bauer-Marschallinger, D. Sabel, and W. Wagner. "Optimisation of global grids for high-resolution remote sensing data". en. In: *Computers & Geosciences* 72 (Nov. 2014), pp. 84–93. ISSN: 0098-3004. DOI: 10.1016/j.cageo.2014.07.005. URL: http://www.sciencedirect.com/science/article/pii/S0098300414001629 (Accessed 04/02/2020).

[11] N. Bezak, P. Panagos, L. Liakos, and M. Mikoš. "Brief communication: A first hydrological investigation of extreme August 2023 floods in Slovenia, Europe". English. In: *Natural Hazards and Earth System Sciences* 23.12 (Dec. 2023). Publisher: Copernicus GmbH, pp. 3885–3893. ISSN: 1561-8633. DOI: 10.5194/nhess-23-3885-2023. URL: https://nhess.copernicus.org/articles/23/3885/2023/ (Accessed 02/11/2024).

[12] F. Bioresita, A. Puissant, A. Stumpf, and J.-P. Malet. "A method for automatic and rapid mapping of water surfaces from Sentinel-1 imagery". In: *Remote Sensing* 10.2 (2018). DOI: 10.3390/rs10020217.

[13] S. Ceola, F. Laio, and A. Montanari. "Satellite nighttime lights reveal increasing human exposure to floods worldwide". en. In: *Geophysical Research Letters* 41.20 (2014). _eprint: https://onlinelibrary.wiley.com/doi/pdf/10.1002/2014GL061859, pp. 7184–7190. ISSN: 1944-8007. DOI: 10.1002/2014GL061859. URL: https://onlinelibrary.wiley.com/doi/abs/10.1002/2014GL061859 (Accessed 03/11/2024).

[14] L. Chang, Y.-T. Chen, J.-H. Wang, and Y.-L. Chang. "Rice-Field Mapping with Sentinel-1A SAR Time-Series Data". en. In: *Remote Sensing* 13.1 (Jan. 2021). Number: 1 Publisher: Multidisciplinary Digital Publishing Institute, p. 103. ISSN: 2072-4292. DOI: 10.3390/rs13010103. URL: https://www.mdpi.com/2072-4292/13/1/103 (Accessed 06/22/2024).

[15] M. Chini, R. Hostache, L. Giustarini, and P. Matgen. "A Hierarchical Split-Based Approach for Parametric Thresholding of SAR Images: Flood Inundation as a Test Case". In: *IEEE Transactions on Geoscience and Remote Sensing* 55.12 (Dec. 2017). Conference Name: IEEE Transactions on Geoscience and Remote Sensing, pp. 6975–6988. ISSN: 1558-0644. DOI: 10.1109/TGRS.2017.2737664.

[16] C. Chow, A. Twele, and S. Martinis. "An assessment of the Height Above Nearest Drainage terrain descriptor for the thematic enhancement of automatic SAR-based flood monitoring services". In: *Remote Sensing for Agriculture, Ecosystems, and Hydrology XVIII*. Vol. 9998. SPIE, Oct. 2016, pp. 71–81. DOI: 10.1117/12.2240766. URL: https://www.spiedigitallibrary.org/conference-proceedings-of-spie/9998/999808/An-assessment-of-the-Height-Above-Nearest-Drainage-terrain-descriptor/10.1117/12.2240766.full (Accessed 08/09/2023).

[17] F. Cian, M. Marconcini, P. Ceccato, and C. Giupponi. "Flood depth estimation by means of high-resolution SAR images and lidar data". English. In: *Natural Hazards and Earth System Sciences* 18.11 (Nov. 2018). Publisher: Copernicus GmbH, pp. 3063–3084. ISSN: 1561-8633. DOI: 10.5194/nhess-18-3063-2018. URL: https://nhess.copernicus.org/articles/18/3063/2018/ (Accessed 06/29/2024).

[18] M. A. Clement, C. G. Kilsby, and P. Moore. "Multi-temporal synthetic aperture radar flood mapping using change detection". en. In: *Journal of Flood Risk Management* 11.2 (2018), pp. 152–168. ISSN: 1753-318X. DOI: https://doi.org/10.1111/jfr3.12303. URL: https://onlinelibrary.wiley.com/doi/abs/10.1111/jfr3.12303 (Accessed 02/14/2021).

[19] R. Colacicco, A. Refice, R. Nutricato, F. Bovenga, G. Caporusso, A. D'Addabbo, M. La Salandra, F. P. Lovergine, D. O. Nitti, and D. Capolongo. "High-Resolution Flood Monitoring Based on Advanced Statistical Modeling of Sentinel-1 Multi-Temporal Stacks". en. In: *Remote Sensing* 16.2 (Jan. 2024). Number: 2 Publisher: Multidisciplinary Digital Publishing Institute, p. 294. ISSN: 2072-4292. DOI: 10.3390/rs16020294. URL: https://www.mdpi.com/2072-4292/16/2/294 (Accessed 01/21/2024).

[20] R. M. de la Cruz, N. T. Olfindo Jr., M. M. Felicen, N. J. B. Borlongan, J. K. L. Difuntorum, and J. J. S. Marciano Jr. "NEAR-REALTIME FLOOD DETECTION FROM MULTI-TEMPORAL SENTINEL RADAR IMAGES USING ARTIFICIAL INTELLIGENCE". English. In: *ISPRS - International Archives of the Photogrammetry, Remote Sensing and Spatial Information Sciences*. Vol. XLIII-B3-2020. ISSN: 1682-1750. Copernicus GmbH, Aug. 2020, pp. 1663–1670. DOI: https://doi.org/10.5194/isprs-archives-XLIII-B3-2020-1663-2020. URL: https://www.int-arch-photogramm-remote-sens-spatial-inf-sci.net/XLIII-B3-2020/1663/2020/ (Accessed 10/01/2020).

[21] A. D'Addabbo, A. Refice, G. Pasquariello, F. P. Lovergine, D. Capolongo, and S. Manfreda. "A Bayesian Network for Flood Detection Combining SAR Imagery and Ancillary Data". In: *IEEE Transactions on Geoscience and Remote Sensing* 54.6 (June 2016). Conference Name: IEEE Transactions on Geoscience and Remote Sensing, pp. 3612–3625. ISSN: 1558-0644. DOI: 10.1109/TGRS.2016.2520487.

[22] R. d'Andrimont, A. Verhegghen, G. Lemoine, P. Kempeneers, M. Meroni, and M. van der Velde. "From parcel to continental scale – A first European crop type map based on Sentinel-1 and LUCAS Copernicus in-situ observations". In: *Remote Sensing of Environment* 266 (Dec. 2021), p. 112708. ISSN: 0034-4257.

DOI: 10.1016/j.rse.2021.112708. URL: https://www.sciencedirect.com/science/article/pii/S0034425721004284 (Accessed 02/23/2024).

[23] M. Dalaison and R. Jolivet. "A Kalman Filter Time Series Analysis Method for InSAR". en. In: *Journal of Geophysical Research: Solid Earth* 125.7 (2020). _eprint: https://onlinelibrary.wiley.com/doi/pdf/10.1029/2019JB019150, e2019JB019150. ISSN: 2169-9356. DOI: 10.1029/2019JB019150. URL: https://onlinelibrary.wiley.com/doi/abs/10.1029/2019JB019150 (Accessed 06/30/2024).

[24] B. DeVries, C. Huang, J. Armston, W. Huang, J. W. Jones, and M. W. Lang. "Rapid and robust monitoring of flood events using Sentinel-1 and Landsat data on the Google Earth Engine". en. In: *Remote Sensing of Environment* 240 (Apr. 2020), p. 111664. ISSN: 0034-4257. DOI: 10.1016/j.rse.2020.111664. URL: https://www.sciencedirect.com/science/article/pii/S003442572030033X (Accessed 09/22/2021).

[25] E. Dimitriou, A. Efstratiadis, I. Zotou, A. Papadopoulos, T. Iliopoulou, G.-K. Sakki, K. Mazi, E. Rozos, A. Koukouvinos, A. D. Koussis, N. Mamassis, and D. Koutsoyiannis. "Post-Analysis of Daniel Extreme Flood Event in Thessaly, Central Greece: Practical Lessons and the Value of State-of-the-Art Water-Monitoring Networks". en. In: *Water* 16.7 (Jan. 2024). Number: 7 Publisher: Multidisciplinary Digital Publishing Institute, p. 980. ISSN: 2073-4441. DOI: 10.3390/w16070980. URL: https://www.mdpi.com/2073-4441/16/7/980 (Accessed 04/24/2024).

[26] G. Donchyts, H. Winsemius, J. Schellekens, T. Erickson, H. Gao, H. Savenije, and N. van de Giesen. "Global 30m Height Above the Nearest Drainage". In: Apr. 2016. DOI: 10.13140/RG.2.1.3956.8880.

[27] ESA, B. Consult, C. G. .-. ROMANIA, T. V. Deutschland, INRA, and UCL. *Sentinel-2 Toolbox*. Oct. 2021. URL: https://step.esa.int/main/toolboxes/sentinel-2-toolbox/.

[28] E. Fahrland, P. Jacob, H. Schrader, and H. Kahabka. "Copernicus digital elevation model product handbook". In: *Airbus Defence and Space—Intelligence: Potsdam, Germany* (2020).

[29] T. G. Farr, P. A. Rosen, E. Caro, R. Crippen, R. Duren, S. Hensley, M. Kobrick, M. Paller, E. Rodriguez, L. Roth, D. Seal, S. Shaffer, J. Shimada, J. Umland, M. Werner, M. Oskin, D. Burbank, and D. Alsdorf. "The Shuttle Radar Topography Mission". en. In: *Reviews of Geophysics* 45.2 (2007). ISSN: 1944-9208. DOI: 10.1029/2005RG000183. URL: https://onlinelibrary.wiley.com/doi/abs/10.1029/2005RG000183 (Accessed 08/15/2023).

[30] F. Fichtner, N. Mandery, M. Wieland, S. Groth, S. Martinis, and T. Riedlinger. "Time-series analysis of Sentinel-1/2 data for flood detection using a discrete global grid system and seasonal decomposition". In: *International Journal of Applied Earth Observation and Geoinformation* 119 (May 2023), p. 103329. ISSN: 1569-8432. DOI: 10.1016/j.jag.2023.103329. URL: https://www.sciencedirect.com/science/article/pii/S1569843223001516 (Accessed 12/20/2023).

[31] G. M. Foody. "Explaining the unsuitability of the kappa coefficient in the assessment and comparison of the accuracy of thematic maps obtained by image classification". en. In: *Remote Sensing of Environment* 239 (Mar. 2020), p. 111630. ISSN: 0034-4257. DOI: 10.1016/j.rse.2019.111630. URL: https://www.sciencedirect.com/science/article/pii/S0034425719306509 (Accessed 05/06/2022).

[32] G. M. Foody. "Sample size determination for image classification accuracy assessment and comparison". In: *International Journal of Remote Sensing* 30.20 (Sept. 2009), pp. 5273–5291. ISSN: 0143-1161. DOI: 10.1080/01431160903130937. URL: https://doi.org/10.1080/01431160903130937 (Accessed 06/21/2022).

[33] I. Garousi-Nejad, D. G. Tarboton, M. Aboutalebi, and A. F. Torres-Rua. "Terrain Analysis Enhancements to the Height Above Nearest Drainage Flood Inundation Mapping Method". en. In: *Water Resources Research* 55.10 (2019). _eprint: https://onlinelibrary.wiley.com/doi/pdf/10.1029/2019WR024837, pp. 7983–8009. ISSN: 1944-7973. DOI: 10.1029/2019WR024837. URL: https://onlinelibrary.wiley.com/doi/abs/10.1029/2019WR024837 (Accessed 08/16/2023).

[34] L. Giustarini, R. Hostache, D. Kavetski, M. Chini, G. Corato, S. Schlaffer, and P. Matgen. "Probabilistic Flood Mapping Using Synthetic Aperture Radar Data". In: *IEEE Transactions on Geoscience and Remote Sensing* 54.12 (Dec. 2016). Conference Name: IEEE Transactions on Geoscience and Remote Sensing, pp. 6958–6969. ISSN: 1558-0644. DOI: 10.1109/TGRS.2016.2592951.

[35] L. Giustarini, R. Hostache, P. Matgen, G. J.-P. Schumann, P. D. Bates, and D. C. Mason. "A Change Detection Approach to Flood Mapping in Urban Areas Using TerraSAR-X". In: *IEEE Transactions on Geoscience and Remote Sensing* 51.4 (Apr. 2013). Conference Name: IEEE Transactions on Geoscience and Remote Sensing, pp. 2417–2430. ISSN: 1558-0644. DOI: 10.1109/TGRS.2012.2210901.

[36] L. Godbout, J. Y. Zheng, S. Dey, D. Eyelade, D. Maidment, and P. Passalacqua. "Error Assessment for Height Above the Nearest Drainage Inundation Mapping". en. In: *JAWRA Journal of the American Water Resources Association* 55.4 (2019). _eprint: https://onlinelibrary.wiley.com/doi/pdf/10.1111/1752-1688.12783, pp. 952–963. ISSN: 1752-1688. DOI: 10.1111/1752-1688.12783. URL: https://onlinelibrary.wiley.com/doi/abs/10.1111/1752-1688.12783 (Accessed 08/03/2023).

[37] N. Gorelick, M. Hancher, M. Dixon, S. Ilyushchenko, D. Thau, and R. Moore. "Google Earth Engine: Planetary-scale geospatial analysis for everyone". en. In: *Remote Sensing of Environment*. Big Remotely Sensed Data: tools, applications and experiences 202 (Dec. 2017), pp. 18–27. ISSN: 0034-4257. DOI: 10.1016/j.rse.2017.06.031. URL: https://www.sciencedirect.com/science/article/pii/S0034425717302900 (Accessed 03/01/2022).

[38] E. Graham, D. Smart, S. H. Lee, D. Harris, A. Sibley, and D. Holley. "An atmospheric river and a quasi-stationary front lead to heavy rainfall and flooding over Scotland, 6–8 October 2023". en. In: *Weather* 78.12 (2023). _eprint: https://onlinelibrary.wiley.com/doi/pdf/10.1002/wea.4501, pp. 340–343. ISSN: 1477-

8696. DOI: 10.1002/wea.4501. URL: https://onlinelibrary.wiley.com/doi/abs/10.1002/wea.4501 (Accessed 02/11/2024).

[39] S. Grimaldi, J. Xu, Y. Li, V. Pauwels, and J. Walker. "Flood mapping under vegetation using single SAR acquisitions". In: *Remote Sensing of Environment* 237 (2020). DOI: 10.1016/j.rse.2019.111582.

[40] V. Gstaiger, J. Huth, S. Gebhardt, T. Wehrmann, and C. Kuenzer. "Multi-sensoral and automated derivation of inundated areas using TerraSAR-X and ENVISAT ASAR data". In: *International Journal of Remote Sensing* 33.22 (Nov. 2012). Publisher: Taylor & Francis _eprint: https://doi.org/10.1080/01431161.2012.700421, pp. 7291–7304. ISSN: 0143-1161. DOI: 10.1080/01431161.2012.700421. URL: https://doi.org/10.1080/01431161.2012.700421 (Accessed 02/14/2021).

[41] M. A. Gutierrez, N. M. Paguirigan, J. Raviz, M. R. Mabalay, E. Alosnos, L. Villano, S. Asilo, A. Arocena Jr., J. Maloom, and A. Laborte. "THE RICE PLANTING WINDOW IN THE PHILIPPINES: AN ANALYSIS USING MULTI-TEMPORAL SAR IMAGERY". en. In: *The International Archives of the Photogrammetry, Remote Sensing and Spatial Information Sciences* XLII-4/W19 (Dec. 2019), pp. 241–248. ISSN: 2194-9034. DOI: 10.5194/isprs-archives-XLII-4-W19-241-2019. URL: https://www.int-arch-photogramm-remote-sens-spatial-inf-sci.net/XLII-4-W19/241/2019/ (Accessed 03/15/2023).

[42] K. Harfenmeister, D. Spengler, and C. Weltzien. "Analyzing Temporal and Spatial Characteristics of Crop Parameters Using Sentinel-1 Backscatter Data". en. In: *Remote Sensing* 11.13 (Jan. 2019). Number: 13 Publisher: Multidisciplinary Digital Publishing Institute, p. 1569. ISSN: 2072-4292. DOI: 10.3390/rs11131569. URL: https://www.mdpi.com/2072-4292/11/13/1569 (Accessed 06/21/2024).

[43] J. He, Q. Li, P.-W. Chan, C.-W. Choy, B. Mak, C.-C. Lam, and H.-Y. Luo. "An Observational Study of Typhoon Talim over the Northern Part of the South China Sea in July 2023". en. In: *Atmosphere* 14.9 (Sept. 2023). Number: 9 Publisher: Multidisciplinary Digital Publishing Institute, p. 1340. ISSN: 2073-4433. DOI: 10.3390/atmos14091340. URL: https://www.mdpi.com/2073-4433/14/9/1340 (Accessed 04/12/2024).

[44] K. He, Q. Yang, X. Shen, E. Dimitriou, A. Mentzafou, C. Papadaki, M. Stoumboudi, and E. N. Anagnostou. "Brief communication: Storm Daniel Flood Impact in Greece 2023: Mapping Crop and Livestock Exposure from SAR". English. In: *Natural Hazards and Earth System Sciences Discussions* (Oct. 2023). Publisher: Copernicus GmbH, pp. 1–16. DOI: 10.5194/nhess-2023-173. URL: https://nhess.copernicus.org/preprints/nhess-2023-173/ (Accessed 02/11/2024).

[45] Y. Hirabayashi, R. Mahendran, S. Koirala, L. Konoshima, D. Yamazaki, S. Watanabe, H. Kim, and S. Kanae. "Global flood risk under climate change". en. In: *Nature Climate Change* 3.9 (Sept. 2013). Number: 9 Publisher: Nature Publishing Group, pp. 816–821. ISSN: 1758-6798. DOI: 10.1038/nclimate1911. URL: https://www.nature.com/articles/nclimate1911 (Accessed 02/15/2021).

[46] M. S. Horritt, D. C. Mason, D. M. Cobby, I. J. Davenport, and P. D. Bates. "Waterline mapping in flooded vegetation from airborne SAR imagery". In: *Remote Sensing of Environment* 85.3 (May 2003), pp. 271–281. ISSN: 0034-4257. DOI: 10.1016/S0034-4257(03)00006-3. URL: https://www.sciencedirect.com/science/article/pii/S0034425703000063 (Accessed 08/24/2023).

[47] R. Hostache, P. Matgen, and W. Wagner. "Change detection approaches for flood extent mapping: How to select the most adequate reference image from online archives?" en. In: *International Journal of Applied Earth Observation and Geoinformation* 19 (Oct. 2012), pp. 205–213. ISSN: 0303-2434. DOI: 10.1016/j.jag.2012.05.003. URL: http://www.sciencedirect.com/science/article/pii/S0303243412000992 (Accessed 11/14/2020).

[48] C. Huang, B. D. Nguyen, S. Zhang, S. Cao, and W. Wagner. "A Comparison of Terrain Indices toward Their Ability in Assisting Surface Water Mapping from Sentinel-1 Data". en. In: *ISPRS International Journal of Geo-Information* 6.5 (May 2017). Number: 5 Publisher: Multidisciplinary Digital Publishing Institute, p. 140. ISSN: 2220-9964. DOI: 10.3390/ijgi6050140. URL: https://www.mdpi.com/2220-9964/6/5/140 (Accessed 07/31/2023).

[49] K. Jafarzadegan and V. Merwade. "Probabilistic floodplain mapping using HAND-based statistical approach". en. In: *Geomorphology* 324 (Jan. 2019), pp. 48–61. ISSN: 0169-555X. DOI: 10.1016/j.geomorph.2018.09.024. URL: https://www.sciencedirect.com/science/article/pii/S0169555X18303891 (Accessed 08/02/2023).

[50] I. Joubert-Boitat, A. Wania, and S. Dalmasso. *Manual for CEMS-Rapid Mapping Products*. en. ISBN: 9789276216834 ISSN: 1831-9424. Sept. 2020. DOI: 10.2760/29876. URL: https://publications.jrc.ec.europa.eu/repository/handle/JRC121741 (Accessed 11/19/2023).

[51] K. Kaku. "Satellite remote sensing for disaster management support: A holistic and staged approach based on case studies in Sentinel Asia". en. In: *International Journal of Disaster Risk Reduction* 33 (Feb. 2019), pp. 417–432. ISSN: 2212-4209. DOI: 10.1016/j.ijdrr.2018.09.015. URL: https://www.sciencedirect.com/science/article/pii/S2212420918304801 (Accessed 02/12/2021).

[52] K. Karamvasis and V. Karathanassi. "FLOMPY: An Open-Source Toolbox for Floodwater Mapping Using Sentinel-1 Intensity Time Series". en. In: *Water* 13.21 (Jan. 2021). Number: 21 Publisher: Multidisciplinary Digital Publishing Institute, p. 2943. ISSN: 2073-4441. DOI: 10.3390/w13212943. URL: https://www.mdpi.com/2073-4441/13/21/2943 (Accessed 03/14/2024).

[53] V. Katiyar, N. Tamkuan, and M. Nagai. "Near-Real-Time Flood Mapping Using Off-the-Shelf Models with SAR Imagery and Deep Learning". en. In: *Remote Sensing* 13.12 (Jan. 2021). Number: 12 Publisher: Multidisciplinary Digital Publishing Institute, p. 2334. ISSN: 2072-4292. DOI: 10.3390/rs13122334. URL: https://www.mdpi.com/2072-4292/13/12/2334 (Accessed 09/13/2024).

[54] J. Kittler and J. Illingworth. "Minimum error thresholding". en. In: *Pattern Recognition* 19.1 (Jan. 1986), pp. 41–47. ISSN: 0031-3203. DOI: 10.1016/0031-3203(86)90030-0. URL: https://www.sciencedirect.com/science/article/pii/0031320386900300 (Accessed 03/23/2022).

[55] V. Komisarenko, K. Voormansik, R. Elshawi, and S. Sakr. "Exploiting time series of Sentinel-1 and Sentinel-2 to detect grassland mowing events using deep learning with reject region". en. In: *Scientific Reports* 12.1 (Jan. 2022). Publisher: Nature Publishing Group, p. 983. ISSN: 2045-2322. DOI: 10.1038/s41598-022-04932-6. URL: https://www.nature.com/articles/s41598-022-04932-6 (Accessed 06/30/2024).

[56] L. Landuyt, A. V. Wesemael, G. J. Schumann, R. Hostache, N. E. C. Verhoest, and F. M. B. V. Coillie. "Flood Mapping Based on Synthetic Aperture Radar: An Assessment of Established Approaches". In: *IEEE Transactions on Geoscience and Remote Sensing* 57.2 (Feb. 2019). Conference Name: IEEE Transactions on Geoscience and Remote Sensing, pp. 722–739. ISSN: 1558-0644. DOI: 10.1109/TGRS.2018.2860054.

[57] J.-S. Lee. "Digital image smoothing and the sigma filter". In: *Computer Vision, Graphics, and Image Processing* 24.2 (Nov. 1983), pp. 255–269. ISSN: 0734-189X. DOI: 10.1016/0734-189X(83)90047-6. URL: https://www.sciencedirect.com/science/article/pii/0734189X83900476 (Accessed 03/12/2024).

[58] J.-S. Lee, J.-H. Wen, T. Ainsworth, K.-S. Chen, and A. Chen. "Improved Sigma Filter for Speckle Filtering of SAR Imagery". In: *IEEE Transactions on Geoscience and Remote Sensing* 47.1 (Jan. 2009). Conference Name: IEEE Transactions on Geoscience and Remote Sensing, pp. 202–213. ISSN: 1558-0644. DOI: 10.1109/TGRS.2008.2002881. URL: https://ieeexplore.ieee.org/document/4689358 (Accessed 03/12/2024).

[59] Y. Li, H. Fu, J. Zhu, K. Wu, P. Yang, L. Wang, and S. Gao. "A Method for SRTM DEM Elevation Error Correction in Forested Areas Using ICESat-2 Data and Vegetation Classification Data". en. In: *Remote Sensing* 14.14 (Jan. 2022). Number: 14 Publisher: Multidisciplinary Digital Publishing Institute, p. 3380. ISSN: 2072-4292. DOI: 10.3390/rs14143380. URL: https://www.mdpi.com/2072-4292/14/14/3380 (Accessed 08/22/2023).

[60] Y. Li, S. Martinis, S. Plank, and R. Ludwig. "An automatic change detection approach for rapid flood mapping in Sentinel-1 SAR data". en. In: *International Journal of Applied Earth Observation and Geoinformation* 73 (Dec. 2018), pp. 123–135. ISSN: 0303-2434. DOI: 10.1016/j.jag.2018.05.023. URL: https://www.sciencedirect.com/science/article/pii/S0303243418302782 (Accessed 03/08/2021).

[61] Y. Li, S. Martinis, and M. Wieland. "Urban flood mapping with an active self-learning convolutional neural network based on TerraSAR-X intensity and interferometric coherence". en. In: *ISPRS Journal of Photogrammetry and Remote Sensing* 152 (June 2019), pp. 178–191. ISSN: 0924-2716. DOI: 10.1016/j.isprsjprs.

2019.04.014. URL: https://www.sciencedirect.com/science/article/pii/S092427161930111X (Accessed 02/06/2021).

[62] Z. Li and I. Demir. "U-net-based semantic classification for flood extent extraction using SAR imagery and GEE platform: A case study for 2019 central US flooding". en. In: *Science of The Total Environment* 869 (Apr. 2023), p. 161757. ISSN: 0048-9697. DOI: 10.1016/j.scitotenv.2023.161757. URL: https://www.sciencedirect.com/science/article/pii/S0048969723003728 (Accessed 02/14/2023).

[63] Z. Li, F. Q. Duque, T. Grout, B. Bates, and I. Demir. "Comparative analysis of performance and mechanisms of flood inundation map generation using Height Above Nearest Drainage". In: *Environmental Modelling & Software* 159 (Jan. 2023), p. 105565. ISSN: 1364-8152. DOI: 10.1016/j.envsoft.2022.105565. URL: https://www.sciencedirect.com/science/article/pii/S1364815222002651 (Accessed 08/22/2023).

[64] J. Liang and D. Liu. "A local thresholding approach to flood water delineation using Sentinel-1 SAR imagery". In: *ISPRS Journal of Photogrammetry and Remote Sensing* 159 (Jan. 2020), pp. 53–62. ISSN: 0924-2716. DOI: 10.1016/j.isprsjprs.2019.10.017. URL: https://www.sciencedirect.com/science/article/pii/S0924271619302540 (Accessed 11/07/2023).

[65] Y. Lin, S.-H. Yun, A. Bhardwaj, and E. Hill. "Urban flood detection with Sentinel-1Multi-Temporal Synthetic Aperture Radar (SAR) observations in a Bayesian framework: A case study for Hurricane Matthew". In: *Remote Sensing* 11.15 (2019). DOI: 10.3390/rs11151778.

[66] C. Liu, P. Frazier, and L. Kumar. "Comparative assessment of the measures of thematic classification accuracy". en. In: *Remote Sensing of Environment* 107.4 (Apr. 2007), pp. 606–616. ISSN: 0034-4257. DOI: 10.1016/j.rse.2006.10.010. URL: https://www.sciencedirect.com/science/article/pii/S0034425706004068 (Accessed 06/28/2022).

[67] M. R. Mabalay, J. Raviz, E. Alosnos, M. Barbieri, E. Quicho, J. E. A. Bibar, M. Barroga, M. Coñado, P. Mabalot, J. R. Mirandilla, A. Arocena, J. Maloom, G. Bello, E. Cariño, G. de Mesa, N. Detoito, H. Gonzaga, N. Martin, M. P. Tejada, M. J. Vives, M. Lastimoso, D. K. Bumagat, H. Cayaban, M. Barroga, R. Bayot, A. M. Callejo, N. M. Paguirigan, M. A. Gutierrez, G. C. Romuga, F. G. Amanquiton, J. Gan, E. P. Banasihan, C. C. Guevarra, A. Rala, H. Yonson, M. Malonzo, G. B. Berja, C. Diaz, L. A. Tamani, R. G. Roces, S. Asilo, J. de Dios, T. D. Setiyono, F. Holecz, E. J. Quilang, and A. Laborte. "The Philippine Rice Information System (PRiSM)Philippine Rice Information System (PRISM): An Operational Monitoring-Monitoring and Information System on RiceRicePhilippine Rice Information System (PRISM)Monitoring". en. In: *Remote Sensing of Agriculture and Land Cover/Land Use Changes in South and Southeast Asian Countries*. Ed. by K. P. Vadrevu, T. Le Toan, S. S. Ray, and C. Justice. Cham: Springer International Publishing, 2022, pp. 133–150. ISBN: 978-3-030-92365-5. DOI: 10.1007/978-3-030-92365-5_7. URL: https://doi.org/10.1007/978-3-030-92365-5_7 (Accessed 03/25/2024).

[68] S. Maity, C. Patnaik, M. Chakraborty, and S. Panigrahy. "Analysis of temporal backscattering of cotton crops using a semiempirical model". In: *IEEE Transactions on Geoscience and Remote Sensing* 42.3 (Mar. 2004). Conference Name: IEEE Transactions on Geoscience and Remote Sensing, pp. 577–587. ISSN: 1558-0644. DOI: 10.1109/TGRS.2003.821888. URL: https://ieeexplore.ieee.org/abstract/document/1273589 (Accessed 03/12/2024).

[69] K. N. Markert, A. M. Markert, T. Mayer, C. Nauman, A. Haag, A. Poortinga, B. Bhandari, N. S. Thwal, T. Kunlamai, F. Chishtie, M. Kwant, K. Phongsapan, N. Clinton, P. Towashiraporn, and D. Saah. "Comparing Sentinel-1 Surface Water Mapping Algorithms and Radiometric Terrain Correction Processing in Southeast Asia Utilizing Google Earth Engine". en. In: *Remote Sensing* 12.15 (Jan. 2020). Number: 15 Publisher: Multidisciplinary Digital Publishing Institute, p. 2469. ISSN: 2072-4292. DOI: 10.3390/rs12152469. URL: https://www.mdpi.com/2072-4292/12/15/2469 (Accessed 09/14/2022).

[70] S. Martinis, S. Plank, and K. Ćwik. "The use of Sentinel-1 time-series data to improve flood monitoring in arid areas". In: *Remote Sensing* 10.4 (2018). DOI: 10.3390/rs10040583.

[71] S. Martinis, A. Twele, and S. Voigt. "Towards operational near real-time flood detection using a split-based automatic thresholding procedure on high resolution TerraSAR-X data". English. In: *Natural Hazards and Earth System Sciences* 9.2 (Mar. 2009). Publisher: Copernicus GmbH, pp. 303–314. ISSN: 1561-8633. DOI: 10.5194/nhess-9-303-2009. URL: https://nhess.copernicus.org/articles/9/303/2009/ (Accessed 09/13/2024).

[72] S. Martinis, J. Kersten, and A. Twele. "A fully automated TerraSAR-X based flood service". en. In: *ISPRS Journal of Photogrammetry and Remote Sensing* 104 (June 2015), pp. 203–212. ISSN: 0924-2716. DOI: 10.1016/j.isprsjprs.2014.07.014. URL: https://www.sciencedirect.com/science/article/pii/S0924271614001981 (Accessed 02/14/2021).

[73] S. Martinis, C. Kuenzer, A. Wendleder, J. Huth, A. Twele, A. Roth, and S. Dech. "Comparing four operational SAR-based water and flood detection approaches". In: *International Journal of Remote Sensing* 36.13 (July 2015). Publisher: Taylor & Francis _eprint: https://doi.org/10.1080/01431161.2015.1060647, pp. 3519–3543. ISSN: 0143-1161. DOI: 10.1080/01431161.2015.1060647. URL: https://doi.org/10.1080/01431161.2015.1060647 (Accessed 02/14/2021).

[74] P. Matgen, M. Chini, B. Bauer-Marschallinger, F. Roth, C. Krullikowski, C. W.-Y. Chow, M. Wieland, S. Martinis, W. Wagner, P. Salamon, S. Cao, R. Hostache, Y. Li, L. Molini, and M. Seewald. *Provision of an Automated, Global, Satellite-based Flood Monitoring Product for the Copernicus Emergency Management Service: Product Definition Document (PDD)*. Monograph. Num Pages: 75. Apr. 2022. URL: https://extwiki.eodc.eu/GFM/PDD (Accessed 03/12/2024).

[75] T. Mayer, A. Poortinga, B. Bhandari, A. P. Nicolau, K. Markert, N. S. Thwal, A. Markert, A. Haag, J. Kilbride, F. Chishtie, A. Wadhwa, N. Clinton, and D. Saah. "Deep learning approach for Sentinel-1 surface water mapping leveraging Google Earth Engine". en. In: *ISPRS Open Journal of Photogrammetry and Remote Sensing* 2 (Dec. 2021), p. 100005. ISSN: 2667-3932. DOI: 10.1016/j.ophoto.2021.100005. URL: https://www.sciencedirect.com/science/article/pii/S2667393221000053 (Accessed 10/23/2021).

[76] M. J. Metzger. *The Global Environmental Stratification: A high-resolution bioclimate map of the world*. eng. Accepted: 2018-05-28T16:57:36Z Journal Abbreviation: GEnS Publication Title: Metzger M.J., Bunce R.G.H, Jongman R.H.G, Sayre R., Trabucco A., Zomer R. (2013). A high-resolution bioclimate map of the world: a unifying framework for global biodiversity research and monitoring. Global Ecology and Biogeography 22: 630-638. May 2018. DOI: 10.7488/ds/2354. URL: https://datashare.ed.ac.uk/handle/10283/3089 (Accessed 03/21/2024).

[77] D. Misev, P. Baumann, D. Bellos, and S. Wiehle. "BigDataCube: A Scalable, Federated Service Platform for Copernicus". English. In: 2019, pp. 4103–4112. ISBN: 978-1-72810-858-2. DOI: 10.1109/BigData47090.2019.9006222.

[78] J. Muñoz-Sabater, E. Dutra, A. Agustí-Panareda, C. Albergel, G. Arduini, G. Balsamo, S. Boussetta, M. Choulga, S. Harrigan, H. Hersbach, B. Martens, D. G. Miralles, M. Piles, N. J. Rodríguez-Fernández, E. Zsoter, C. Buontempo, and J.-N. Thépaut. "ERA5-Land: a state-of-the-art global reanalysis dataset for land applications". English. In: *Earth System Science Data* 13.9 (Sept. 2021). Publisher: Copernicus GmbH, pp. 4349–4383. ISSN: 1866-3508. DOI: 10.5194/essd-13-4349-2021. URL: https://essd.copernicus.org/articles/13/4349/2021/ (Accessed 03/13/2024).

[79] T. Nadine, C. Stephen, L. Lucia, M. Jérôme, B. Stéphanie, and Y. Hervé. "Exploitation of Sentinel-1 Data for Flood Mapping and Monitoring within the Framework of the Copernicus Emergency Core and Downstream Services". In: *IGARSS 2019 - 2019 IEEE International Geoscience and Remote Sensing Symposium*. ISSN: 2153-7003. July 2019, pp. 5393–5396. DOI: 10.1109/IGARSS.2019.8899324.

[80] H. Nagai, T. Abe, and M. Ohki. "SAR-Based Flood Monitoring for Flatland with Frequently Fluctuating Water Surfaces: Proposal for the Normalized Backscatter Amplitude Difference Index (NoBADI)". en. In: *Remote Sensing* 13.20 (Jan. 2021). Number: 20 Publisher: Multidisciplinary Digital Publishing Institute, p. 4136. ISSN: 2072-4292. DOI: 10.3390/rs13204136. URL: https://www.mdpi.com/2072-4292/13/20/4136 (Accessed 02/10/2022).

[81] C. Navacchi and B. Bauer-Marschallinger. *TUW-GEO/yeoda: v0.1.4*. Jan. 2020. DOI: 10.5281/zenodo.3622776. URL: https://zenodo.org/record/3622776 (Accessed 09/15/2020).

[82] A. D. Nobre, L. A. Cuartas, M. Hodnett, C. D. Rennó, G. Rodrigues, A. Silveira, M. Waterloo, and S. Saleska. "Height Above the Nearest Drainage – a hydrologically relevant new terrain model". en. In: *Journal of Hydrology* 404.1 (June 2011), pp. 13–29. ISSN: 0022-1694. DOI: 10.1016/j.jhydrol.2011.03.051. URL: http://

www.sciencedirect.com/science/article/pii/S0022169411002599 (Accessed 06/24/2020).

[83] D. O'Grady, M. Leblanc, and D. Gillieson. "Use of ENVISAT ASAR Global Monitoring Mode to complement optical data in the mapping of rapid broad-scale flooding in Pakistan". English. In: *Hydrology and Earth System Sciences* 15.11 (Nov. 2011). Publisher: Copernicus GmbH, pp. 3475–3494. ISSN: 1027-5606. DOI: 10.5194/hess-15-3475-2011. URL: https://hess.copernicus.org/articles/15/3475/2011/ (Accessed 06/29/2024).

[84] N. Otsu. "A Threshold Selection Method from Gray-Level Histograms". In: *IEEE Transactions on Systems, Man, and Cybernetics* 9.1 (Jan. 1979). Conference Name: IEEE Transactions on Systems, Man, and Cybernetics, pp. 62–66. ISSN: 2168-2909. DOI: 10.1109/TSMC.1979.4310076.

[85] C. Paulik, W. Dorigo, W. Wagner, and R. Kidd. "Validation of the ASCAT Soil Water Index using in situ data from the International Soil Moisture Network". In: *International Journal of Applied Earth Observation and Geoinformation* 30 (Aug. 2014), pp. 1–8. ISSN: 1569-8432. DOI: 10.1016/j.jag.2014.01.007. URL: https://www.sciencedirect.com/science/article/pii/S0303243414000099 (Accessed 04/14/2024).

[86] R. Pelich, M. Chini, R. Hostache, P. Matgen, L. Pulvirenti, and N. Pierdicca. "Mapping Floods in Urban Areas from Dual-Polarization InSAR Coherence Data". English. In: *IEEE Geoscience and Remote Sensing Letters* 19 (2022). ISSN: 1545-598X. DOI: 10.1109/LGRS.2021.3110132.

[87] R. Pelich, M. Chini, R. Hostache, P. Matgen, J. M. Delgado, and G. Sabatino. "Towards a global flood frequency map from SAR data". In: *2017 IEEE International Geoscience and Remote Sensing Symposium (IGARSS)*. ISSN: 2153-7003. July 2017, pp. 4024–4027. DOI: 10.1109/IGARSS.2017.8127883.

[88] T. Pellarin, J.-C. Calvet, and W. Wagner. "Evaluation of ERS scatterometer soil moisture products over a half-degree region in southwestern France". en. In: *Geophysical Research Letters* 33.17 (2006). ISSN: 1944-8007. DOI: 10.1029/2006GL027231. URL: https://onlinelibrary.wiley.com/doi/abs/10.1029/2006GL027231 (Accessed 03/12/2024).

[89] J. W. Pratt. "Remarks on Zeros and Ties in the Wilcoxon Signed Rank Procedures". In: *Journal of the American Statistical Association* 54.287 (Sept. 1959), pp. 655–667. ISSN: 0162-1459. DOI: 10.1080/01621459.1959.10501526. URL: https://www.tandfonline.com/doi/abs/10.1080/01621459.1959.10501526 (Accessed 06/30/2024).

[90] L. Pulvirenti, N. Pierdicca, M. Chini, and L. Guerriero. "An algorithm for operational flood mapping from Synthetic Aperture Radar (SAR) data using fuzzy logic". English. In: *Natural Hazards and Earth System Sciences* 11.2 (Feb. 2011). Publisher: Copernicus GmbH, pp. 529–540. ISSN: 1561-8633. DOI: https://doi.org/10.5194/nhess-11-529-2011. URL: https://nhess.copernicus.org/articles/11/529/2011/ (Accessed 02/16/2021).

[91] B. Rabus, M. Eineder, A. Roth, and R. Bamler. "The shuttle radar topography mission—a new class of digital elevation models acquired by spaceborne radar". In: *ISPRS Journal of Photogrammetry and Remote Sensing* 57.4 (Feb. 2003), pp. 241–262. ISSN: 0924-2716. DOI: 10.1016/S0924-2716(02)00124-7. URL: https://www.sciencedirect.com/science/article/pii/S0924271602001247 (Accessed 08/22/2023).

[92] M. Rättich, S. Martinis, and M. Wieland. "Automatic Flood Duration Estimation Based on Multi-Sensor Satellite Data". en. In: *Remote Sensing* 12.4 (Jan. 2020). Number: 4 Publisher: Multidisciplinary Digital Publishing Institute, p. 643. ISSN: 2072-4292. DOI: 10.3390/rs12040643. URL: https://www.mdpi.com/2072-4292/12/4/643 (Accessed 06/22/2024).

[93] A. Refice, A. D'Addabbo, F. Lovergine, F. Bovenga, R. Nutricato, and D. Nitti. "Improving Flood Monitoring Through Advanced Modeling of Sentinel-1 Multi-Temporal Stacks". In: *IGARSS 2022 - 2022 IEEE International Geoscience and Remote Sensing Symposium*. ISSN: 2153-7003. July 2022, pp. 5881–5884. DOI: 10.1109/IGARSS46834.2022.9883943. URL: https://ieeexplore.ieee.org/document/9883943/references#references (Accessed 01/22/2024).

[94] A. Refice, D. Capolongo, G. Pasquariello, A. D'Addabbo, F. Bovenga, R. Nutricato, F. P. Lovergine, and L. Pietranera. "SAR and InSAR for Flood Monitoring: Examples With COSMO-SkyMed Data". In: *IEEE Journal of Selected Topics in Applied Earth Observations and Remote Sensing* 7.7 (July 2014). Conference Name: IEEE Journal of Selected Topics in Applied Earth Observations and Remote Sensing, pp. 2711–2722. ISSN: 2151-1535. DOI: 10.1109/JSTARS.2014.2305165.

[95] C. D. Rennó, A. D. Nobre, L. A. Cuartas, J. V. Soares, M. G. Hodnett, J. Tomasella, and M. J. Waterloo. "HAND, a new terrain descriptor using SRTM-DEM: Mapping terra-firme rainforest environments in Amazonia". In: *Remote Sensing of Environment* 112.9 (Sept. 2008), pp. 3469–3481. ISSN: 0034-4257. DOI: 10.1016/j.rse.2008.03.018. URL: https://www.sciencedirect.com/science/article/pii/S003442570800120X (Accessed 08/22/2023).

[96] J. Rentschler, M. Salhab, and B. A. Jafino. "Flood exposure and poverty in 188 countries". en. In: *Nature Communications* 13.1 (June 2022). Publisher: Nature Publishing Group, p. 3527. ISSN: 2041-1723. DOI: 10.1038/s41467-022-30727-4. URL: https://www.nature.com/articles/s41467-022-30727-4 (Accessed 06/17/2024).

[97] F. Roth, B. Bauer-Marschallinger, M. E. Tupas, C. Reimer, P. Salamon, and W. Wagner. "Sentinel-1-based analysis of the severe flood over Pakistan 2022". English. In: *Natural Hazards and Earth System Sciences* 23.10 (Oct. 2023). Publisher: Copernicus GmbH, pp. 3305–3317. ISSN: 1561-8633. DOI: 10.5194/nhess-23-3305-2023. URL: https://nhess.copernicus.org/articles/23/3305/2023/ (Accessed 10/26/2023).

[98] P. Salamon, N. Mctlormick, C. Reimer, T. Clarke, B. Bauer-Marschallinger, W. Wagner, S. Martinis, C. Chow, C. Böhnke, P. Matgen, M. Chini, R. Hostache, L. Molini, E. Fiori, and A. Walli. "The New, Systematic Global Flood Monitoring Product of the Copernicus Emergency Management Service". In: *2021 IEEE International Geoscience and Remote Sensing Symposium IGARSS*. ISSN: 2153-7003. July 2021, pp. 1053–1056. DOI: 10.1109/IGARSS47720.2021.9554214.

[99] G. D. C. Santos. "2020 tropical cyclones in the Philippines: A review". en. In: *Tropical Cyclone Research and Review* 10.3 (Sept. 2021), pp. 191–199. ISSN: 2225-6032. DOI: 10.1016/j.tcrr.2021.09.003. URL: https://www.sciencedirect.com/science/article/pii/S2225603221000278 (Accessed 04/30/2022).

[100] S. Schlaffer, M. Chini, L. Giustarini, and P. Matgen. "Probabilistic mapping of flood-induced backscatter changes in SAR time series". en. In: *International Journal of Applied Earth Observation and Geoinformation* 56 (Apr. 2017), pp. 77–87. ISSN: 0303-2434. DOI: 10.1016/j.jag.2016.12.003. URL: https://www.sciencedirect.com/science/article/pii/S0303243416301994 (Accessed 02/14/2021).

[101] S. Schlaffer, P. Matgen, M. Hollaus, and W. Wagner. "Flood detection from multi-temporal SAR data using harmonic analysis and change detection". en. In: *International Journal of Applied Earth Observation and Geoinformation* 38 (June 2015), pp. 15–24. ISSN: 0303-2434. DOI: 10.1016/j.jag.2014.12.001. URL: http://www.sciencedirect.com/science/article/pii/S0303243414002645 (Accessed 03/20/2020).

[102] G. Schumann, L. Giustarini, A. Tarpanelli, B. Jarihani, and S. Martinis. "Flood Modeling and Prediction Using Earth Observation Data". en. In: *Surveys in Geophysics* 44.5 (Oct. 2023), pp. 1553–1578. ISSN: 1573-0956. DOI: 10.1007/s10712-022-09751-y. URL: https://doi.org/10.1007/s10712-022-09751-y (Accessed 10/18/2023).

[103] G. J. .-. Schumann and D. K. Moller. "Microwave remote sensing of flood inundation". en. In: *Physics and Chemistry of the Earth, Parts A/B/C*. Emerging science and applications with microwave remote sensing data 83-84 (Jan. 2015), pp. 84–95. ISSN: 1474-7065. DOI: 10.1016/j.pce.2015.05.002. URL: https://www.sciencedirect.com/science/article/pii/S1474706515000406 (Accessed 02/14/2021).

[104] X. Shen, D. Wang, K. Mao, E. Anagnostou, and Y. Hong. "Inundation extent mapping by synthetic aperture radar: A review". In: *Remote Sensing* 11.7 (2019). DOI: 10.3390/RS11070879.

[105] X. Shen, E. N. Anagnostou, G. H. Allen, G. Robert Brakenridge, and A. J. Kettner. "Near-real-time non-obstructed flood inundation mapping using synthetic aperture radar". en. In: *Remote Sensing of Environment* 221 (Feb. 2019), pp. 302–315. ISSN: 0034-4257. DOI: 10.1016/j.rse.2018.11.008. URL: https://www.sciencedirect.com/science/article/pii/S0034425718305169 (Accessed 03/21/2021).

[106] S. F. Sherpa, M. Shirzaei, C. Ojha, S. Werth, and R. Hostache. "Probabilistic Mapping of August 2018 Flood of Kerala, India, Using Space-Borne Synthetic Aperture Radar". In: *IEEE Journal of Selected Topics in Applied Earth Observations and Remote Sensing* 13 (2020). Conference Name: IEEE Journal of Selected Topics in Applied Earth Observations and Remote Sensing, pp. 896–913. ISSN: 2151-1535. DOI: 10.1109/JSTARS.2020.2970337.

[107] E. Stephens, G. Schumann, and P. Bates. "Problems with binary pattern measures for flood model evaluation". en. In: *Hydrological Processes* 28.18 (2014), pp. 4928–4937. ISSN: 1099-1085. DOI: 10.1002/hyp.9979. URL: https://onlinelibrary.wiley.com/doi/abs/10.1002/hyp.9979 (Accessed 10/20/2022).

[108] L. Tarasova, D. Lun, R. Merz, G. Blöschl, S. Basso, M. Bertola, A. Miniussi, O. Rakovec, L. Samaniego, S. Thober, and R. Kumar. "Shifts in flood generation processes exacerbate regional flood anomalies in Europe". en. In: *Communications Earth & Environment* 4.1 (Feb. 2023). Number: 1 Publisher: Nature Publishing Group, pp. 1–12. ISSN: 2662-4435. DOI: 10.1038/s43247-023-00714-8. URL: https://www.nature.com/articles/s43247-023-00714-8 (Accessed 02/11/2024).

[109] A. Tarpanelli, A. C. Mondini, and S. Camici. "Effectiveness of Sentinel-1 and Sentinel-2 for flood detection assessment in Europe". English. In: *Natural Hazards and Earth System Sciences* 22.8 (Aug. 2022). Publisher: Copernicus GmbH, pp. 2473–2489. ISSN: 1561-8633. DOI: 10.5194/nhess-22-2473-2022. URL: https://nhess.copernicus.org/articles/22/2473/2022/ (Accessed 10/23/2023).

[110] B. Tellman, J. A. Sullivan, C. Kuhn, A. J. Kettner, C. S. Doyle, G. R. Brakenridge, T. A. Erickson, and D. A. Slayback. "Satellite imaging reveals increased proportion of population exposed to floods". en. In: *Nature* 596.7870 (Aug. 2021), pp. 80–86. ISSN: 1476-4687. DOI: 10.1038/s41586-021-03695-w. URL: https://www.nature.com/articles/s41586-021-03695-w (Accessed 08/09/2021).

[111] C. Ticehurst, Z.-S. Zhou, E. Lehmann, F. Yuan, M. Thankappan, A. Rosenqvist, B. Lewis, and M. Paget. "Building a SAR-Enabled Data Cube Capability in Australia Using SAR Analysis Ready Data". en. In: *Data* 4.3 (Sept. 2019). Number: 3 Publisher: Multidisciplinary Digital Publishing Institute, p. 100. ISSN: 2306-5729. DOI: 10.3390/data4030100. URL: https://www.mdpi.com/2306-5729/4/3/100 (Accessed 04/29/2022).

[112] P. L. M. Tolentino, A. Poortinga, H. Kanamaru, S. Keesstra, J. Maroulis, C. P. C. David, and C. J. Ritsema. "Projected Impact of Climate Change on Hydrological Regimes in the Philippines". en. In: *PLOS ONE* 11.10 (Oct. 2016). Publisher: Public Library of Science, e0163941. ISSN: 1932-6203. DOI: 10.1371/journal.pone.0163941. URL: https://journals.plos.org/plosone/article?id=10.1371/journal.pone.0163941 (Accessed 10/01/2020).

[113] R. Torres, P. Snoeij, D. Geudtner, D. Bibby, M. Davidson, E. Attema, P. Potin, B. Rommen, N. Floury, M. Brown, I. N. Traver, P. Deghaye, B. Duesmann, B. Rosich, N. Miranda, C. Bruno, M. L'Abbate, R. Croci, A. Pietropaolo, M. Huchler, and F. Rostan. "GMES Sentinel-1 mission". In: *Remote Sensing of Environ-*

ment. The Sentinel Missions - New Opportunities for Science 120 (May 2012), pp. 9–24. ISSN: 0034-4257. DOI: 10.1016/j.rse.2011.05.028. URL: https://www.sciencedirect.com/science/article/pii/S0034425712000600 (Accessed 08/22/2023).

[114] V. Tsyganskaya, S. Martinis, and P. Marzahn. "Flood monitoring in vegetated areas using multitemporal Sentinel-1 data: Impact of time series features". In: *Water (Switzerland)* 11.9 (2019). DOI: 10.3390/w11091938.

[115] M. Tupas, C. Navacchi, F. Roth, B. Bauer-Marschallinger, F. Reuß, and W. Wagner. "COMPUTING GLOBAL HARMONIC PARAMETERS FOR FLOOD MAPPING USING TU WIEN'S SAR DATACUBE SOFTWARE STACK". English. In: *The International Archives of the Photogrammetry, Remote Sensing and Spatial Information Sciences*. Vol. XLVIII-4-W1-2022. ISSN: 1682-1750. Copernicus GmbH, Aug. 2022, pp. 495–502. DOI: 10.5194/isprs-archives-XLVIII-4-W1-2022-495-2022. URL: https://www.int-arch-photogramm-remote-sens-spatial-inf-sci.net/XLVIII-4-W1-2022/495/2022/ (Accessed 08/23/2022).

[116] M. Tupas, F. Roth, B. Bauer-Marschallinger, and W. Wagner. "Assessment of Time-Series-Derived No-Flood References for SAR-based Bayesian Flood Mapping". In: *GIScience & Remote Sensing* (2024). DOI: 10.1080/15481603.2024.2427304.

[117] M. E. Tupas, F. Roth, B. Bauer-Marschallinger, and W. Wagner. "An Intercomparison of Sentinel-1 Based Change Detection Algorithms for Flood Mapping". en. In: *Remote Sensing* 15.5 (Jan. 2023). Number: 5 Publisher: Multidisciplinary Digital Publishing Institute, p. 1200. ISSN: 2072-4292. DOI: 10.3390/rs15051200. URL: https://www.mdpi.com/2072-4292/15/5/1200 (Accessed 02/22/2023).

[118] M. E. Tupas, F. Roth, B. Bauer-Marschallinger, and W. Wagner. "Assessing Global Hand Datasets as Priors for SAR-Based Bayesian Flood Mapping". In: *IGARSS 2024 - 2024 IEEE International Geoscience and Remote Sensing Symposium*. ISSN: 2153-7003. July 2024, pp. 1209–1213. DOI: 10.1109/IGARSS53475.2024.10641043. URL: https://ieeexplore.ieee.org/abstract/document/10641043 (Accessed 11/04/2024).

[119] M. E. Tupas, F. Roth, B. Bauer-Marschallinger, and W. Wagner. "Improving Sentinel-1 Flood Maps Using a Topographic Index as Prior in Bayesian Inference". en. In: *Water* 15.23 (Jan. 2023). Number: 23 Publisher: Multidisciplinary Digital Publishing Institute, p. 4034. ISSN: 2073-4441. DOI: 10.3390/w15234034. URL: https://www.mdpi.com/2073-4441/15/23/4034 (Accessed 11/22/2023).

[120] A. Twele, W. Cao, S. Plank, and S. Martinis. "Sentinel-1-based flood mapping: a fully automated processing chain". In: *International Journal of Remote Sensing* 37.13 (July 2016). Publisher: Taylor & Francis, pp. 2990–3004. ISSN: 0143-1161. DOI: 10.1080/01431161.2016.1192304. URL: https://doi.org/10.1080/01431161.2016.1192304 (Accessed 11/19/2021).

[121] K. Uddin, M. A. Matin, and F. J. Meyer. "Operational Flood Mapping Using Multi-Temporal Sentinel-1 SAR Images: A Case Study from Bangladesh". en. In: *Remote Sensing* 11.13 (Jan. 2019). Number: 13 Publisher: Multidisciplinary Digital Publishing Institute, p. 1581. DOI: 10.3390/rs11131581. URL: https://www.mdpi.com/2072-4292/11/13/1581 (Accessed 03/20/2020).

[122] F. T. Ulaby, G. A. Bradley, and M. C. Dobson. "Microwave Backscatter Dependence on Surface Roughness, Soil Moisture, and Soil Texture: Part II-Vegetation-Covered Soil". In: *IEEE Transactions on Geoscience Electronics* 17.2 (Apr. 1979). Conference Name: IEEE Transactions on Geoscience Electronics, pp. 33–40. ISSN: 0018-9413. DOI: 10.1109/TGE.1979.294626. URL: https://ieeexplore.ieee.org/document/4071968 (Accessed 04/18/2024).

[123] N. Ulloa, S.-H. Chiang, and S.-H. Yun. "Flood proxy mapping with normalized difference Sigma-Naught Index and Shannon's entropy". In: *Remote Sensing* 12.9 (2020). DOI: 10.3390/RS12091384.

[124] M. Vreugdenhil, W. Wagner, B. Bauer-Marschallinger, I. Pfeil, I. Teubner, C. Rüdiger, and P. Strauss. "Sensitivity of Sentinel-1 Backscatter to Vegetation Dynamics: An Austrian Case Study". en. In: *Remote Sensing* 10.9 (Sept. 2018). Number: 9 Publisher: Multidisciplinary Digital Publishing Institute, p. 1396. ISSN: 2072-4292. DOI: 10.3390/rs10091396. URL: https://www.mdpi.com/2072-4292/10/9/1396 (Accessed 10/05/2023).

[125] W. Wagner, B. Bauer-Marschallinger, C. Navacchi, F. Reuß, S. Cao, C. Reimer, M. Schramm, and C. Briese. "A Sentinel-1 Backscatter Datacube for Global Land Monitoring Applications". In: *Remote Sensing* 13 (Nov. 2021), p. 4622. DOI: 10.3390/rs13224622.

[126] W. Wagner, G. Lemoine, and H. Rott. "A Method for Estimating Soil Moisture from ERS Scatterometer and Soil Data". In: *Remote Sensing of Environment* 70.2 (Nov. 1999), pp. 191–207. ISSN: 0034-4257. DOI: 10.1016/S0034-4257(99)00036-X. URL: https://www.sciencedirect.com/science/article/pii/S003442579900036X (Accessed 11/08/2023).

[127] W. Wagner, R. Lindorfer, S. Hahn, H. Kim, M. Vreugdenhil, A. Gruber, M. Fischer, and M. Trnka. "Global Scale Mapping of Subsurface Scattering Signals Impacting ASCAT Soil Moisture Retrievals". In: *IEEE Transactions on Geoscience and Remote Sensing* 62 (2024). Conference Name: IEEE Transactions on Geoscience and Remote Sensing, pp. 1–20. ISSN: 1558-0644. DOI: 10.1109/TGRS.2024.3429550. URL: https://ieeexplore.ieee.org/document/10601171?source= (Accessed 10/22/2024).

[128] A. Wania, I. Joubert-Boitat, F. Dottori, M. Kalas, and P. Salamon. "Increasing Timeliness of Satellite-Based Flood Mapping Using Early Warning Systems in the Copernicus Emergency Management Service". en. In: *Remote Sensing* 13.11 (Jan. 2021). Number: 11 Publisher: Multidisciplinary Digital Publishing Institute, p. 2114. ISSN: 2072-4292. DOI: 10.3390/rs13112114. URL: https://www.mdpi.com/2072-4292/13/11/2114 (Accessed 03/27/2023).

[129] R. S. Westerhoff, M. P. H. Kleuskens, H. C. Winsemius, H. J. Huizinga, G. R. Brakenridge, and C. Bishop. "Automated global water mapping based on wide-swath orbital synthetic-aperture radar". English. In: *Hydrology and Earth System Sciences* 17.2 (Feb. 2013). Publisher: Copernicus GmbH, pp. 651–663. ISSN: 1027-5606. DOI: https://doi.org/10.5194/hess-17-651-2013. URL: https://hess.copernicus.org/articles/17/651/2013/ (Accessed 11/17/2020).

[130] M. Wieland and S. Martinis. "A Modular Processing Chain for Automated Flood Monitoring from Multi-Spectral Satellite Data". en. In: *Remote Sensing* 11.19 (Jan. 2019). Number: 19 Publisher: Multidisciplinary Digital Publishing Institute, p. 2330. ISSN: 2072-4292. DOI: 10.3390/rs11192330. URL: https://www.mdpi.com/2072-4292/11/19/2330 (Accessed 08/15/2023).

[131] F. Wilcoxon. "Individual Comparisons by Ranking Methods". In: *Biometrics Bulletin* 1.6 (1945). Publisher: [International Biometric Society, Wiley], pp. 80–83. ISSN: 0099-4987. DOI: 10.2307/3001968. URL: https://www.jstor.org/stable/3001968 (Accessed 06/30/2024).

[132] X. Wu, Z. Zhang, S. Xiong, W. Zhang, J. Tang, Z. Li, B. An, and R. Li. "A Near-Real-Time Flood Detection Method Based on Deep Learning and SAR Images". en. In: *Remote Sensing* 15.8 (Jan. 2023). Number: 8 Publisher: Multidisciplinary Digital Publishing Institute, p. 2046. ISSN: 2072-4292. DOI: 10.3390/rs15082046. URL: https://www.mdpi.com/2072-4292/15/8/2046 (Accessed 09/13/2024).

[133] H. Xu. "Modification of normalised difference water index (NDWI) to enhance open water features in remotely sensed imagery". en. In: *International Journal of Remote Sensing* (Feb. 2007). Publisher: Taylor & Francis. DOI: 10.1080/01431160600589179. URL: https://www.tandfonline.com/doi/abs/10.1080/01431160600589179 (Accessed 03/07/2022).

[134] D. Yamazaki, D. Ikeshima, J. Sosa, P. D. Bates, G. H. Allen, and T. M. Pavelsky. "MERIT Hydro: A High-Resolution Global Hydrography Map Based on Latest Topography Dataset". en. In: *Water Resources Research* 55.6 (2019). _eprint: https://onlinelibrary.wiley.com/doi/pdf/10.1029/2019WR024873, pp. 5053–5073. ISSN: 1944-7973. DOI: 10.1029/2019WR024873. URL: https://onlinelibrary.wiley.com/doi/abs/10.1029/2019WR024873 (Accessed 08/02/2023).

[135] D. Zanaga, R. Van De Kerchove, W. De Keersmaecker, N. Souverijns, C. Brockmann, R. Quast, J. Wevers, A. Grosu, A. Paccini, S. Vergnaud, O. Cartus, M. Santoro, S. Fritz, I. Georgieva, M. Lesiv, S. Carter, M. Herold, L. Li, N.-E. Tsendbazar, F. Ramoino, and O. Arino. *ESA WorldCover 10 m 2020 v100*. Oct. 2021. DOI: 10.5281/zenodo.5571936. URL: https://zenodo.org/records/5571936 (Accessed 03/14/2024).

[136] M. Zhang, F. Chen, D. Liang, B. Tian, and A. Yang. "Use of sentinel-1 grd sar images to delineate flood extent in Pakistan". In: *Sustainability (Switzerland)* 12.14 (2020), pp. 1–19. DOI: 10.3390/su12145784.

[137] J. Zhao, M. Chini, R. Pelich, P. Matgen, R. Hostache, S. Cao, and W. Wagner. "DERIVING EXCLUSION MAPS FROM C-BAND SAR TIME-SERIES: AN ADDITIONAL INFORMATION LAYER FOR SAR-BASED FLOOD EXTENT MAPPING". English. In: *ISPRS Annals of Photogrammetry, Remote Sensing and Spatial Information Sciences*. Vol. V-1-2020. ISSN: 2194-9042. Copernicus GmbH, Aug. 2020, pp. 395–400. DOI: https://doi.org/10.5194/isprs-annals-V-1-2020-395-2020. URL: https://www.isprs-ann-photogramm-remote-sens-spatial-inf-sci.net/V-1-2020/395/2020/ (Accessed 08/29/2020).

[138] J. Zhao, Y. Li, P. Matgen, R. Pelich, R. Hostache, W. Wagner, and M. Chini. "Urban-Aware U-Net for Large-Scale Urban Flood Mapping Using Multitemporal Sentinel-1 Intensity and Interferometric Coherence". English. In: *IEEE Transactions on Geoscience and Remote Sensing* 60 (2022). ISSN: 0196-2892. DOI: 10.1109/TGRS.2022.3199036.

[139] J. Zhao, M. Chini, P. Matgen, R. Hostache, R. Pelich, and W. Wagner. "An Automatic SAR-Based Change Detection Method for Generating Large-Scale Flood Data Records: The UK as a Test Case". In: *IGARSS 2019 - 2019 IEEE International Geoscience and Remote Sensing Symposium*. ISSN: 2153-7003. July 2019, pp. 6138–6141. DOI: 10.1109/IGARSS.2019.8900534. URL: https://ieeexplore.ieee.org/document/8900534 (Accessed 11/12/2024).

[140] J. Zhao, R. Pelich, R. Hostache, P. Matgen, S. Cao, W. Wagner, and M. Chini. "Deriving exclusion maps from C-band SAR time-series in support of floodwater mapping". In: *Remote Sensing of Environment* 265 (Nov. 2021), p. 112668. ISSN: 0034-4257. DOI: 10.1016/j.rse.2021.112668. URL: https://www.sciencedirect.com/science/article/pii/S0034425721003886 (Accessed 11/12/2024).

[141] J. Zhao, R. Pelich, R. Hostache, P. Matgen, W. Wagner, and M. Chini. "A large-scale 2005–2012 flood map record derived from ENVISAT-ASAR data: United Kingdom as a test case". en. In: *Remote Sensing of Environment* 256 (Apr. 2021), p. 112338. ISSN: 0034-4257. DOI: 10.1016/j.rse.2021.112338. URL: https://www.sciencedirect.com/science/article/pii/S0034425721000560 (Accessed 03/16/2021).